Correlation of Thermal images and power degradation of Photovoltaic modules

Monphias Vumbugwa

Submitted in partial fulfilment of
the requirements for the degree of

Magister Scientiae

in the Faculty of Science
at the Nelson Mandela University

December 2018

Supervisor: Prof E.E. van Dyk
Co-Supervisor: Dr J.L. Crozier
Co-Supervisor: Dr F.J. Vorster

Declaration

Full Names: Monphias Vumbugwa

Student Number: 218207115

Qualification: Magister Scientiae

Title of Project: Correlation of Photovoltaics Plant Performance Metrics.

In accordance with Rule G4.6.3, I hereby declare that the above-mentioned treatise/ dissertation/ thesis is my own work and that it has not previously been submitted for assessment to another University or for another qualification.

Monphias Vumbugwa

Dated: November 2018

Dedicated to Laina, Laphine and Lowell

Acknowledgements

My sincere gratitude to:

- My supervisor, *Prof E.E. van Dyk* for his excellent guidance, support and encouragement throughout my research.
- My co-supervisor, *Dr J.L. Crozier* for her valued advice and assistance.
- My co-supervisor, *Dr F.J. Vorster* for his valued advice and assistance.
- *Mr I. Kwembur*, *Mr R.M. Dix-Peek* and *Dr R. Schultz* for their useful assistance in this work.
- *Mr Johan Wessels* for his technical assistance.
- My colleagues and friends in the Physics department and PV research group for their help and contributions during this project.
- *Ms Jualine Ferreira*, *Miss Mariska Muller* and *Ms C. Neveling* for their administrative help.
- The *National Research Foundation (NRF)*, *Nelson Mandela University (NMU)* and *Photovoltaics Insight (PVi)* for the financial support.
- A special thanks to my wife *Megnolia* for her support and encouragement during the course of my studies.
- And last but not least to the *Almighty God*, for taking me through this.

Abstract

The generation of electrical energy using Photovoltaic (PV) technology has increased globally with the decrease in the cost of PV systems and the rise in electrical power demand. In South Africa, the support by the government in implementing the Renewable Energy Independent Power Producer Procurement Programme (REIPPPP) has seen a growth in PV system deployment and investment in roof and ground mounted, stand alone and grid connected PV plants. This rapid growth shows that the PV industry is becoming highly competitive as there is a shift to low carbon emissions and it is anticipated to be the most affordable source of electricity. Hence, there is need to develop maintenance and fault diagnosis expertise and capabilities in the PV industry, which can in turn improve the dependability, productiveness and lifespan of PV systems. Solar PV modules directly receive and convert solar irradiance into electricity and may not generate the expected optimum energy due to abnormalities which arise when they are exposed to harsh unfavorable environmental conditions in the field.

Thermal Infrared (TIR) imaging is widely used as a fault diagnosis tool in operating PV modules and mostly in large PV power plants. Therefore, there is need to research the interpretation of the observed thermal signatures and the impact that the anomalies have on electrical output of the system so as to improve the PV maintenance systems. This research focuses on identifying performance limiting defects using an Infra-Red (I-R) camera, mounted on an Unmanned Aerial Vehicle (UAV), to understand the effect of thermal signatures on current-voltage (I-V) characteristics of PV module strings.

Aerial TIR imaging using a UAV can rapidly identify abnormalities in operational PV modules strings as hotspots. Any deviation of the string I-V curve, from the expected, indicates a problem with one or more PV modules in the string. However, locating the faulty module involves measuring I-V parameters of the individual modules in a string, which is not feasible in large PV power plants. Therefore, there is a need to estimate the power loss associated with the thermal signatures in PV module strings. Visual inspection may help in identifying the exact cause of some hotspots, while other hotspots need special characterization techniques, such as Electroluminescence (EL) and UV Fluorescence (UV-F), which can indicate if a solar cell is cracked or has weak busbars or contact finger connections.

Shattered module glass results in notable string power deterioration and if left unattended, poses a safety issue due to the presence of shattered glass and the continued hot-spotting presents fire risks. The intrusion of moisture through the cracked area causes other secondary defects like delamination and corrosion of cell parts especially if the plant is in an industrial location. Uneven shading due to soiling can be identified in thermal imaging and can alter the shape of current-voltage (I-V) curve, affect the operating point and results in significant power loss in multi-crystalline silicon (mc-Si) strings depending on area affected. However, the use of bypass diodes minimize PV module string power loss. The absence of bypass diodes in thin-film copper-indium-gallium-diselenide (CIGS) modules can result in detrimental effects and possible permanent damage of the partially shaded module. This correlation of thermal anomalies with PV module string performance may add value towards the development of operation and maintenance of solar PV systems and improvement of the PV industry.

Keywords: UAV, TIR thermography, hotspot, I-V characteristics, string, performance

Table of Contents

List of Tables

List of Figures

Chapter 1

Introduction

1.1 Photovoltaics status

The traditional fossil fuel energy generators, which are currently the major sources of energy, cannot meet the world's high demand of energy and apart from being associated with energy conversion losses they have negatively impacted on the environment through emitting greenhouse gases and other waste products. The waste products emitted from the fossil fuel industry were nearly constant, in 2016, due to the advancement in the use of alternative renewable sources of energy, such as solar photovoltaics (PV) and wind power, to address the global energy needs [1][2].

Solar energy is the largest renewable energy source and solar PV is the world's fastest expanding energy technology. It is now amongst the most viable and sustainable electrical power generators, and is destined to be a cheap and widely used global electrical energy source [3], due to the international drive aiming for clean power production [4]. Through research in PV technologies, which not only focus on system efficiency but also on its reliability, the global PV industry has developed rapidly resulting in increase in PV systems (stand alone and grid tied) installations of up to 303 GW worldwide as shown in Figure 1-1 [2][5].

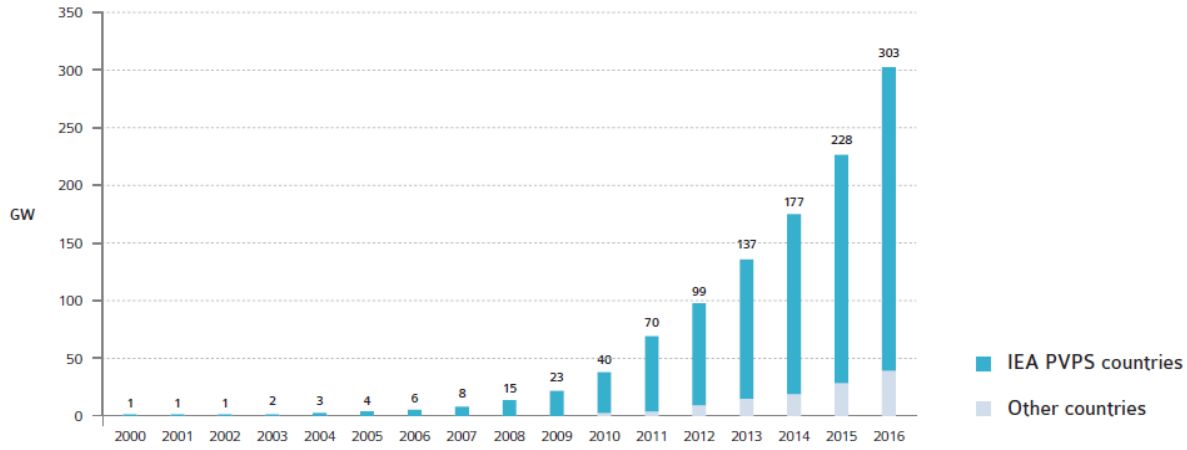

Figure 1-1: Cumulative Global solar PV installed capacity by the end of 2016 [6].

Countries of IEA PVPS: Australia, Austria, Belgium, Canada, Chile, China, Denmark, Finland, France, Germany, Israel, Italy, Japan, Korea, Malaysia, Mexico, Netherlands, Norway, Portugal, South Africa, Spain, Sweden, Switzerland, Thailand, Turkey, USA.

The fast growth of PV systems deployment is due to the rising demand for electricity, the need for clean power production, improved policy support for renewable energy and mostly due to cost reduction in PV modules [2][5], as indicated by the trend of graphs of three selected countries, which report to International Energy Agency (IEA), in Figure 1-2.

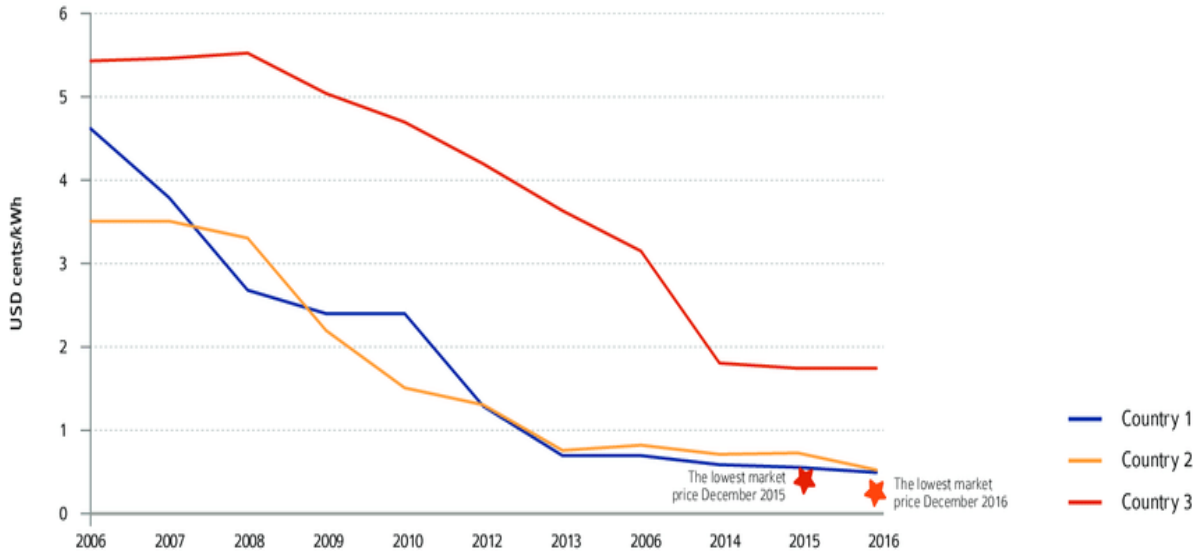

Figure 1-2: Trend of PV module prices in selected 3 IEA countries from 2006 to 2016 [6].

Solar energy is abundant in Southern African nations, where the average solar irradiance of more than 6.0 kWh/m^2 on a sunny day is experienced, as seen in Figure 1-3. The African continent is increasingly turning to solar PV as an economic means to strengthen energy security [6]. In 2012, it was noted that there was high potential in PV technology development in three African countries namely South Africa, Zimbabwe and Kenya [7], and South Africa took the lead having a total of installed capacity, mostly large-scale ground mounted, reached more than 1 GW by end of 2016. The sustainable development in growth of PV energy capacity, in South Africa, was mainly due to the implementation of the Renewable Energy Independent Power Producer Procurement Programme (REIPPPP) [8]. The programme has resulted in 8.1 GW allocated to renewables (mainly wind and PV) and by end of 2016, 1.5 GW of this (8.1 GW) was feeding electrical power into the grid from PV systems and no significant change was observed in grid-connected plants in 2017. Furthermore, it caused a sharp rise of 3.8% in energy from renewable power sources since 2010, which led the country to be in the top ten for installed, utility scale solar PV capacity in the World. South African municipalities are anticipated to have a huge role in unlocking investment opportunities for PV energy services by allowing small scale embedded generation, which comes with rules and safety

issues on high quality solar PV use and installations under the GreenCard [9][10]. Technology improvements and lower costs of PV system installations have motivated local entrepreneurs in the solar home system (SHS) market and in developing stand-alone mini-grids [5].

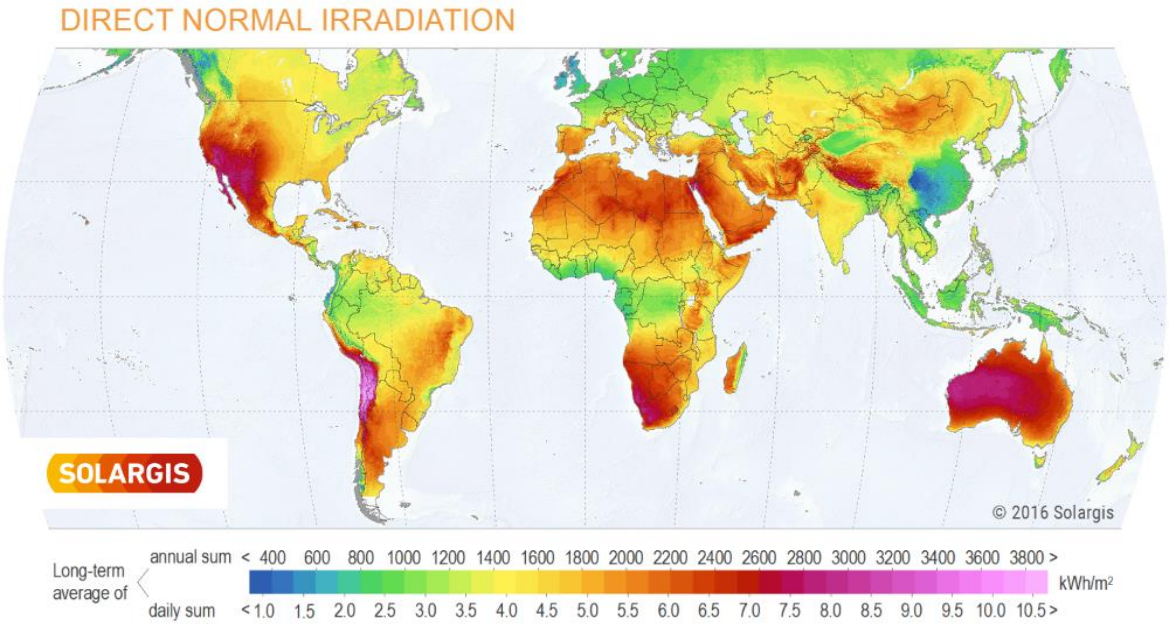

Figure 1-3: Global horizontal solar irradiation map [11].

Solar PV plays a substantial role in electricity generation in several countries, and the establishment of very large PV parks, in South Africa, will increase the shift from relying on traditional power generators and will see the country tackling the chronic power challenges [10]. In Zimbabwe, the growth in PV as an alternative to the grid, in providing basic electricity services (light, radio, TV) to rural communities was due to international donor funded PV activities and the duty free imports of low cost silicon PV modules from neighboring countries, South Africa and Botswana [7], despite the fact that, at one point (1988) it had the capability (Solarcomm) to assemble solar modules from imported PV cells. The do-it-yourself (DIY) approach, which dates back from 1990 [12], is still carried on in installing small household PV generators to bridge the gap of energy need, although there are huge projects under Zimbabwe Power Company (ZPC) awaiting implementation, such as the Gwanda, Munyati and Insukamini solar PV plants [13]. Also, a UK company (Rhino Green Energy) is working on installing a 50 MW plant in Marondera [14]. The attracting of investors into its energy infrastructure, the call for tenders to grant power purchase agreements (PPA) and since PV offers access to cheap electricity [5], it is expected that the nation will not only accelerate the

nation's economic development but also decrease reliance on energy imports and simultaneously reducing environmental degradation.

1.2 Research Objectives

Solar PV modules are key components of a PV system and are meant to last for more than 20 years while in operation with minimal maintenance. Nevertheless, there are several PV module failure modes and degradation mechanisms which can reduce efficiency or cause the modules to fail when they are deployed outdoors, where they are exposed to long-term real field operational conditions [15][16], and during the post-manufacturing period when transporting and installing the PV modules [17]. For this reason and since there is a notable shift towards solar energy (as discussed earlier), the operation and maintenance of PV systems becomes a very crucial and valuable activity to meet energy efficiency and for PV modules to operate for the expected period. The focus of this study is on correlating the performance limiting anomalies, identified by aerial TIR imaging of a PV plant, in-situ, with the PV module string output current-voltage characteristics so as to understand the impact of thermal signatures on PV module string efficiency and acquire valuable knowledge aiming to improve the effectiveness of quality assessment tools in PV plants.

PV plants normally use Supervisory Control and Data Acquisition (SCADA) systems to monitor power generated and status of various sections of the plant. The system saves maintenance time and costs as it can remotely present performance data as graphs and distinguish any underperforming unit of the plant from good operating units [18]. However, it requires physical checking and testing of the equipment, in the underperforming sector, to rectify the fault causing the affected unit to generate low power than expected. This can involve traditional power testing of PV modules using a current-voltage (I-V) curve tracer. An I-V tracer is used to reveal the performance of a PV module string and if it shows abnormal I-V characteristics then the string is faulty. The fault can be detected by further testing and carrying out visual inspection on individual modules in the string. This conventional testing technique, is costly, time consuming [17], and impractical especially when dealing with large-scale PV plants consisting of hundreds or thousands of PV modules. Thermal Infra-Red (TIR) imaging can quickly identify abnormalities in operating PV modules as areas of elevated temperature. Aerial TIR inspection is cost effective and can locate defective parts of a PV module which cannot be visually observed [19][20].

The increase in PV technologies, and large on-and-off grid PV generators call for the need for efficient and reliable PV plant maintenance system and tools so as to obtain optimum yield for the long-expected lifetime of PV modules. Therefore, detailed understanding of the detrimental effect of thermal signatures on PV module performance is important to develop the operation and maintenance of PV plants and for efficient use of a clean and unlimited renewable resource, solar.

The approach suggested the use of aerial Infrared Thermography analysis for monitoring the operating temperature of PV modules to detect possible malfunctions in the form of hot spots and estimate inefficiency of the PV module strings in relation to the observed thermal signatures. A TIR camera mounted on an Unmanned Aerial Vehicle (UAV) which is remotely controlled was used to highlight anomalies on PV modules in operation. Visual inspection of the modules under study was carried out, referencing to thermal images, to determine the actual anomaly causing the hotspot. Then, I-V parameters of the affected module strings, and singular modules, were measured and corrected to Standard Testing Conditions (STC) for detailed analysis and estimation of power loss linked to the thermal abnormalities.

1.3 Dissertation outline

This section summarises the contents of the chapters that follow.

Chapter 2: The chapter introduces the physics of semiconductors and gives a brief description of a p-n diode and the properties of solar cells. The I-V characteristics of solar cells and modules under different conditions and Thermography are discussed in detail.

Chapter 3: This section presents the experimental layout showing how the results were obtained. The setups, equipment used, and the steps followed in the TIR imaging and I-V parameter measuring on ground mounted PV modules are discussed here.

Chapter 4: Detailed analysis and discussion of the observed results is presented in this section. The results show the correlation of the thermal signatures with the I-V characteristics of the PV module strings and discusses possible causes of the module strings power deterioration.

Chapter 5: The chapter summarises and concludes the research work and proposes some future work to be investigated.

Chapter 2

Theory

2.1 Principles of solar cells

2.1.1 Introduction

A phenomenon allowing solar radiant energy to be directly converted to electricity (the photovoltaic effect), was discovered in 1839 by the French physicist, Edmond Becquerel, while carrying out electro-chemical experiments [21], and comprehensive description of the theory of solar cell operation was given in 1905 by Einstein, and Schottky in 1930. Chapin, Pearson and Fuller, in 1954, developed a silicon solar cell which could convert 6% of sunlight into electricity, and since then solar cells with higher efficiency were commercially available, with the best, silicon solar cell, now reaching around 25% efficiency [22].

2.1.2 Semiconductor Properties

Group IV, on the periodic table, consists of semiconductor elements such as silicon (Si) and germanium (Ge) with four electrons in their valence shells which can gain energy and get excited to the conduction band as shown in Figure 2-1. When an electron is moved from the valence band to the conduction band it constitutes the creation of an electron-hole pair, thus increasing the mobility of charge carriers and electrical properties of the material. Silicon has a forbidden energy gap of ΔE_G = 1.12 eV [1].

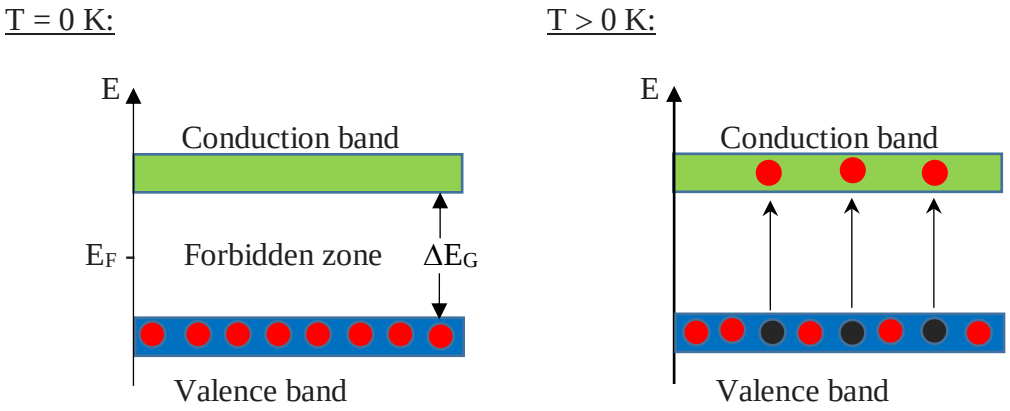

Figure 2-1: Thermally excited valence electrons overcome the band gap to the conduction band (adapted from [1]).

The highest energy state occupied by electrons, Fermi level (E_F), for the intrinsic semiconductor lies in the middle of the forbidden band at 0 K, as shown in Figure 2-1, and it indicates equal concentrations of free electrons and holes.

Solar cells are produced from semiconductor materials by doping usually with boron, to obtain positive charge carriers called holes, making the semiconductor layer p (positive)-type, and by doping with phosphorus so as to have negative charge carriers, electrons, making the semiconductor layer n (negative)-type. Doping of intrinsic semiconductors materials, usually silicon, with impurities to have extrinsic semiconductors, improves the electrical properties of semiconductors by changing the electron and hole carrier concentrations [21]. The imbalance of electrons and holes also affects the Fermi level by causing it to rise towards the conduction band, in n-doped material, and to drop towards the valence band, in p-doped semiconductor, as indicated in Figure 2-2.

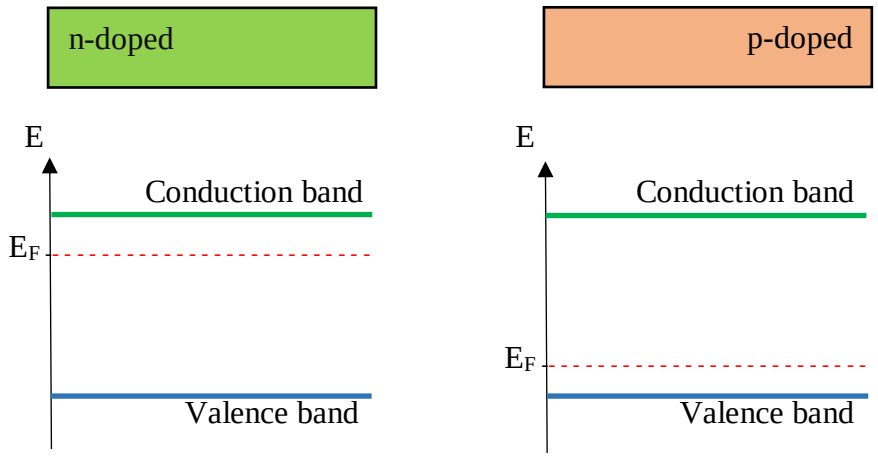

Figure 2-2: Fermi level effect on isolated p and n materials.

2.1.3 The p-n junction

Joining the p-type and n-type semiconductors creates a p-n junction with an electric field set up, in the region of the junction, due to the diffusion of electrons as they try to evenly distribute themselves. Movement of charge carriers will cease as electrons find it hard to cross against the building electric field, creating the depletion layer between the p and n type materials. The depletion region can be manipulated by applying voltage or by exposing it to light, causing the charge carriers to drift.

When the p and n materials are brought together their Fermi levels align as shown in the energy band diagram in Figure 2-3, that is if the materials have same temperature, and a built in potential equal to ΔE and relating to the band gap is developed [1].

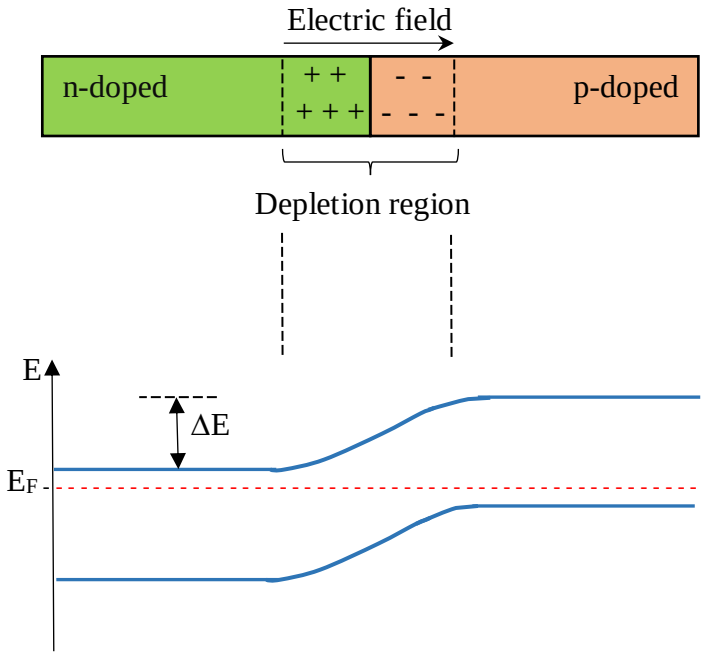

Figure 2-3: Fermi level for a thermally equilibrium p-n junction.

2.1.4 Current generation

When solar light is incident on solar cells it may be reflected, transmitted or absorbed and if absorbed, the photons transfer their energy to electrons. Photons with energy equal to or greater than the band gap of the semiconductor material will lead to generation of charge carriers and the excess energy will increase the lattice vibrations resulting in rise of temperature of the semiconductor. When connected across a load, current will flow from the cell to the external load, as shown in Figure 2-4.

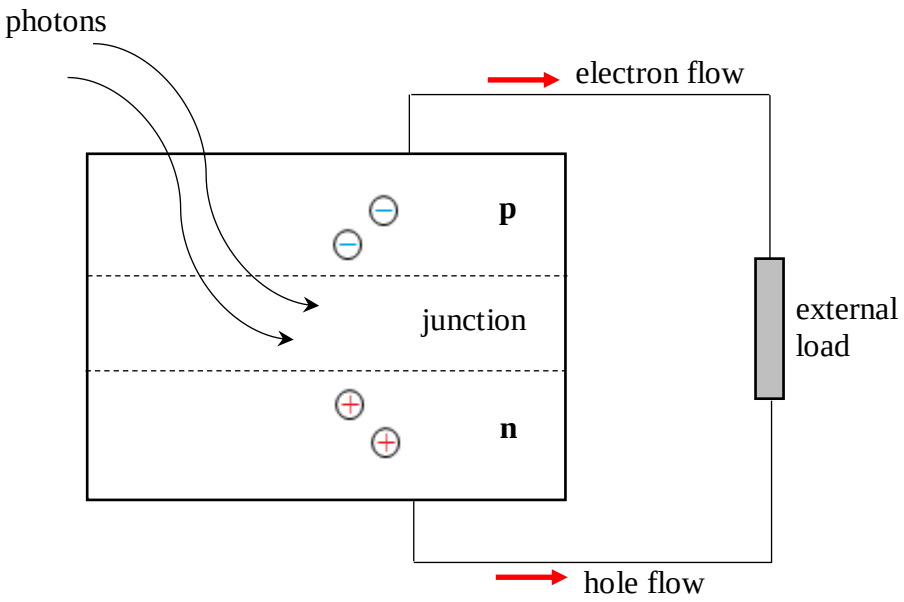

Figure 2-4: The photoelectric effect in a solar cell.

The photon energy is expressed as:

$$E = hf \qquad 2.1$$

where h is Plank's constant 6.63 x 10^{-34} Js and f is the frequency of the incident photon [23].

The p-n junction's electric field provides the voltage for the solar cell which is of the order of 0.6 V for a crystalline silicon PV cell [21].

The idealized equivalent circuit of a solar cell is shown in Figure 2-5, and the source current I, which results from excitation of electrons by solar radiation, flows to the external load of resistance R_L when the diode voltage is V.

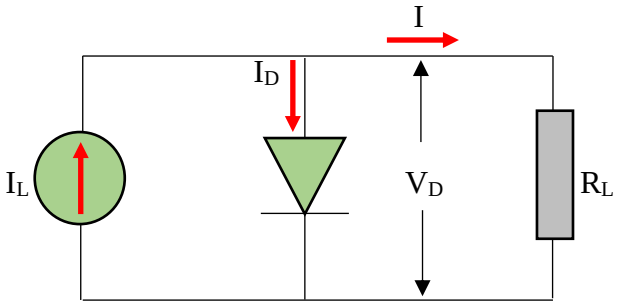

Figure 2-5: The equivalent circuit of a solar cell.

The current source represents the photon generation current, I_L, and the diode current I_D, the dark current of the solar cell which is given in equation 2.2 [23].

$$I_D = I_S\left(e^{\frac{qV}{nkT}} - 1\right) \qquad 2.2$$

where: I_S = the saturation current of the p-n junction

q = elementary charge

n = ideality factor of the diode

k = Boltzmann's constant

T = absolute temperature

According to Kirchhoff's current law, the sum of the currents at a junction is zero. Therefore, the current of a solar cell can be expressed as:

$$I = I_L - I_D \qquad 2.3$$

Combining equations 2.2 and 2.3 gives the current in the solar cell which can be expressed by equation 2.4.

$$I = I_L - I_S\left(e^{\frac{qV_D}{nkT}} - 1\right) \qquad 2.4$$

If solar cells are in use, there exist series (R_s) and shunt (R_{sh}) resistances. Figure 2-6 shows the structure of a typical solar cell indicating these parasitic resistances. The resistances cause a change in the equivalent circuit model of an ideal solar cell to the one shown in Figure 2-7, with series and shunt resistances taken into account.

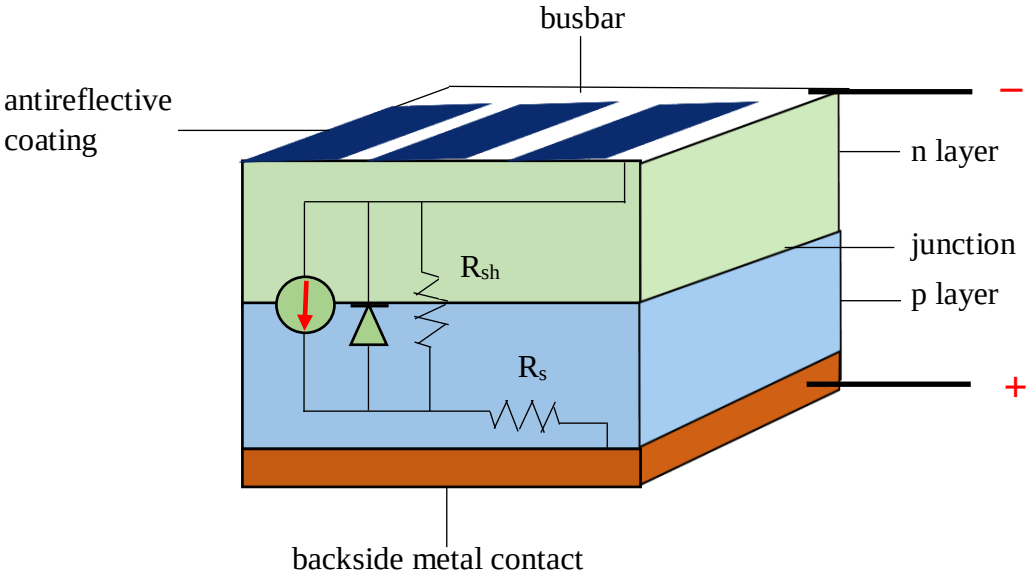

Figure 2-6: Typical solar cell structure.

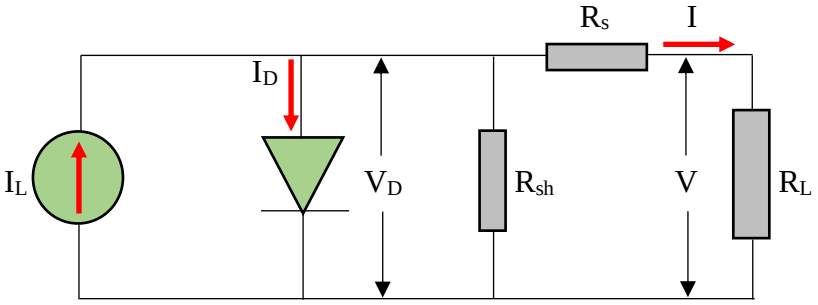

Figure 2-7: Parasitic series and shunt resistances in a solar cell equivalent circuit.

R_s is due to the resistance of the movement of current through the p-n material of the solar cells, the metal contacts and the busbars and it limits the current (I) generated under light conditions. The voltage (V) across the load is now given by equation 2.5 and equation 2.6 shows the one-diode model equation.

$$V = V_D - IR_S \qquad 2.5$$

$$I = I_L - I_S\left(e^{\frac{q(V+IR_S)}{nkT}} - 1\right) - \frac{(V+IR_S)}{R_{sh}} \qquad 2.6$$

2.1.5 Solar cell technology

PV cells can be classified as either wafer-based crystalline, compound semiconductor (thin-film) or organic. The wafer-based crystalline technology of which multi-crystalline silicon (mc-Si) modules fall into is the first-generation PV system. Thin-film technology is a second-generation PV system including copper-indium-gallium-diselenide (CIGS) and cadmium telluride (CdTe) modules. Currently crystalline silicon technologies account for more than 90% of the overall cell production [24].

Single-crystalline silicon (c-Si) PV cells are more efficient (16-25% efficiency) than mc-Si cells whose average conversion efficiency is around 14-18% but are more popular as they are less expensive to produce. Thin-film materials commercially used are CdTe and CIGS and the cells are formed by depositing extremely thin layers of these semiconductor materials onto a backing material such as glass, stainless steel or plastic and are potentially less expensive to manufacture than crystalline cells. Amorphous silicon cells are cheaper to produce than the wafer based crystalline cells and currently have efficiency of around 10% [1]. The disadvantages of thin-film technology are lower efficiency and uncertain durability, but they have a slightly better performance than crystalline cells under low light conditions and are also less likely to suffer power loss from partial shading of the operating cells [25]. Commonly used commercial silicon solar cells measure approximately 0.16 m x 0.17 m and deliver I_{sc} of 8 A when V_{oc} is 0.5 – 0.6 V [1].

2.2 PV module construction

A single PV cell generates low voltage and electrical power, which are insufficient for use in many devices. Hence, to increase their utility, several cells are electrically connected in series to form a module which outputs standard power depending with module type and size. The number of cells determine the voltage of the PV module while its current depends on the size of the solar cells and their efficiency.

The modules are installed outdoors, hence the need to protect the solar cells from harsh environmental influences so that they may operate in the field for more than 20 years while generating optimum expected power. Figure 2-8 shows the layers of materials used to build a PV module, and the materials used are mainly for protection of solar cells from mechanical damage and moisture infiltration. Moisture ingress will cause rapid degradation of the module due to corrosion of metal contacts and interconnects. The interconnected cells are first coated with a non-reflective layer of silicon nitride or titanium oxide, to reduce losses due to sunlight

reflection and then they are encapsulated between two layers of ethylene vinyl acetate (EVA). EVA is used because it is stable under ultra violet (UV) light, and at high temperatures. The laminated cells are sandwiched between the front glass and the backing material. Tedlar dissipates heat quickly (unlike glass) due to its low thermal resistance, so it is commonly used at the back surface to transfer heat from overheated cells. It also provides support for the solar cells. Using glass at the front surface allows transmission of the wavelengths of light, to the cells, needed for power generation and reduce a build-up of dust and dirt which could shade the cells since glass has smooth surfaces. Aluminium is usually used to frame the layers and provide additional structural support [26]. A junction box, which is fixed at the backside of the module, houses the connections of the cell substrings to the terminals of external cables and usually in some it contains bypass diodes [17]. Typically, Schottky diodes are used [27], and the purpose of using bypass diodes in PV modules is discussed in section 2.5.

Typical commercial thin-film modules, such as CIGS and CdTe, are fabricated using monolithic integration technique. This approach involves successive deposition of metal contacts and semiconductor layers on glass, spread with scribing steps to form hundreds of series connected cells [28]. Crystalline PV modules manufacturing process allows bypass diodes to be incorporated in the module [29], but the scribing based approach makes it difficult to include bypass diodes and rarely one bypass diode can be used to protect the cells [28]. The monolithically integration process provides important cost advantage for thin film technologies.

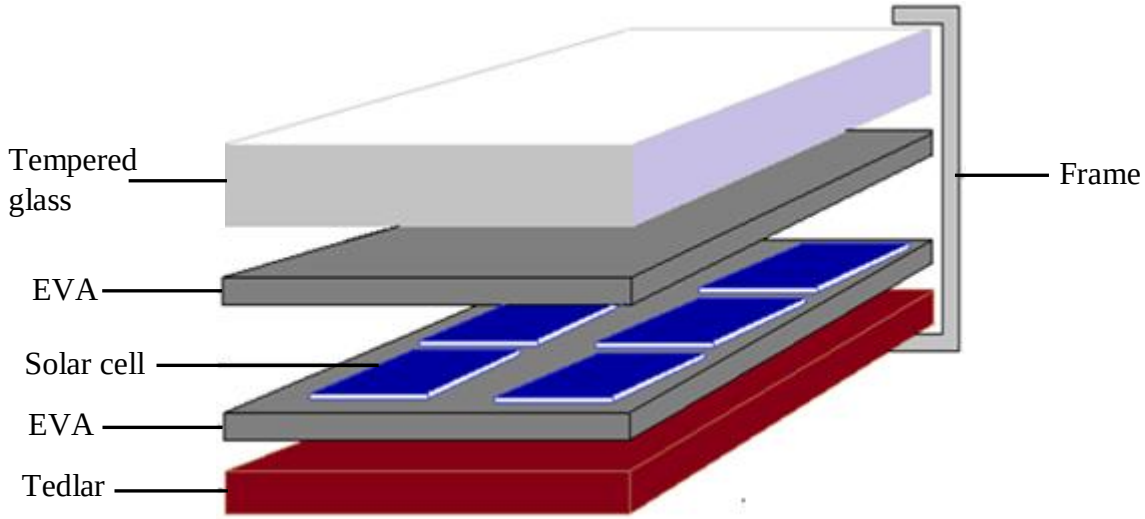

Figure 2-8: Typical structure of a silicon PV module (adapted from [26]).

2.3 Electrical characteristics of Solar cells and PV modules

2.3.1 Characteristics and performance parameters

The electrical behavior of a solar cell can be described by using the current equation 2.6 and an equivalent circuit in Figure 2-7. The performance parameters of a solar cell or module are obtained by outdoor measurement of their current-voltage (I-V) values using the I-V curve analyzer. The equipment is discussed in detail in section 3.2.2.

Figure 2-9 shows a typical I-V characteristic of a silicon solar cell together with performance parameters, open-circuit voltage (V_{oc}), short circuit current (I_{sc}), current and voltage at maximum power point, I_{mp} and V_{mp}, and the maximum power (P_{max}). Also shown in the figure is the power curve of the I-V characteristic. A simulator program, PVSim, [30], was used to show the efficiency of solar cells and modules under different conditions, as shown in some sections that follow. The values of the parameters for the simulated I-V characteristic in Figure 2-9 are listed in Table 2-1.

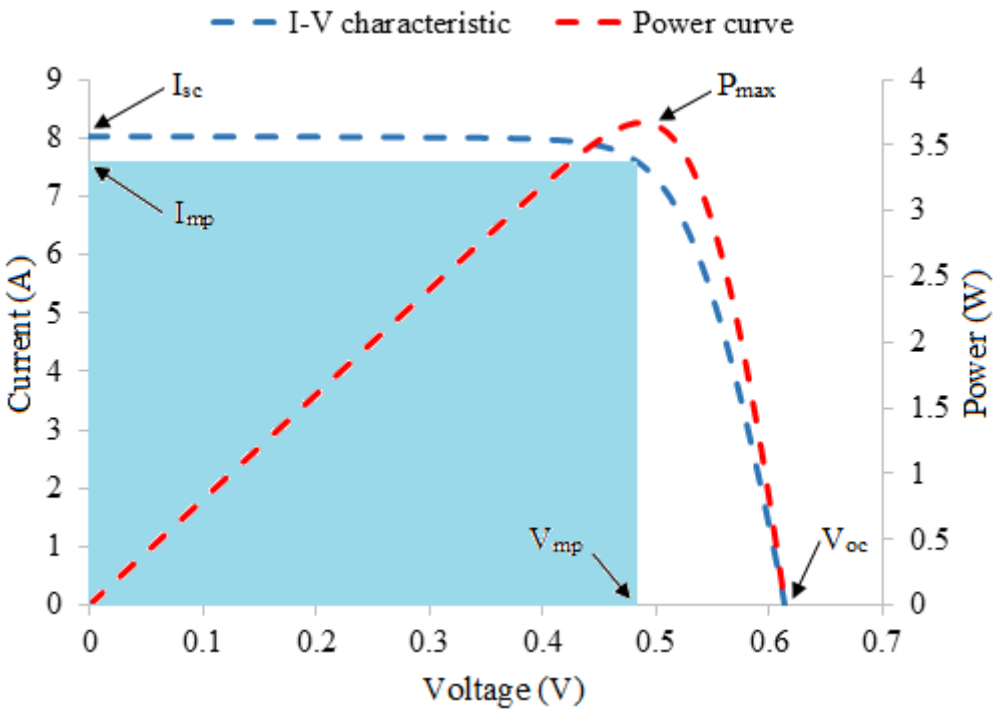

Figure 2-9: A simulated performance characteristic of a silicon solar cell under standard test conditions.

Table 2-1: Parameters of the simulated I-V characteristic of a silicon solar cell.

I_{sc}	8.0 A
V_{oc}	0.62 V
R_s	6.0 x 10^{-3} Ω
R_{sh}	34.70 Ω
N (non-ideal diode quality factor)	3.73

The power at any point along the I-V characteristic of Figure 2-9 is a product of current and voltage, and the maximum power (P_{max}) is located around the "knee" of the I-V curve.

Since P = VI, it implies that

$$P_{max} = I_{mp}V_{mp} \quad (2.7)$$

and corresponds to the shaded area under the I-V characteristic in Figure 2-9.

If the total incident power per meter square, termed irradiance (E) is known, then conversion efficiency of a PV cell or module is:

$$\text{Efficiency} = P_{max}/EA \quad (2.8)$$

where: A is the area of a cell or module in m^2.

Efficiency also depends on the characteristics of the solar cell material and the technology as described in section 2.1.5.

According to reference [31], fill factor (FF) is also a useful performance indicator in PV cells and modules. It is a ratio of the maximum power to the product of I_{sc} and V_{oc}, and typical FF values for silicon cells and thin film cells are between 0.75-0.85 and 0.6-0.75, respectively. Any impediment that causes a reduction in FF will result in power loss.

$$FF = P_{max}/V_{oc}I_{sc} \quad (2.9)$$

2.3.2 Influence of Irradiance and Temperature on I-V parameters

Solar irradiance is a measure of power density of sunlight received at an area, while irradiation is the measure of energy density of the sunlight. As the solar insolation keeps on changing throughout the day similarly the I-V and power-voltage (P-V) characteristics of the solar cell

or PV module varies. The photon generated current, I_L, is approximately equal to I_{sc} and linearly dependent on irradiance and is given by

$$I_L = XI_{L1-sun} \quad 2.10$$

where: X is the level of irradiance and $I_{L1\text{-}sun}$ represents photocurrent at irradiance of 1000 W/m^2 [32].

Shading reduce the irradiance falling onto the solar cells. Shading might be due to cloud cover or any object (buildings or plants) which can obstruct sunlight falling onto the solar cells. Soiling consisting of dust, dirt and bird droppings is also a form of shading which can decrease the output current of PV modules [33]. Uniform shading on all cells in a PV module, unlike uneven shading, results in equal reduction of solar energy incident onto the cells and in turn drops the output current. Uneven shading is described in section 2.5 of this document.

Optical degradation on PV modules as a result of discoloration, glass breakage, delamination and bubbles affect optical properties of the module resulting in unwanted optical reflection and limiting of the penetrating of solar energy incident on the operating solar cells. This consequently affect the generated power. Evolving optical degradation is usually detectable, with a simple optical/visual inspection by naked eye, before any significant loss of PV module's power output or safety risk issue occurs. Optical degradation, especially discoloration, can be related to significant thermal stress and the generation of acetic acid when the module is under real field conditions [17].

When loss in irradiance striking the solar cells occurs, a drop of output current values is evidenced on the I-V characteristic of the impacted PV module. This drop results in generated power output losses. The PV module characteristics under 900 W/m^2 and 500 W/m^2 is shown in Figure 2-10, and it clearly indicates a drop in I_{sc} and I_{mp} at lower irradiance which affects the P_{max} of the PV module.

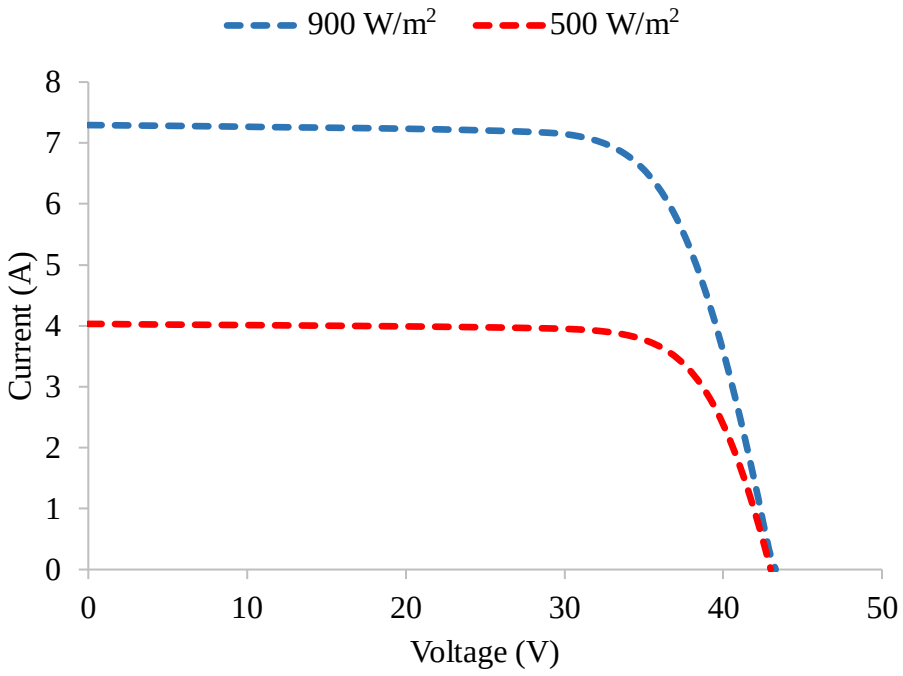

Figure 2-10: Effect of change in incident solar irradiance on I-V characteristics of a PV module, imitated at 25°C.

An increase in temperature results in a decrease in the band gap energy, of the semiconductor material, and increase in minority carrier lifetime. The increased temperature also increases the dark saturation current density, which affects the open circuit voltage (V_{oc}), and results in an increased light-generated current thus affecting the short circuit current (I_{sc}) [23].

The effect of temperature change on I-V characteristic is shown in the simulated I-V curves in Figure 2-11. When temperature increases, from 30°C to 65°C, V_{oc} is significantly reduced while I_{sc} increases slightly as seen in the I-V curves, and the module becomes less efficient, as indicated by the calculated power in Table 2-2. There is approximately 58.1 W power loss due to this change in temperature. The photon generated current, I_L, increases slightly due to an increase in the number of thermally generated carriers in solar cells [34].

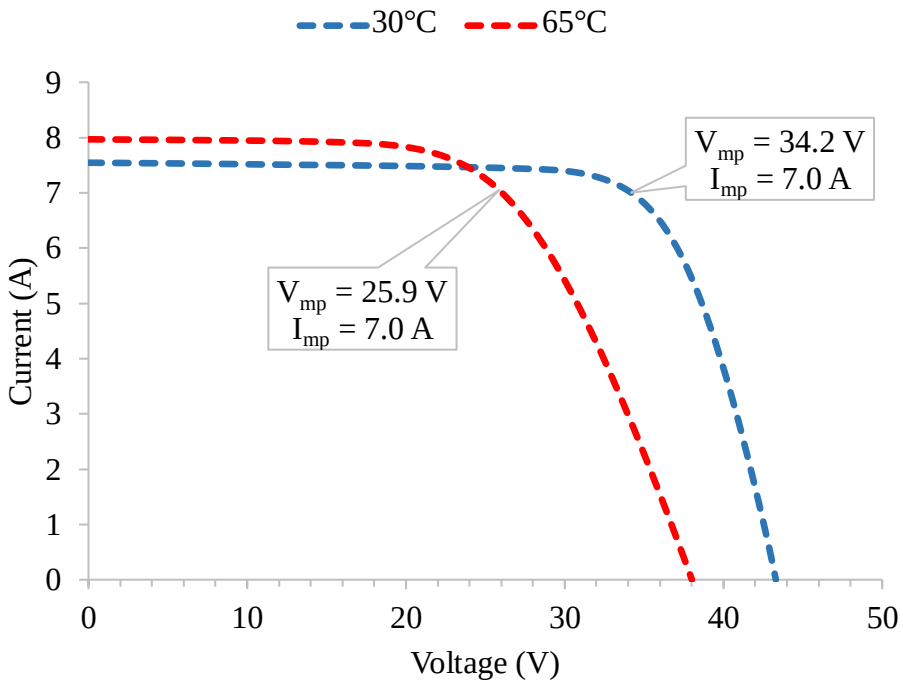

Figure 2-11: Modelled I-V curves of a module at same irradiance and different temperatures.

Table 2-2: Effect of temperature change on PV Module's output power.

Temperature (°C)	V_{mp} (V)	I_{mp} (A)	P_{max} (W)
30	34.2	7.0	239.4
65	25.9	7.0	181.3

The power of a solar module is measured according to the Standard-Test-Conditions (STC) and defined by three conditions:

1. Full solar irradiance, E = 1000 W/m^2
2. Cell temperature, T = 25°C
3. Air mass, AM, of 1.5.

However, in practical applications, PV modules rarely operate under such situations, so the I-V measurements taken in the field, which should be at an irradiance greater than 650 W/m^2, must be corrected to STC conditions [33][17]. Irradiance and temperature measured at the same time as the I-V curve data are used to correct to STC.

Equation 2.11, is used to correct the measured current, $I_{m,}$ to STC corrected current (I_c) [35], and depends highly on the solar irradiance (E). The calculation of corrected voltage (V_c), which is affected by the module temperature T, is given by equation 2.12 with V_m being the measured voltage. The current (α) and voltage (β) temperature coefficients vary with module technology

and are given by the manufacturer, or they can be determined by using regression analysis method on the I-V parameters measured at different temperatures [36].

$$I_c = [I_m + \alpha(25 - \mathrm{T})] \text{ x } \frac{1000}{\mathrm{E}} \qquad 2.11$$

$$V_c = [V_m + \beta(25 - \mathrm{T})] \qquad 2.12$$

Quantification of uncertainty is an obligation for measurements. It is advised, for all power measurements, to be quoted with their standard uncertainties so as to realise and understand the influence of factors such as uncertainties on measured values (current and voltage), non-uniformity of solar illumination on modules and sensor uncertainties in the temperature coefficients which are used in the translation equations [37].

2.3.3 Series and Shunt resistances in solar modules

Solar cells should have low R_s since the presence of high series resistance limits the output current, as discussed in section 1.1.4, and reduces the voltage at a particular current but has no impact on the open circuit voltage nor on the short circuit current of the module. At very high values of R_s, there will be a significant reduction in I_{sc} and the behavior of the solar cell resembles that of a resistor [38].

Low shunt resistance is caused by shunt paths which result in directing the light generated current through an alternate path. Such a diversion reduces the amount of current at a specific voltage which lowers current flowing to the load thus reducing output power. The presence of shunt resistance is mostly due to manufacturing defects. Low shunt resistance under reduced light levels degrades the efficiency of a PV module significantly [39], therefore for a cell or module to operate more efficiently, a high value of R_{sh} must be achieved.

The effects of R_s and R_{sh} on the modelled I-V curves of a PV module are shown in Figure 2-12 (a) and (b) for a three substring 72 cell module. In (a), there is a change in slope near V_{oc} with increase in R_s and with large values of R_s the module's I_{sc} drops. There is a reduction in V_{oc} and a change in slope, near I_{sc}, when R_{sh} is decreased from 34.1 Ω to 0.04 Ω. The I-V curves show the change in slope when a module has high R_s (near V_{oc}) and low R_{sh} (near I_{sc}) which have an impact of reducing the fill-factor.

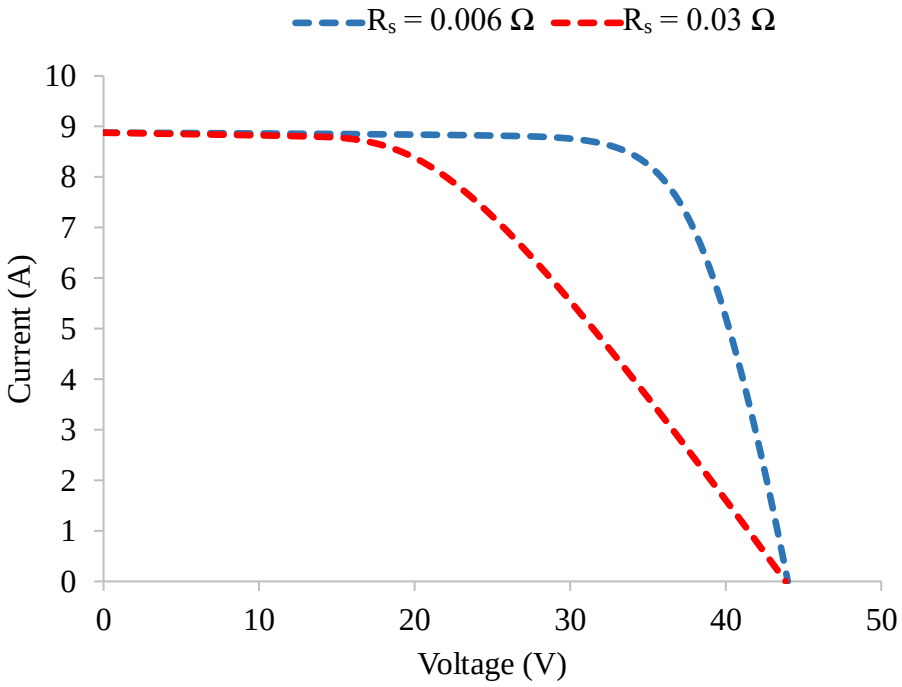

a

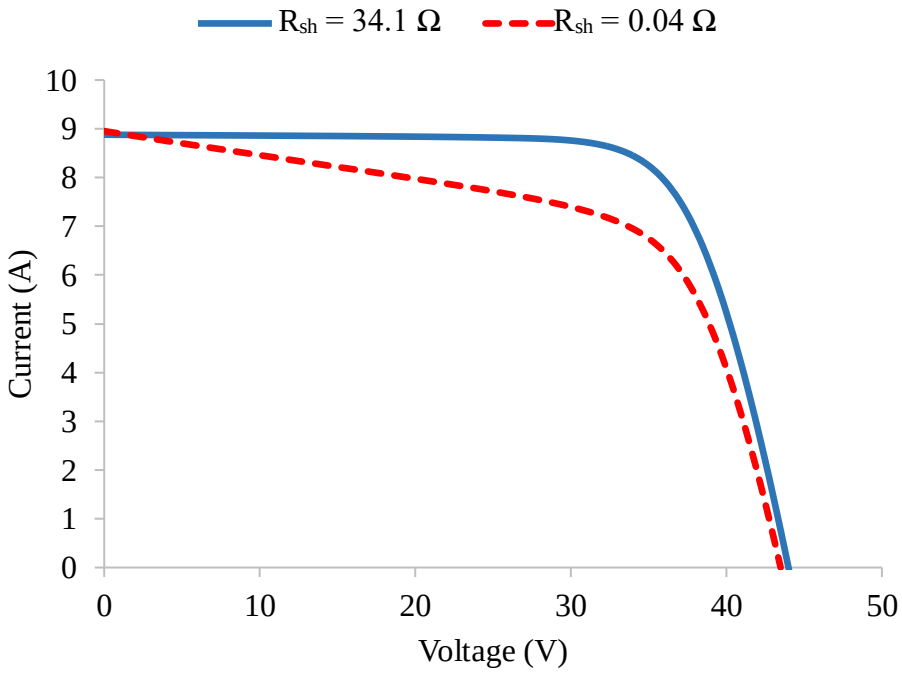

b

Figure 2-12: The modelled I-V characteristics of a PV module showing effects of (a) series resistance and (b) shunt resistance.

2.4 Module configuration in a PV plant

A photovoltaic array is the complete power-generating unit, in PV plants, and consists of several PV modules connected in series, parallel or a combination to achieve the desired power output. Generally, most applications have PV modules connected in series in a string and strings are combined in parallel at a combiner box before being connected to the grid, or load, through an inverter. Figure 2-13 shows a combination of PV modules electrically connected in a typical PV plant layout. In a grid-connected system, the PV generated direct current (DC) is converted to alternating current (AC), by the inverter, and synchronised to the grid, while in stand-alone generators there is no link to the grid but to batteries. The battery bank is charged when the array is generating power and stores energy to be used when the PV modules are not operating, e.g. at night and cloudy weather [1].

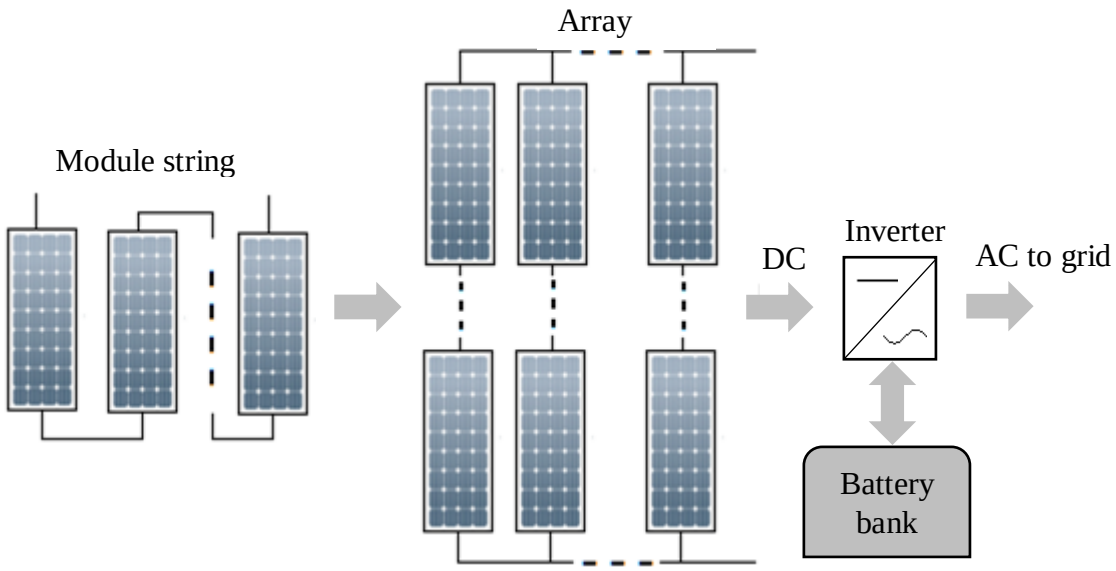

Figure 2-13: Typical interconnection of PV module in the field (adapted from [31]).

The entire module string has effective voltage equal to sum of individual module's voltages. This was confirmed by using PVSim a cell and module simulation program developed by Sandia National Laboratories to model for three modules as indicated in Figure 2-14. If the series connected modules generate equal currents, the string current is equal to the individual module current.

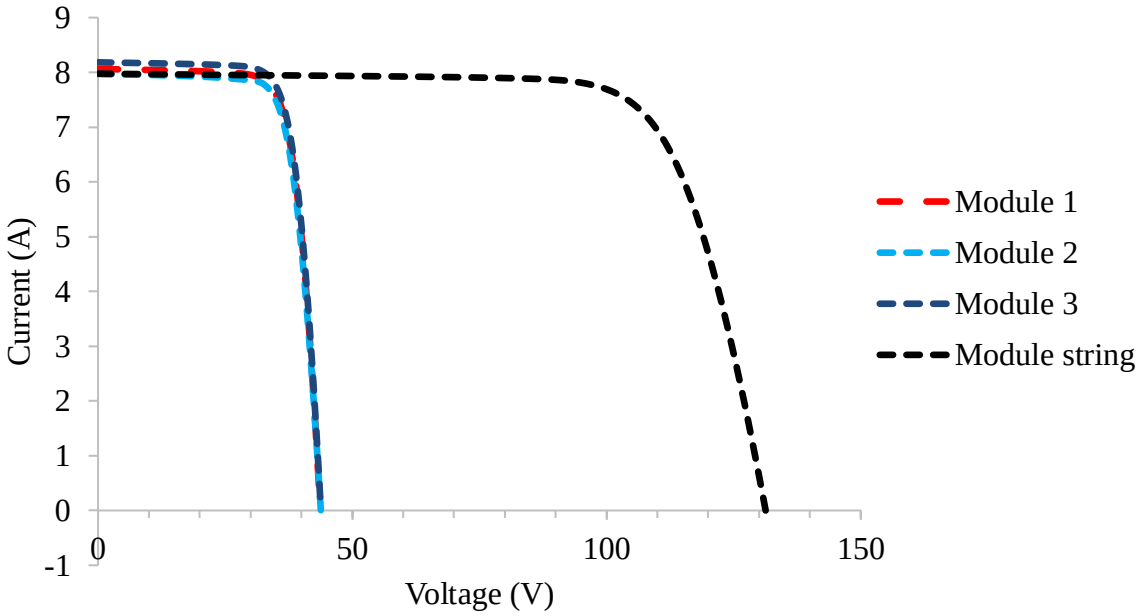

Figure 2-14: Individual and combined I-V curves for three modules connected in series.

When connected in parallel, the currents of the individual modules add up to give the resultant current, while the effective array voltage remain the same as the individual module voltages. Three modules in parallel were simulated for an array arrangement and Figure 2-15 shows the I-V curves.

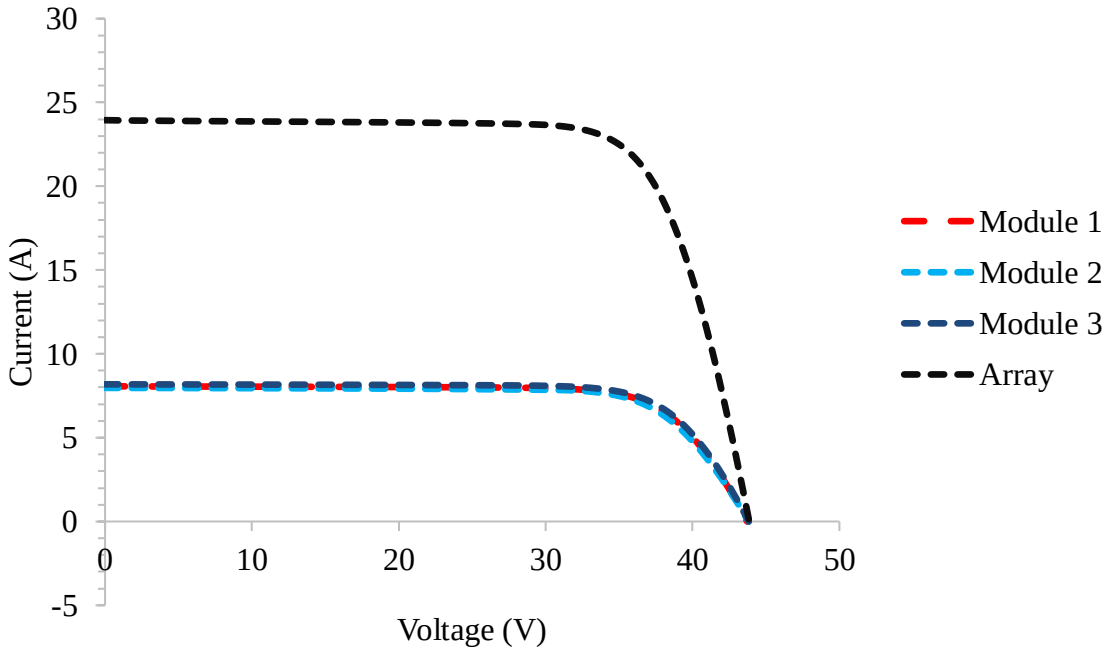

Figure 2-15: Effect of parallel connection, of PV modules, on output current and voltage.

2.5 Mismatch effects in PV module performance

Anomalies in PV modules, such as micro cracks, snail trails, broken fingers and busbars, shunts and weak solder joints, can cause electrical mismatch in PV cells. The anomalies are not always detectable by visual inspection, and mostly if they become visible, the resultant power loss is severe [17]. Current mismatch causes cells to heat up, as discussed in section 2.5.1, and affects the performance of the solar cells. The presence of cracks in modules does not necessarily cause notable power loss [35][40], but in the field, micro cracks on PV modules can develop and spread into larger cracks due to operational conditions and can lead to isolation of cracked parts. This results in significant power loss which depends on crack pattern and the effect can be revealed in a step-shaped I-V curve [17][40].

Mismatch resulting from partial shading on PV modules can be due to soiling or bird droppings. PV modules are deployed outdoors and like any outdoor surface, the modules are prone to dust and bird droppings. Birds find warmth and ideal nesting areas, commonly, in roof mounted PV installations and this means massive bird droppings problems, and this depends with the location of the PV system. PV modules are installed to absorb optimum energy from the sun, and the module's inclination angle contributes to the catchment of dust that is blown by wind [41]. Dust build up on the bottom frame of the module causes shading on the bottom row of solar cells. This soiling tends to be persistent and will often lead to hot spots on the module, as spots of reduced efficiency leading to higher resistive losses in the module. In thin-film PV modules, CIGS or CdTe, the effect of uneven shading of the cells in a module can cause shunts formation on the affected solar cells and result in having an underperforming module [28].

2.5.1 Hotspots in PV modules

If a cell in a substring is defective or shaded it underperforms and produces less current than the substring's expected current and the current of the weak cell presides over the substring, limiting the current flowing to the external circuit. This causes excess current to be forced onto the weak cell due to reverse biasing. The cell acts as load and dissipates electrical power as heat, instead of generating current leading to localised heating called hotspot. This is illustrated in Figure 2-16, where a shaded cell is functioning in series with good cells in a substring. Increasing the shaded area of the cell will reduce the substring's generated current and possibly to the extent of bypassing the whole substring as illustrated in Figure 2-18. The shaded cell will operate at elevated temperature which can result in subsequent failures such as de-soldering of interconnects, discolouration of EVA and module glass cracks [42][17], and in a worse situation irreparable consequences can result when dealing with CIGS technology, as

highlighted in section 4.3.2. Module glass cracks can cause optical inhomogeneity and may lead to scattering of some incident solar irradiation away from the solar cells under the affected area. Moisture ingress through the cracked part may also lead to other defects such as delamination [16]. The hot spots can also result due to resistive flow of generated current caused by broken cell fingers, loose contacts of busbars and module connectors, and if mismatch between cells increases then more power will be dissipated in the weak cell [23].

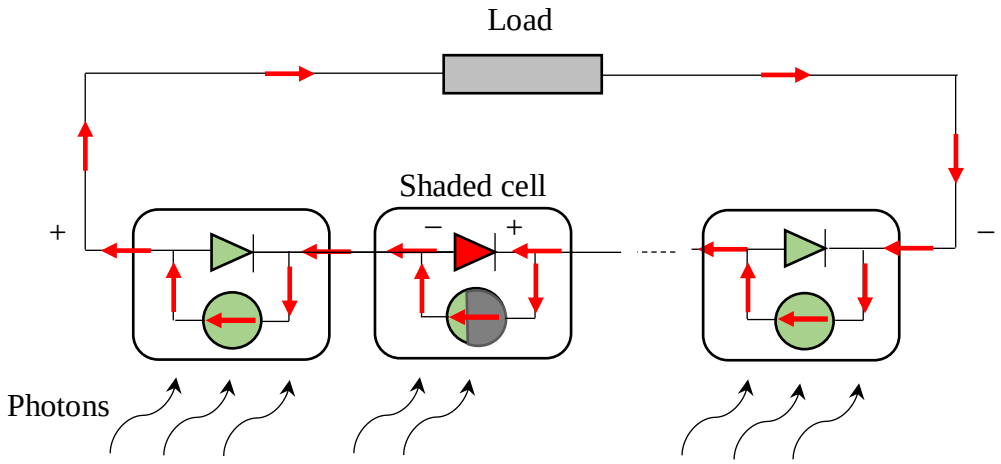

Figure 2-16: Mismatched solar cell in a PV module substring (adapted from [35]).

Similar hot-spotting effects can be observed in a shaded PV module when operating in a module string. In such a case, the mismatched module causes the entire string to operate at a lower current and the excess power produced by the remaining modules is consumed by the defective or partially/fully shaded module. This power consumption leads to an increase in temperature of the abnormal PV module resulting in power deterioration of the module string and the PV plant. Additionally, the formation of hotspots can affect the reliability and reduce the service life span of the PV modules.

Solar cells in a module should have identical electrical characteristics such that they all operate at exactly the same current and voltage when they experience the same insolation and temperature. However, it is impractical, and cells can operate slightly differently even if they are manufactured from the same automated machinery. This mismatch can be due to intrinsic manufacturing defects and impurities and causes some cells to be highly susceptible to light shading than others resulting in hotspots. Ageing solar cells in the field get exposed to nonuniform irradiation due to uneven shading, as discussed in section 4.3, and undergo light and thermal induced degradation which can also contribute to the difference in their operating

points. PV modules manufactured according to high quality control procedures can easily experience mismatch losses due to low mismatch tolerance [17].

The destructive effects of hot spotting can be lessened by using bypass diodes. Figure 2-17 shows the connection of bypass diodes on two substrings in a PV module and if all cells are operating normally, we have same amount of current flowing through each cell as indicated by red arrows.

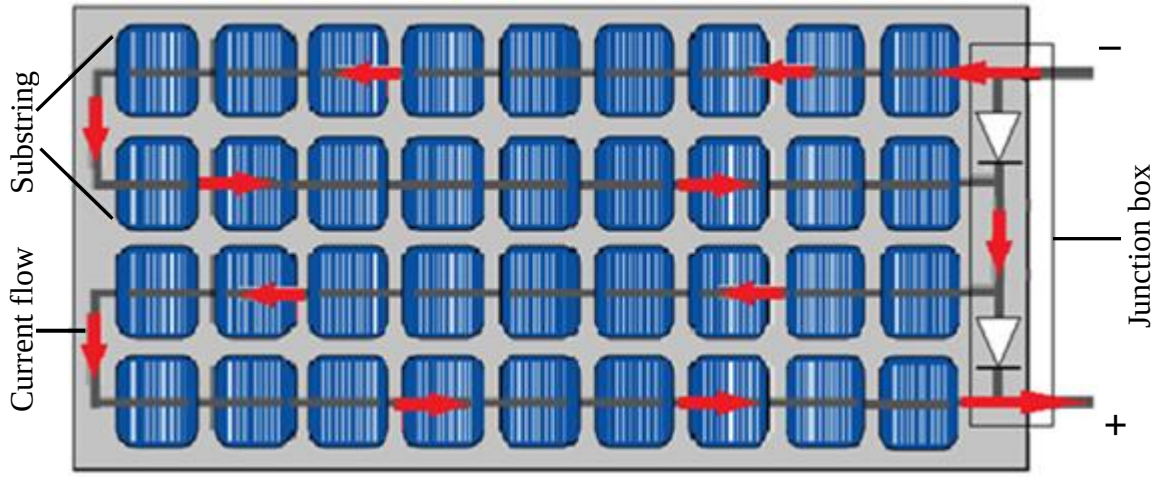

Figure 2-17: Bypass diodes connection and current flow in PV module substrings (adapted from [26]).

When one or more cells are shaded/faulty, the photogenerated current follows the path shown in Figure 2-18. The substring with a mismatched cell will be bypassed by activating a bypass diode parallel to this substring. There now exists a forward biasing potential difference across this diode which makes it conduct [1], and causing the faulty cell not to operate in reverse bias. This will enable smooth operation of the module and protecting the shaded string from hotspot and the module string current is not limited by the weak cell although the loss of power becomes less intense than not using bypass diodes. However, the activation of the bypass diode does not improve performance but only prevent further degradation of the PV module [17], and the impact of bypassing the substring is discussed in next section. The use of bypass diodes is also applicable in module strings, but they are at risk of damage caused by lightning, since solar farms are installed in open areas. “Open” failing of a bypass diode can leave the corresponding underperforming substring vulnerable to a destructive hot spotting, while if it is “shorted” a significant power loss of the module string will be experienced [43][17].

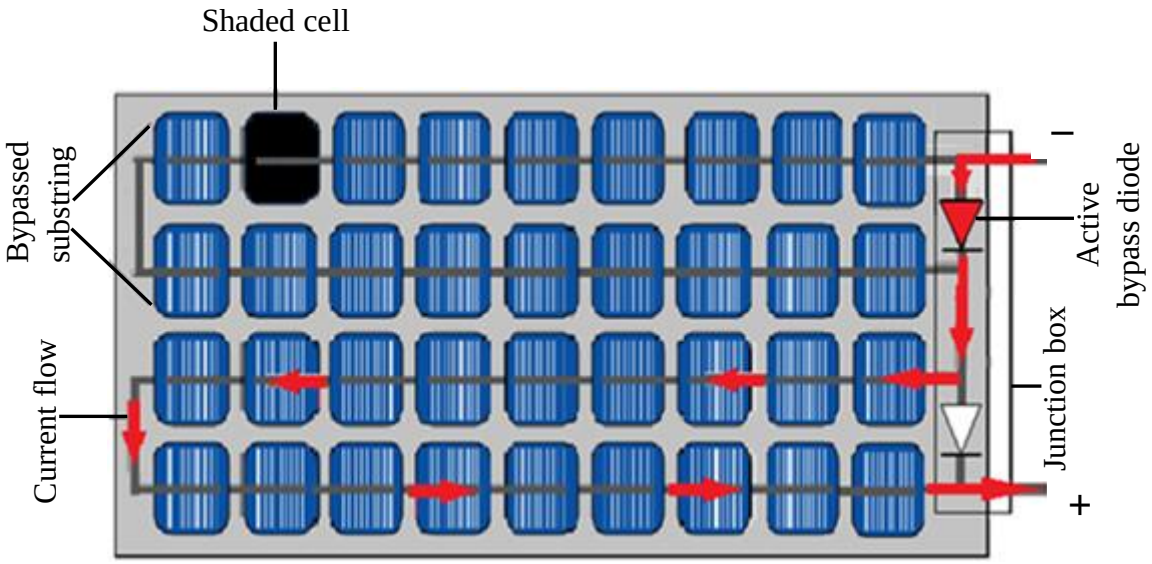

Figure 2-18: Effect of bypass diodes on mismatched solar cell substring.

The current mismatch in PV modules has a significant impact on the I-V curves. It alters the shape of the I-V curve [44], indicating the effect on output power of the PV module. Figure 2-19 illustrates the impact of mismatched solar cell substrings on the voltage and current generated by a PV module. The I-V curves for three substrings (with one mismatched), and a substrings combination (the module I-V curve), were simulated using a PVSim program [30]. The curves, in Figure 2-19 (a) clearly indicate a drop in the current as a result of a faulty substring and the module while V_{oc} of the module equals the addition of the individual substring voltages.

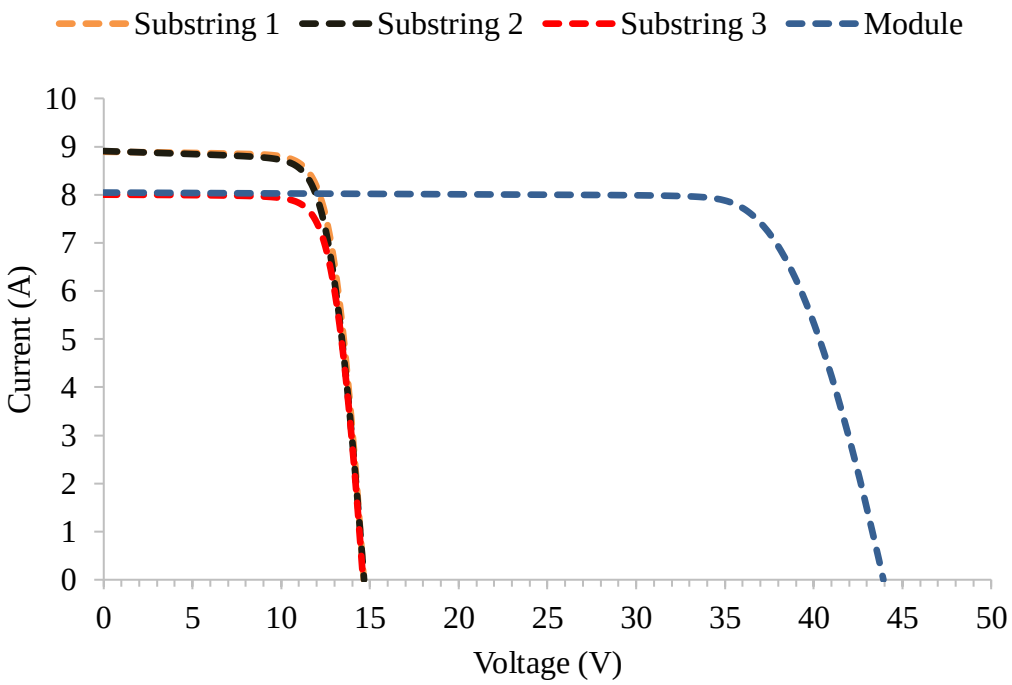

a

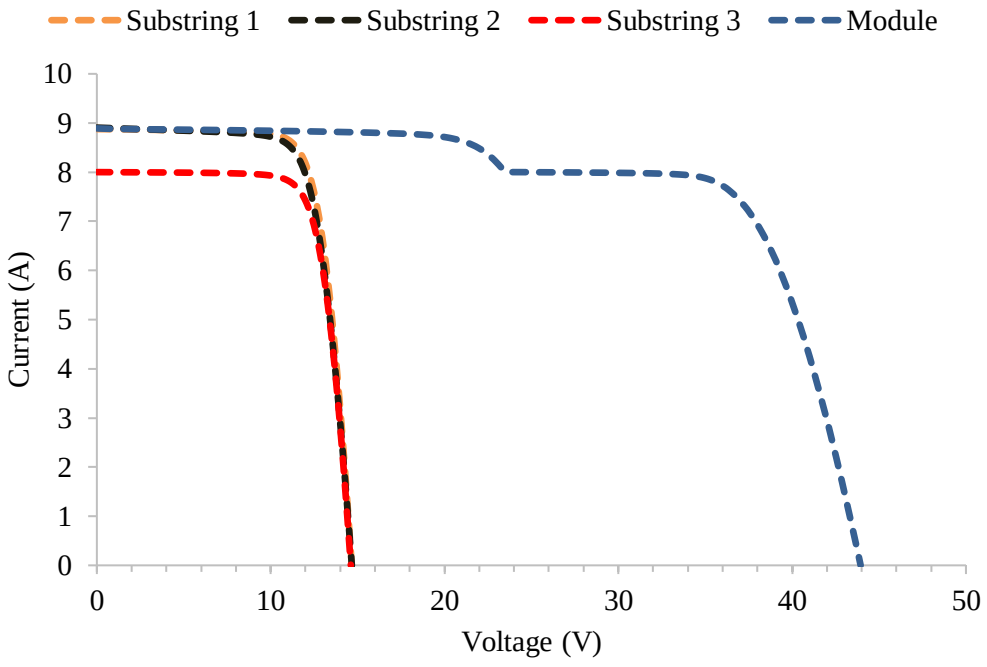

b

Figure 2-19: I-V curves showing the effect of current mismatch in cell substrings (a) without and (b) with bypass diodes.

Figure 2-19 (b) shows the I-V curves when bypass diodes are incorporated. The resultant current is that of the good substrings but the combined or module I-V curve has a step due to conduction of a bypass diode that is in parallel to the mismatched/weak substring. The position of the step relates to the number of activated bypass diodes. When the bump is closer to I_{sc} more bypass diodes will be conducting than when the step is close to the knee [45]. V_{oc} can decreases due to the reduction in the number of substrings which are generating power, e.g. when there is a faulty bypass diode (shorted) across a substring. This will cause the affected substring not to contribute to the module string generated power and the open circuit voltage will be less, by a magnitude of one substring voltage, than the expected. The difference increases as the number of bypassed (or shorted) substrings increases. In the case of having a faulty open bypass diode, the module will suffer power loss, if it experiences substring current mismatch as described earlier, and degrade quickly due to severe hot spotting of the respective substring [17].

PV I-V curve tracers can be used for performance check on installed PV modules in the field and such equipment, e.g Solmetric I-V analyser, can reveal mismatch in cells and modules. Section 3.2.2 outlines how the Solmetric I-V analyser functions. The equipment traces I-V characteristics of a PV source and any deviation from the expected parameters indicates an inefficient string or module [33].

2.6 Thermography

2.6.1 Introduction

Thermal radiation is emitted by all objects of temperature above absolute zero and the heat radiation Q emitted by a body is determined by the body temperature T, the Boltzmann's constant σ and the emissivity ε, according to the equation

$$Q = \sigma \varepsilon T^4. \qquad 2.15$$

As seen in the equation, there is a direct link between the emitted heat energy Q and the fourth power of object temperature, and this principle is applicable in Thermography. TIR Thermography or thermal imaging is about the non-destructive detection and measurement of infra-red (I-R) radiation, which is emitted by the surface of any body. The emitted I-R energy is converted to temperature, by thermal cameras, and represented in the form of thermal images [46]. Most failures in equipment are signalled by a significant rise in operating temperature and the heat patterns can help identify malfunctioning parts before they completely fail. The non-

contact nature of TIR thermography makes it ideal for many applications and in recent years it is widely applied in inspecting abnormalities on in-situ PV modules [47].

2.6.2 TIR thermography on PV modules in the field

Conventional condition monitoring and performance evaluation of commercial, operating PV modules is mainly based on electrical measurements or computer simulation models [48], which display lack of fault detection ability. However, the temperature-based monitoring technique (TIR thermography) can indicate any performance limiting anomaly of an operating PV module. Field TIR thermography measurements of PV modules are performed outdoors, under steady state solar illumination, i.e. clear sky and low air flow and, under such conditions, heat and electricity are generated by the incident irradiance which, in the case of a good PV module, is expected to cause homogeneous temperature distribution on the module surface. Since the majority of occurring faults have a significant impact on the thermal pattern of the PV module, they are detected as inhomogeneities of the temperature distribution and can be seen in thermal image of the defective module. This way, any source of dysfunction or hot spot heating can be located. Elevated temperature of singular spots, cells, substrings or modules can be observed and highlight irregularities which have a substantial effect on the performance, reliability and longevity of PV module strings [17][19].

Figure 2-20 shows the effect of uneven shading by neighboring PV modules which was identified after TIR imaging. It can be noted that the partially shaded cells are at abnormally higher temperature than the background module temperature. Such a thermal signature can be used for quantitative diagnosis by estimating the electrical power output losses of the impacted module or string.

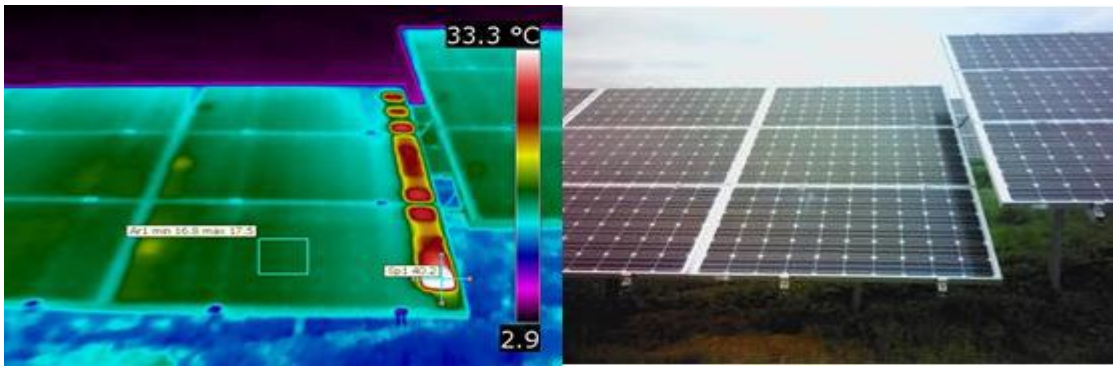

Figure 2-20: Hot cells due to non-uniform shading by the top row of PV modules [27].

TIR thermography is also suitable to detect Potential Induced Degradation (PID) in an illuminated PV array. The resultant thermal pattern of a PV module with PID presents cells which are slightly warmer and usually the cells will be on lower parts and parts close to the module frame as shown in Figure 2-21.

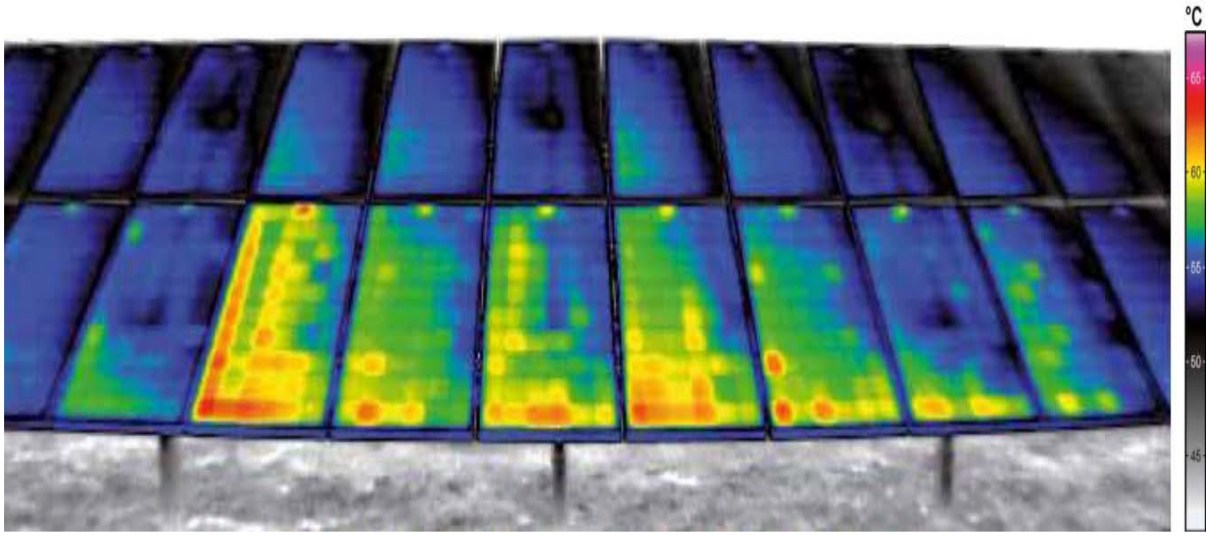

Figure 2-21: TIR image of operating PV module array having modules suffering PID [17].

According to Hoyer et al, a significant temperature difference (ΔT) of 5 ^{o}C or more between an anomaly (faulty cell or interconnect) and a reference module temperature indicates a thermal signature which has the potential to reduce the performance of the module. Considering equation 2.15 (Stefan-Boltzmann black body law on radiative heat transfer), the relation between the additional dissipated power (ΔP) and the consequent temperature rise (ΔT) in the defective/mismatched cell can be given by the following equation [49]:

$$\Delta P = \varepsilon \sigma A \Delta T^4 \qquad 2.16$$

where A is the hot area and ΔT is the increase in the cell temperature (in K) due to hot spot heating.

TIR cameras give the temperature of a PV module in relation to the emitted radiation. However, there are some parameters which may influence the measurement of temperature of the module under study resulting in thermal cameras receiving radiation from the surroundings. The parameters such as emissivity, reflection radiation, atmospheric temperature and humidity must be considered when thermal imaging the PV modules to minimize errors. Typical emissivity values of the glass and back sheet polymer of the PV modules are 0.85 and 0.95 respectively

and have to be correctly entered into the I-R camera software before measurement. Other aspects to take into account are I-R camera resolution and most important the angle of capturing the PV modules thermal data. The I-R camera should be approximately perpendicular to module surface. These factors apply for both ground TIR thermography, using a hand held I-R camera, as well as aerial UAV or drone based TIR imaging and in aerial thermography, using a UAV, it is recommended to consider the flight height and speed of the drone as they can cause blurring on the thermal images [50][27].

Thermal with the corresponding EL images of a module that confirm the effect of electrically isolating cracks causing mismatch are shown in Figure 2-22. It is important to note that electrically isolated portions of cells cause current mismatch in relation to fully operational cells, as highlighted in section 2.5. To maintain the same electrical current through a series connected module substring (with functioning bypass diode), a mismatched cell's operational current-voltage point will change depending on the level of mismatch and the actual operational current-voltage point of the substring. The activation of bypass diodes will influence the operational point of a substring that will consequently dictate the individual operational points of each cell in the substring. When a mismatched cell's operational voltage shifts to reverse bias in an effort to maintain the substring current, the cell will heat up (resistive heating) and can be identified on the TIR image. When the operational voltage of a mismatched cell remains positive, the moderate non-resistive heating may not be detected on the TIR images. The resulting temperatures of the cells will depend on the individual cell I-V parameters and the conditions of measurement [27][50].

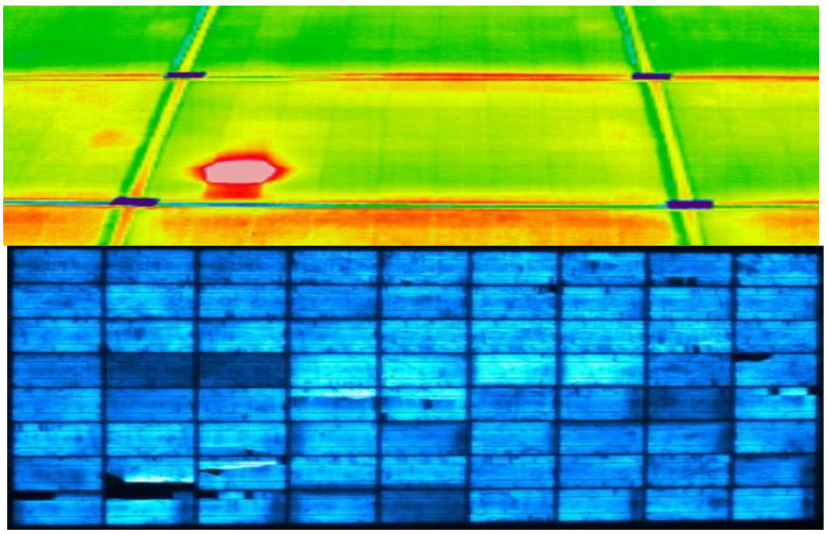

Figure 2-22: TIR image and a corresponding EL image revealing a fractured cell [50].

Table 2-3 highlights some possible abnormalities in operational PV modules which were identified after thermal imaging, according to IEA-PVPS: Review of Failures of Photovoltaic Modules [17],.

Table 2-3: Defect classification in PV module TIR imaging [17].

Class	Pattern	Description	Possible irregularity
A		Module at elevated temperature	Disconnected Module (open circuit)
B	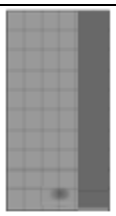	Overheating of cell string (substring)	Mismatched substring (string bypassed)
C	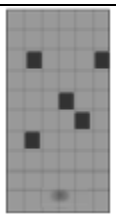	Single cells at elevated temperature are randomly distributed in a "patchwork pattern" across cell strings and have significant ΔT	Several partial cell disconnects resulting in severe mismatch
D	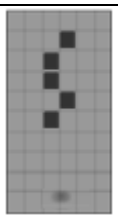	"Patchwork pattern", Cells at elevated temperature are randomly distributed in same cell string and have significant ΔT	Several partial cell disconnects resulting in severe mismatch
E	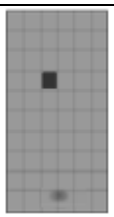	Single cell overheating	Defective or delaminated cell

Table 2-3 continued.

Class	Pattern	Description	Possible irregularity
F	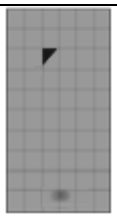	Part of a cell is warmer	Portion of cell is electrically inactive (broken cell or cell interconnect)
G		Uneven heating or overheating at specific points on cell or areas of module	Optical impediment (shading) or delaminated cell
H	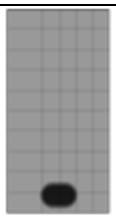	Hot junction box	Faulty connection on junction box

2.7 Summary

Doping of semiconductor materials improve their electrical properties. The PV action which occurs when photons fall on p-n junction was discussed. A number of solar cells are electrically linked in series in a module or string to increase the system voltage. It was shown that the output parameters of a PV cell, module or string can be affected by several module anomalies and operational conditions such as irradiance and temperature. The impact of the irregularities on module performance was reflected on the I-V curves. Abnormal operation of PV modules can result in mismatch which cause non-uniform temperature distribution in the module and can be revealed by UAV TIR imaging as hot areas. The hot-spotting cause detrimental effects such as module glass cracks, delamination, burns and increase the rate of module deterioration. However, the integration of bypass diodes in mc-Si modules, minimise the impact of thermal signatures. Different patterns of thermal signatures due to several module/cell irregularities were also discussed.

Chapter 3

Experimental Details

3.1 Experimental solar PV plant

The experiments were conducted at Eskom Research and Innovation Centre (ERIC) in Rosherville, Johannesburg, South Africa. Eskom is a South-African power company that generates electricity and distributes it to consumers [51]. The ERIC Solar PV system has an installed capacity of 400 kWp and has been in operation since January 2015. It occupies an area of approximately one hectare on which multi-crystalline silicon (mc-Si) and copper indium gallium selenide (CIGS) thin-film modules are installed in different orientations. The PV plant was designed to test the energy yield of different technologies in the following configurations and orientations [52],

- Area 100 – Crystalline Silicon Fixed North Facing
- Area 200 – Thin-film Fixed North Facing
- Area 300 – Crystalline Silicon Fixed East and West Facing
- Area 400 – Thin-film Fixed East and West Facing
- Area 500 – Crystalline Silicon Tracking North to South
- Area 600 – Crystalline Silicon Tracking East to West
- Area 700 – Thin-Film Tracking East to West.

The ground mounted PV modules feed the generated power to the local electricity distribution grid. The modules are labelled according to their position on the plant's site map, e.g. area 100, inverter 2, string 4, module 7 (A100-Inv2-ST4-M07), which made it easier for locating, inspecting and testing the strings and modules. Nine or ten CIGS modules are connected in series to make up a string, whereas in each mc-Si string there are fourteen modules. Several strings of CIGS modules are paralleled at a combiner box before feeding electrical power to an inverter and the grid [52]. Figure 3-1 shows an aerial view of the mc-Si and CIGS modules at ERIC plant.

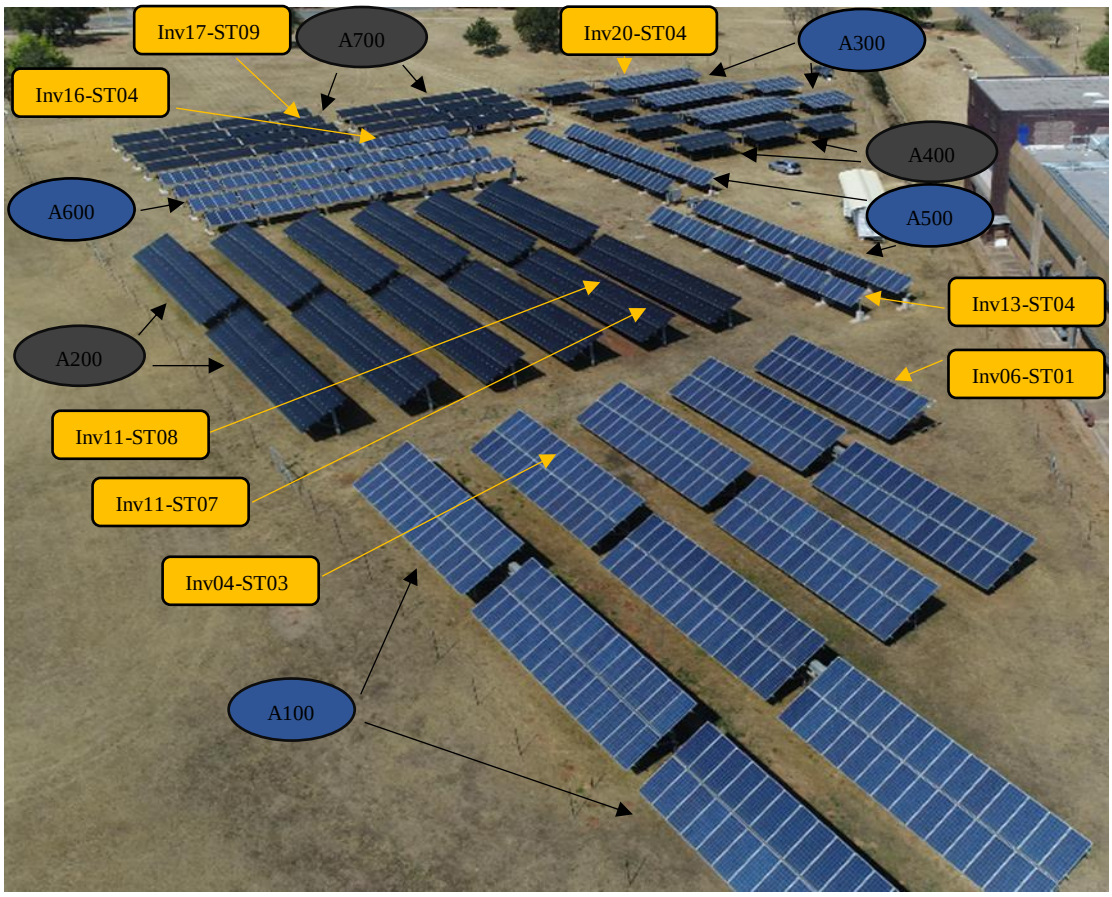

Figure 3-1: Aerial view of ERIC Solar PV plant facility. Source: Hawk62 Aviation.

3.1.1 ERIC PV module specifications

The mc-Si modules have three substrings, and each consists of 24 solar cells, thus 72 series-connected cells in one module. Each substring has a bypass diode in parallel over it. A CIGS module consists of 133 monolithically series connected solar cells and has no bypass diodes. The manufacturer's specifications of the mc-Si and CIGS modules are given in Table 3-1. The solar cells in mc-Si modules are laminated between glass and back sheet while in CIGS modules there is glass to glass protection of cells.

Table 3-1: Details of PV modules at ERIC plant.

Specifications	**Technology**	
	mc-Si	CIGS thin-film
Manufacturer	Astronergy	tsmc solar
Model	CHSM6612P-300	TS-145C2
I_{sc}	8.9 A	2.6 A
V_{oc}	45.2 V	86.0 V
I_{mp}	8.4 A	2.3 A
V_{mp}	35.7 V	63.6 V
P_{max}	300 Wp	145 Wp
α (%/°C)	0.087	0.010
β (%/°C)	-0.332	-0.290

3.2 Data Acquisition at the PV plant

The experimental data was obtained by first carrying out thermal imaging, then visual inspection and lastly taking I-V measurements of the module strings under study. The procedure is given in sections 3.2.1 and 3.2.2.

3.2.1 Aerial Thermography

Thermal Infra-Red (TIR) recordings of operating PV modules were obtained with the use of a lightweight camera mounted on a remote-controlled UAV/drone. The camera utilised was a Flir Tau2 640 and enabled simultaneous capturing of TIR and visual images. The camera specifications are listed in reference [53]. Figure 3-2 shows the UAV with integrated IR camera used for the generation of the aerial TIR data.

Figure 3-2: UAV with I-R camera used for monitoring PV module strings at ERIC. Source: Hawk62 Aviation.

TIR imaging of the operating PV modules, in strings, was carried out in September 2017 under steady conditions, with high incident solar radiation that ranged from 708 to 1242 W/m^2, under a cloudless blue sky and low wind flow. The automatic settings in the IR camera facilitated geometric resolution adjustments while flying the drone. The flying altitude was set, and the drone was flown, remote controlled, above the operating PV module strings. The capturing angle of the IR camera on the drone was set to be almost perpendicular to the module surface, to minimise disturbing reflections especially from the sky. Figure 3-3 shows the acceptable angles (green) for setting the IR camera and the angles (red) which were avoided, as advised [54].

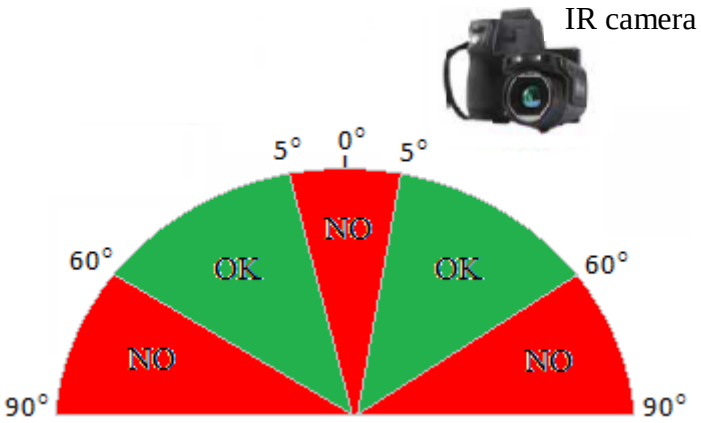

Figure 3-3: Recommended positioning of an IR camera on aerial thermal imaging of PV modules (adapted from [55]).

Remote controlling of the drone and capturing of images was performed by qualified personnel from HAWK62. The procedure outlined in flow chart in Figure 3-4, was followed in analyzing and categorizing the thermal images obtained. In this work any non-shading anomaly on a PV module that caused a temperature rise (ΔT) of $\geq 5°C$ on the affected cell was considered a defect and the strings which contain the 'defective' modules were termed 'defective' strings.

Optical images, from the selected PV module strings, were used in trying to locate and determine the nature of the visible anomalies causing thermal irregularities in the PV modules, such as cracked glass, soiling or other impediments and defects. The strings which contained the affected modules in each string were noted and a comprehensive visual inspection was carried out under good lighting and as recommended in reference [17]. The front and back surfaces of the defective modules were inspected to determine any optical impediments or any module irregularities causing hotspots. After visual inspection the I-V characteristics of the PV modules and strings were measured as outlined in the following section.

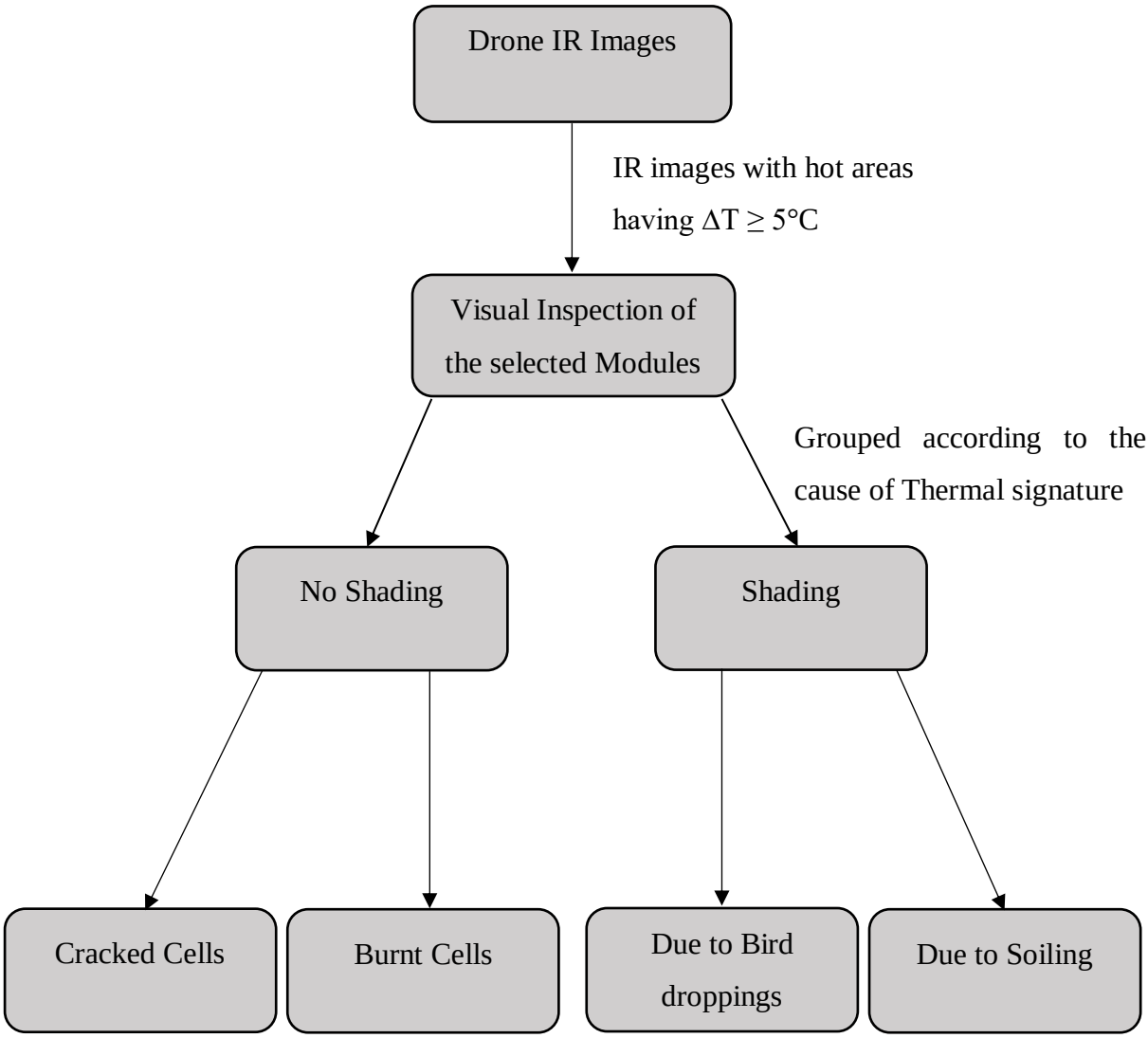

Figure 3-4: Classification of defective modules.

3.2.2 I-V measurements

A portable Solmetric Photovoltaic Analyzer, model PVA-1000S-30, was used for measuring the I-V characteristics of the PV modules and strings at the ERIC PV plant. This was carried out on a different day to the day to capturing of TIR images. The PVA analyser's hardware consists of:

- Laptop computer (PC)
- Wireless interface
- I-V measurement unit with test leads
- SolSensor unit for measuring solar irradiance and temperature
- 2 x type K thermocouples.

The PV module strings were isolated from the inverter by opening the DC coupler/disconnect switch and the Solmetric PV analyser hardware was set up as shown in Figure 3-5. The SolSensor unit, which measures irradiance and module temperature, was clamped on the frame of one module in the string to be tested. This enabled the unit to be at the same inclination as the modules under test and hence measure plane-of-array irradiance. Type K thermocouples were used to measure the module temperature and estimation of the string temperature. The tip of each thermocouple (TC 1 and TC 2) was attached, making a firm contact, at the backside of the module. Figure 3-6 shows TC 1 and TC 2 taped a third of the distance along the diagonal as recommended. The thermocouples were not placed near the module frame (Figure 3-7) since it is cooler at the edges of the module [56]. The average of these two temperatures is used as the temperature for the entire string, using the assumption that the modules in the string are operating at similar temperatures.

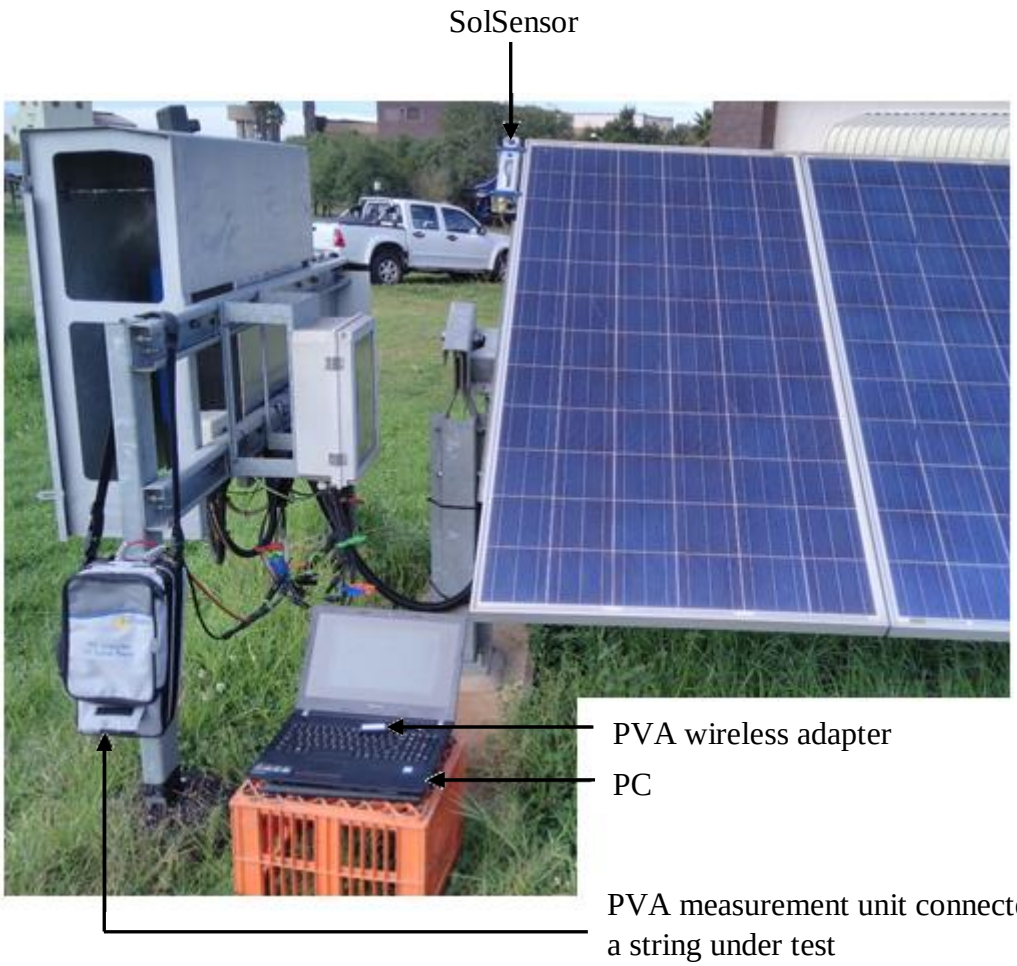

Figure 3-5: PVA-1000S-30 equipment set up for I-V measurement of mc-Si module string at ERIC plant.

Figure 3-6: Type K thermocouple tips stuck diagonally on the backside of a PV module and a SolSensor unit at same inclination angle as the modules.

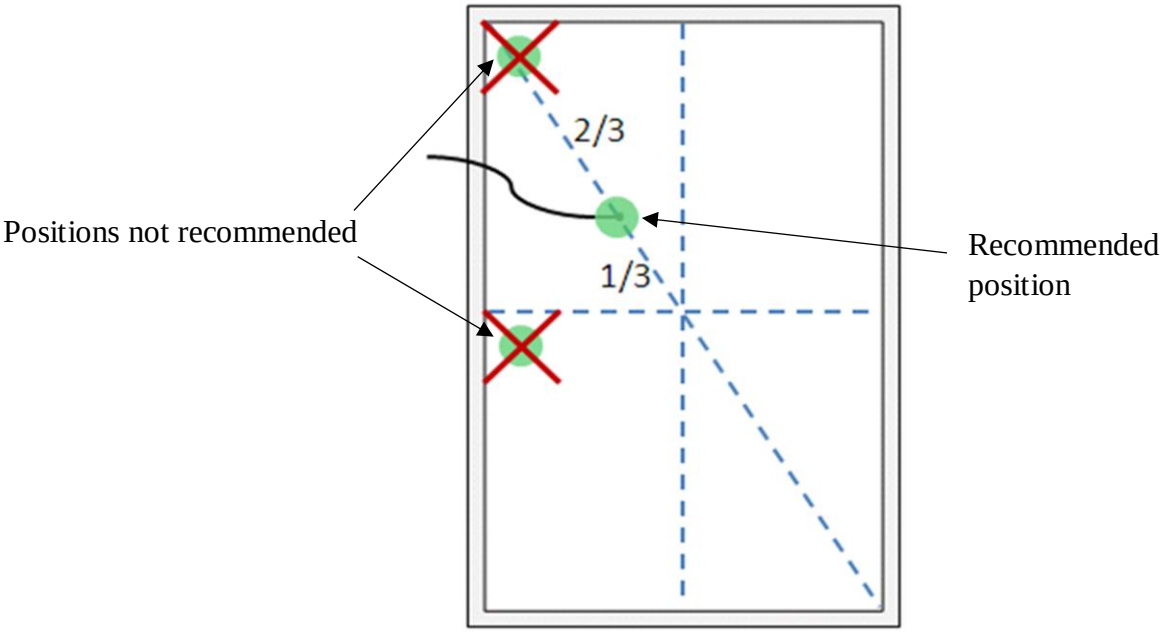

Figure 3-7: Recommended placement of thermocouples on backside of a PV module [57].

The PVA I-V measurement unit was connected to one module string, using the test leads and the PVA software was launched on the PC to measure the I-V parameters of the selected string. The SolSensor and the PVA I-V measurement unit were linked to the PC via a wireless PVA interface. The performance model was set up and involved selecting the PV module type, entering the number of modules in series and number of strings per inverter or combiner box, then I-V parameters were measured. The I-V trace points were measured by sweeping the load, in the I-V measurement unit, on a PV source over a range of currents and voltages. The PVA curve tracer accomplished this by loading the string or module, under test, at different points across its operating range between 0 V and V_{oc}. At each point, the output current and voltage were measured simultaneously [57].

The measured I-V values of the PV modules and strings were corrected to STC using equations 2.9 and 2.10 and the current and voltage correction factors in Table 3-1. The acquired IR data was analysed with respect to significant temperature abnormalities and correlated to the I-V characteristics (STC corrected) of the relevant PV module string in order to estimate the string power loss associated with the thermal signatures. In analysing the module and string I-V characteristics, the performance parameters obtained from non-defective modules and strings were used for reference.

The International Guidelines of Uncertainty in Measurement (GUM) [37], were used for calculating the combined uncertainty of the performance parameters of the strings and modules. The combined percentage uncertainties, due to field measurements and STC translation methods, were calculated using the root-sum-of-squares method for all standard uncertainties. The uncertainties used in the calculations are listed in Table 3-2 and were obtained from manufactures specifications, and α and β values in Table 3-1 were considered in obtaining uncertainties due to STC translations where equations 2.11 and 2.12 were used.

Table 3-2: PVA-1000S-30 equipment uncertainty specifications [56].

Parameter	Uncertainty	Relative Uncertainty
Voltage accuracy	±0.25 V	±0.5%
Current accuracy	±0.04 A	±0.5%
Temperature accuracy	Typically, less than 2°C	
Irradiance accuracy		±2%
Illumination non-uniformity	Typically, less than 2°C	

To understand more about the performance of module strings containing a module having thermal abnormalities due to soiling, an experiment was carried out at Outdoor Research Facility (ORF) at Nelson Mandela University in Port Elizabeth. The approach used is described in section 3.3.

3.3 Soiling Simulation at ORF

The experiment was conducted to simulate different non-uniform soiling scenarios that were observed at the ERIC PV plant. The ORF consists of ground mounted fixed North facing PV modules which feed the grid. The experiment was carried out on a string of 14 series connected poly-crystalline Silicon modules which are a similar configuration to those at ERIC plant, but with a smaller 60-cell module. The equipment set up is shown in Figure 3-8 and Figure 3-9, and TIR imaging and I-V measurements were taken under the required conditions [50]. The sky was clear and the pyranometer measured irradiance of around 850 W/m^2.

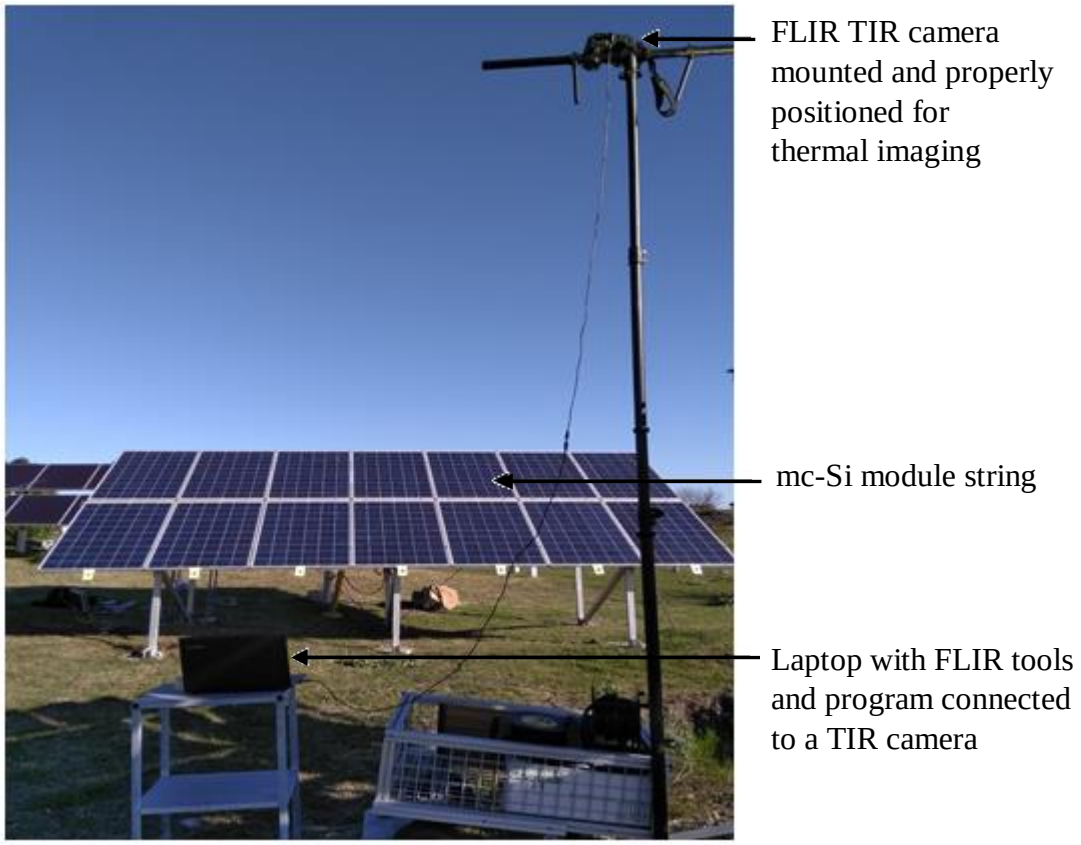

Figure 3-8: Thermal imaging equipment set up at ORF.

Figure 3-9: I-V measurement equipment set up at ORF.

In order to simulate the soiling scenarios, soft dough made from flour and water was used to resemble bird dropping while flour powder resembled light soiling which build up on bottom edges of inclined PV modules. After setting up the thermal camera as shown in Figure 3-8, soft dough was put on one cell of module 2 as shown in Figure 3-10 (a) to create light shading, and a thermal image of the partially shaded module was taken while the module string was generating power. The PV source was disconnected from an inverter and I-V characteristics of the string were measured while the dough was still on the cell. The equipment used for measuring the I-V parameters is shown in Figure 3-9 and consisted of an analyser from the PV-Engineering company. Heavy shading was then applied on the light shaded solar cell by applying more dough to the same area to reduce the amount of light reaching the cell. A thermal image was taken, and I-V characteristics of the string were again measured. Light and heavy shading are shown in Figure 3-10 (a) and (b) respectively. The shaded module 2 was cleaned to remove dough and reference I-V measurements were taken from the module string. Dry flour powder was used to partially shade the bottom cells of module 3 as shown in Figure 3-10 (c) and the procedure for TIR imaging and I-V measurement was repeated. The I-V measurements obtained were normalised and correlated to the respective thermal signatures of the partially shaded modules. The results are presented and discussed in section 4.6.

light shading | heavy shading | bottom shading

a | **b** | **c**

Figure 3-10: Soiling simulation on poly-crystalline PV modules at ORF.

3.4 Summary

UAV thermography is a non-destructive technique used in locating irregularities in operating PV modules. The anomalies were reflected as hot areas and the actual causes of the thermal signatures were identified on visual inspection. I-V measurements of selected modules and strings were taken and corrected to STC. Detailed analysis of the thermal signatures and output parameters of the module strings was carried out. The soiling experiment was carried out at ORF to simulate shading that was observed at ERIC and to have a more in-depth understanding of partial shading on performance of the mc-Si modules.

Chapter 4

Results and Discussion

4.1 Introduction

Thermal images obtained after the testing procedure highlighted in chapter 3 showed temperature irregularities in some modules resulting in abnormalities in PV module operation. The anomalies that resulted in hotspots and hot cells on PV modules correspond to and include module cover glass cracks, shaded cells and burn marks on the back sheet. These features are discussed in the following sections. Not all features that caused temperature inhomogeneity in a module correlate to visually observed features.

4.2 Effect of cracked modules on string performance

4.2.1 Impact of a shattered module on mc-Si string performance

When cracks in cells electrically isolate parts of the cell causing current mismatch, as discussed in chapter 2, thermal irregularities may be observed in the affected module while the module is operating at irradiance levels above 600 W/m^2 [27]. One module, M02, in string A500-Inv13-ST04 was identified in thermal imaging because of hot cells which are randomly distributed in all substrings in a patchwork pattern. The hot cells show a significant ΔT of 66.1°C with one of the substrings (on the left side of the module) appearing to be hotter than the other two as shown in Figure 4-1 (a). Subsequent visual inspection indicated that this module was the only module in the entire string that had experienced physical damage with the cover glass shattered as indicated in Figure 4-1 (b). The output of the entire string was affected by the damaged module as seen in Figure 4-2.

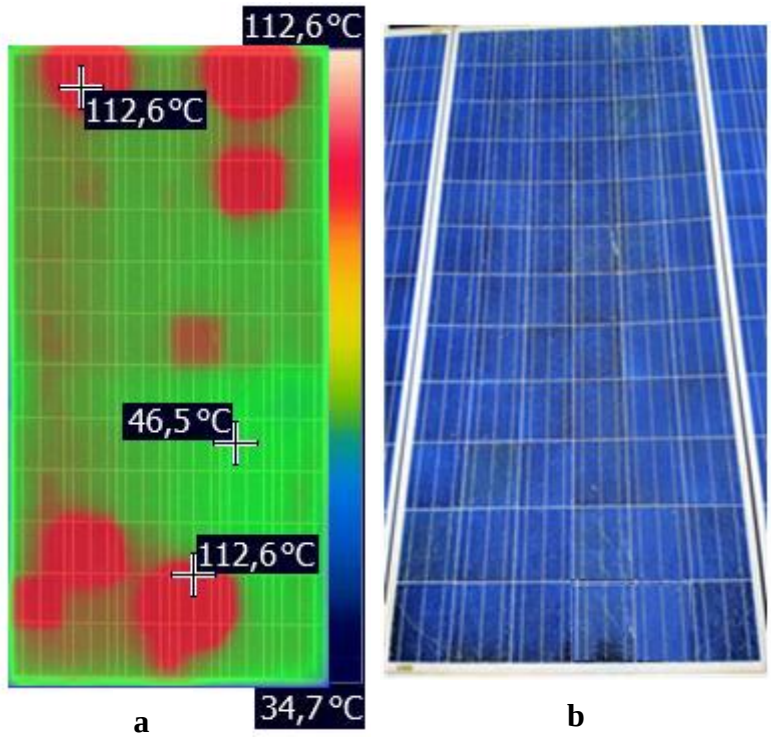

Figure 4-1: (a) Thermal and (b) visual images of a shattered module in a mc-Si module string, A500-Inv13-ST04.

The I-V curve of the module shown in Figure 4-2 (a), shows a feature revealing that at least two of the three module substrings produce a lower current than an undamaged module would produce. Thus, two bypass diodes are conducting current as a result of severe cell mismatch caused by the damaged cells and interconnects as described in section 2.5. The module glass breakage resulted in some parts of the cracked cells to be electrically isolated, affecting the performance of the module as indicated by a reduction in FF and a power loss of 54 W (19.6%), shown in Table 4-1. The shape of the I-V curve of the damaged module can be seen mirrored in the I-V curve of the entire module string thus also translating the drop in power to the string. This is indicated by the bumps in the defective string I-V curve in Figure 4-2 (b). The voltage difference of more than 50 V between the two observable bumps suggest that that two modules may be causing current mismatch in the string. The left bump relates to module causing a current mismatch of less than 0.5 A while the right hand bump relates to the shattered module causing a current mismatch of approximately 2.5 A. Comparing to a reference string A500-Inv13-ST03, the shattered module caused the affected string to underperform by 294 W (7.6%) as shown by the calculated parameter difference between the reference and the defective (ΔP) in Table 4-2.

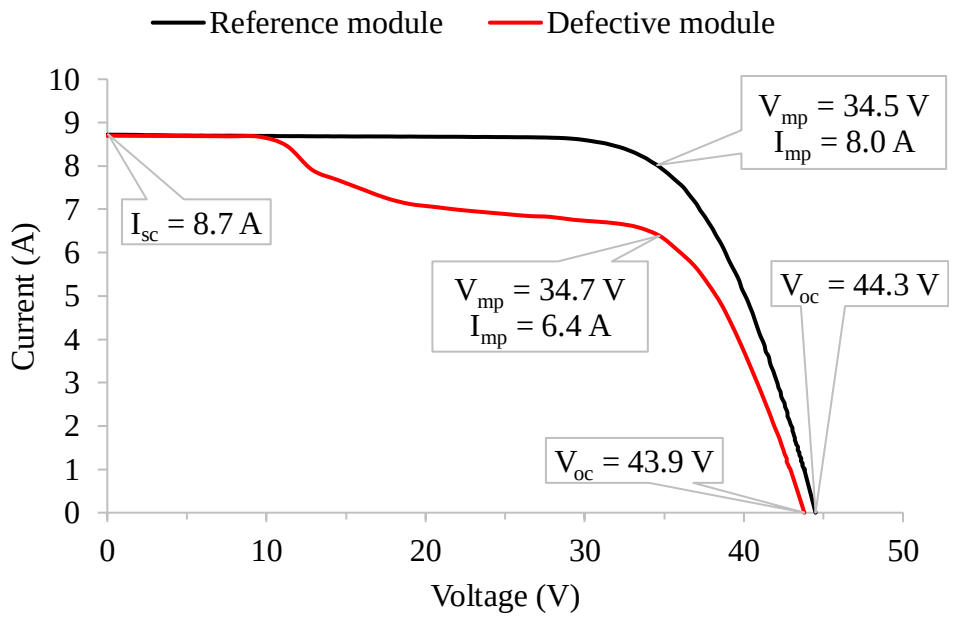

a

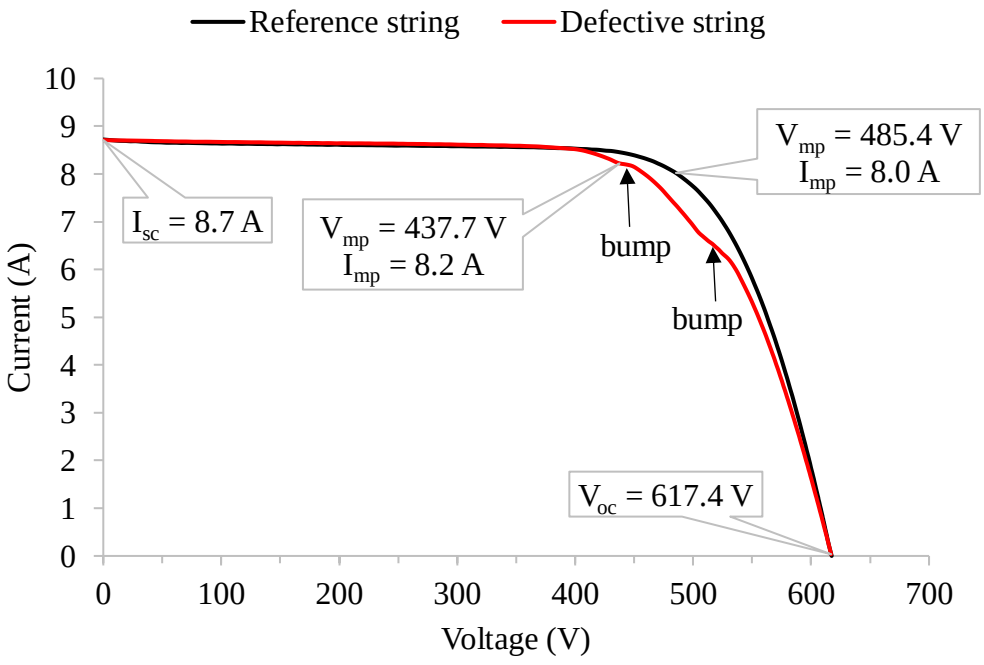

b

Figure 4-2: I-V curves of defective and reference modules (a) and defective and reference strings (b).

Table 4-1: Performance parameters of defective and reference modules of mc-Si technology.

Module	I_{sc} (A)	V_{oc} (V)	I_{mp} (A)	V_{mp} (V)	FF	P_{max} (W)
A500-Inv13-ST04-M02 Defective	8.7±2.1%	43.9±1.1%	6.4±2.2%	34.7±1.3%	0.58	222±3.7%
A500-Inv13-ST04-P01 Reference	8.7±2.1%	44.3±1.1%	8.0±2.2%	34.5±1.3%	0.72	276±3.7%
ΔP (%)	0.0±2.1	0.90±1.1	20±2.2	1.68±1.30	0.14	19.6±3.7

Table 4-2: Performance parameters of defective and reference strings of mc-Si technology.

String	I_{sc} (A)	V_{oc} (V)	I_{mp} (A)	V_{mp} (V)	FF	P_{max} (W)
A500-Inv13-ST04 Defective	8.7±1.8%	617.4±0.9%	8.2±2.7%	437.7±1.1%	0.67	3589±3.2%
A500-Inv13-ST03 Reference	8.7±1.8%	617.4±0.9%	8.0±2.7%	485.4±1.1%	0.72	3883±3.2%
ΔP (%)	0.0±1.8	0.0±0.9	2.5±2.7	9.8±1.1	0.05	7.6±3.2

The string underperformed by approximately 7.6% and continued operation under conditions of elevated cell temperatures. The high temperatures can result in complete module failure since the hot-spotting is degenerative. Also, module glass cracks obstruct solar radiation incident on the solar cells, adding to the cell and module string current mismatch and affecting the energy conversion efficiency. The environmental factors such as wind and rain can mechanically impact on the defective module's surfaces and intensify the damage by elongating and deepening the glass cracks which can strip and disconnect the already weak cells and interconnects, consequently further reducing the output power of the string. Water ingress may also cause ground faults causing the inverter to trigger a safety switch. This may finally lead to the string of fourteen modules not contributing to the PV plant's output energy. Furthermore, the presence of glass breakages poses a safety risk to plant operators and can

result in fire and destruction of the installation as a result of overheated cells. Thus, it is very important for the effective and safe operation of a PV plant that the damaged module be replaced as soon as possible.

4.2.2 Performance of CIGS strings with cracked modules

In string A200-Inv11-ST08 module M03 was observed to have hot cells while the other modules in the same string did not have hot areas visible in the thermal images. The thermal and optical images of the affected module are shown in Figure 4-3. The optical image shows visible glass cracks that run diagonally across almost all cells. No other optical impediment causing current mismatch was identified during visual inspection. From the photograph, the diagonal cracks are clearly visible on parts labelled X but less noticeable on parts labelled Y. The hot cells and the normal operating cells have a temperature difference (ΔT) of 18.5°C. The CIGS modules and strings do not use bypass diodes to mitigate the effect of current mismatch on cells with the result that no bumps are observed in the I-V curves. The I-V curve of the defective string shown in Figure 4-4 shows an increased shunt slope and a decrease in V_{oc} when comparing with the reference string's I-V curve, thus indicating that the defective string is underperforming.

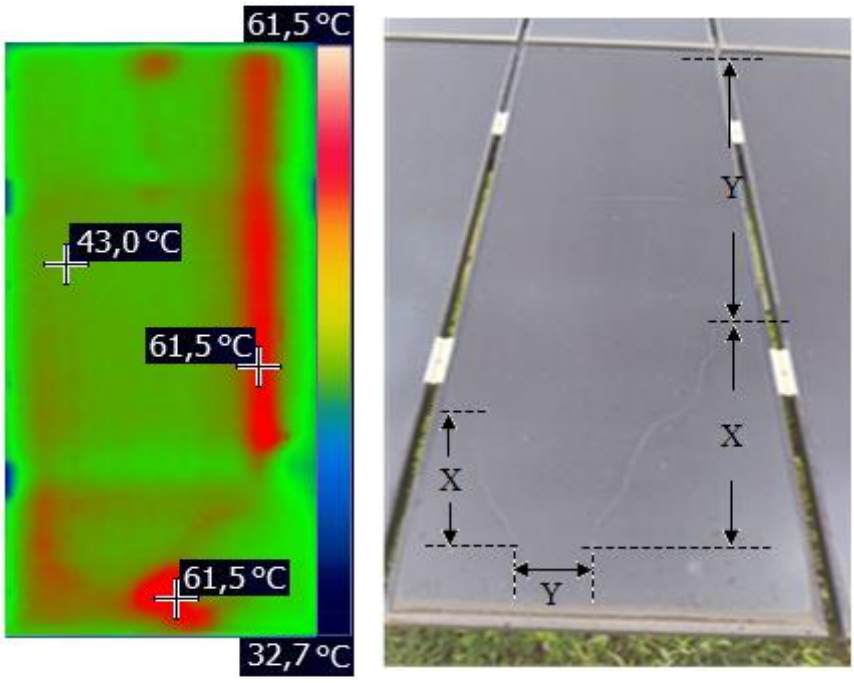

Figure 4-3: Thermal and optical images of module, M03, in a CIGS module string, A200-Inv11-ST08.

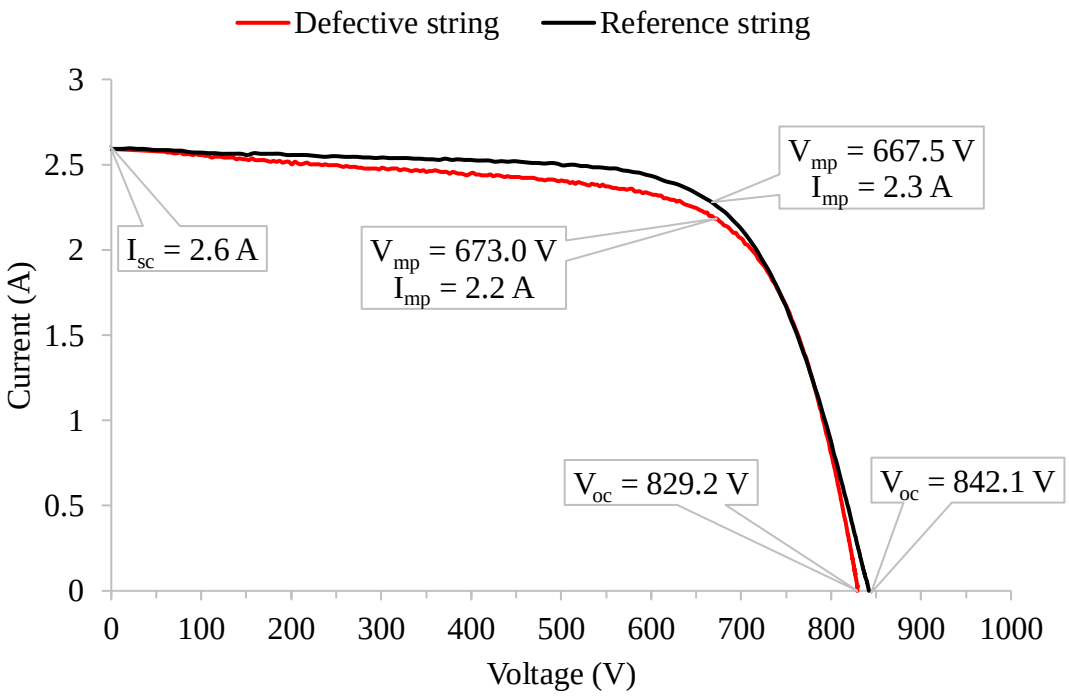

Figure 4-4: I-V curve of the defective string A200-Inv11-ST08, being compared to a reference string of CIGS modules.

Table 4-3 indicates the effect of the irreversible damage on module string performance. It shows a drop in FF, and a significant power loss of 54 W, which translates to a 3.5% underperformance of the string.

Table 4-3: Performance parameters of the defective and reference CIGS strings.

String	I_{sc} (A)	V_{oc} (V)	I_{mp} (A)	V_{mp} (V)	FF	P_{max} (W)
A200-Inv11-ST08 Defective	2.6±1.2%	829.2±1.0%	2.2±1.4%	673.0±1.1%	0.69	1481±3.7%
A200-Inv11-ST09 Reference	2.6±1.2%	842.1±1.0%	2.3±1.4%	667.5±1.1%	0.70	1535±3.7%
ΔP (%)	0.0±1.2	1.5±1.0	0.4±1.4	0.8±1.1	0.01	3.5±3.7

The cracks in the module forced parts of the monolithic cells to separate resulting in current mismatch between the series connected cells. Abnormal heating of sections of cells labelled Y caused the operating voltage of the affected cells to move towards reverse bias resulting in an

increased loss of power produced by the module. Some affected cells may be even forced into severe reverse breakdown voltage, thus reducing the module and string current in the operating region below 600 V. Interruption of cells and interconnects due to the cracks caused some parts of the cells not to contribute power resulting in the drop in V_{oc} of the string. If the module in the string is not replaced, the persistent hot spotting continues to impact on the functionality and energy yield of the PV system. Additionally, interruption of other normal operating cells is possible since the cracks may extend by the hot-spotting and influence of the environmental conditions. Moisture infiltration through the cracked parts, may lead to other abnormalities like delamination of the encapsulant [16], as seen in the defective module M09 of string A700-Inv17-ST09. Plants located in industrial area, like ERIC facility, are exposed to industrial gases. If the waste gases react with moisture, acid is formed and when it penetrates through the glass cracks it causes corrosion of the cell fingers, busbars and interconnects. All these secondary abnormalities, as highlighted in section 2.5.1, result in further deterioration of the module string power and increases the degradation rate of the cracked module.

String A700-Inv17-ST09 consisting of CIGS modules had one defective module, M10, that was observed in thermal imaging. The thermal image of the defective module in the string is shown in Figure 4-5 (a) and it indicates a hot area across several cells. The affected area shows a temperature increase of 5.4°C from normally operating cells. The optical image in Figure 4-5 (b) shows a strip of discolouration, possibly due to delamination on the sun facing side of the module, which correspond to the hot areas on the cells. It was also noted, after visual inspection, that the module's back side had cracked. The portion which aligns to the cracked part is indicated in Figure 4-5 (c) and matches to the delaminated section and the hot area.

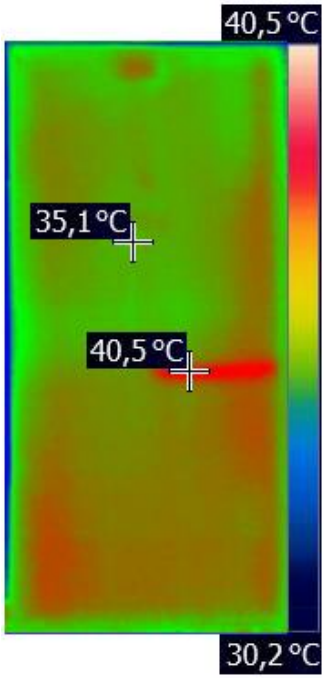

Front surface

Crack visible from back surface is highlighted

a **b** **c**

Figure 4-5: Thermal and optical images of the defective module in string A700-Inv17-ST09.

The optimum power generation of the string was affected by the damage in the module and the impact on the string performance is seen in Figure 4-6, comparing the defective and reference strings I-V characteristics. The I-V curve of the defective string is sloped for voltages between 600 V and V_{oc}, showing an increase in series resistance of the electrical current path of the string. This is due to the crack which interrupted the cells and interconnections and causing the string to underperform as indicated by the drop in the defective string's FF and power loss of around 129 W (8.4%). The performance parameters are listed in Table 4-4.

The impact of current mismatch on performance of solar cells is discussed in section 2.5. The crack may have resulted from mishandling of the module during installation or maintenance. It can also be speculated that the mismatch may have been caused by non-uniformity in the scribing process during manufacturing. Another cause could be long-time uneven shading on the affected cells may have the affected part of the cells to operate in reverse bias and overheat. The abnormal heating may have caused the cracking of the cell material since the CIGS modules have no bypass diodes to circumvent the hot-spotting effect. Further delamination of the encapsulant may have resulted due to moisture ingress through the crack [17].

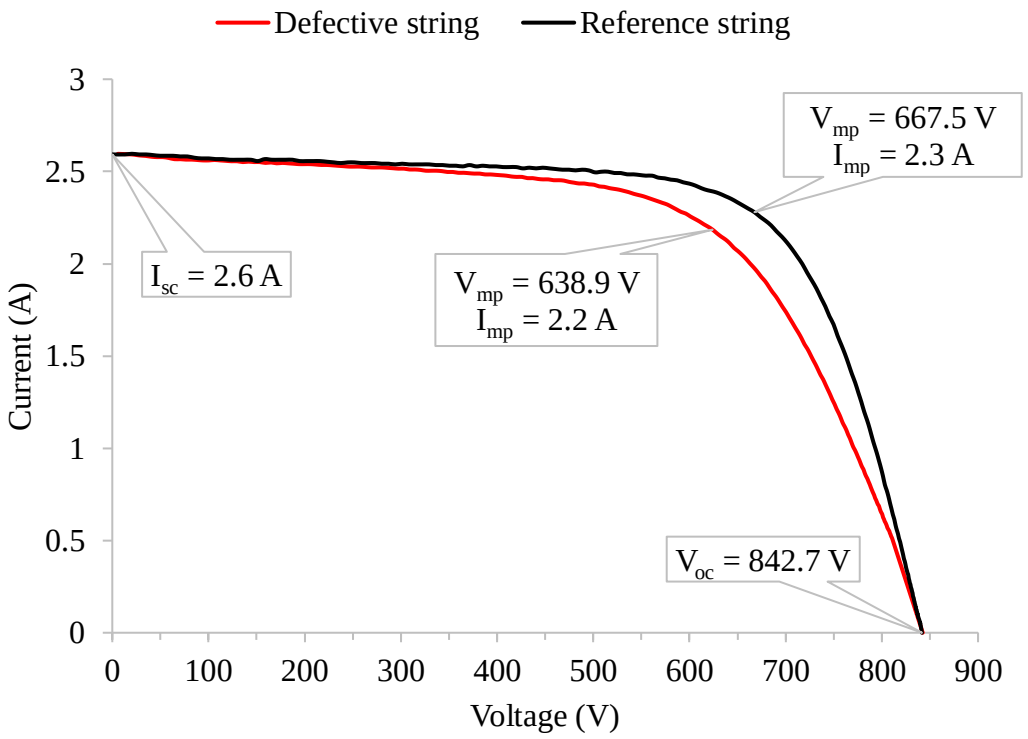

Figure 4-6: The I-V characteristics of the defective string, A700-Inv17-ST09, and the reference string.

Table 4-4: Performance parameters of the defective string, A700-Inv17-ST09, and the reference string of CIGS modules.

String	I_{sc} (A)	V_{oc} (V)	I_{mp} (A)	V_{mp} (V)	FF	P_{max} (W)
A700-Inv17-ST09 Defective	2.6±1.2%	842.7±0.8%	2.2±1.4%	638.9±0.9%	0.64	1406±4.2%
A700-Inv17-ST06 Reference	2.6±1.2%	842.7±0.8%	2.3±1.4%	667.5±0.9%	0.70	1535±4.2%
ΔP (%)	0.0±1.2	0.0±0.8	4.3±1.4	4.3±0.9	0.06	8.4±4.2

4.3 Effect of Shading on string performance

4.3.1 Effect of soiling on performance of mc-Si PV module string

Figure 4-7 shows a thermal image of a mc-Si module, M05, with a hot cell which was identified, during aerial thermography, in string A600-Inv16-ST04. This is the only module in this string that was observed to have thermal irregularities. The cell has a temperature 11.1^{o}C higher than the neighbouring cells. The visual image (Figure 4-7) of the module shows an optical impediment (bird dropping) which corresponds to the hot cell and is visible on the front surface of the module.

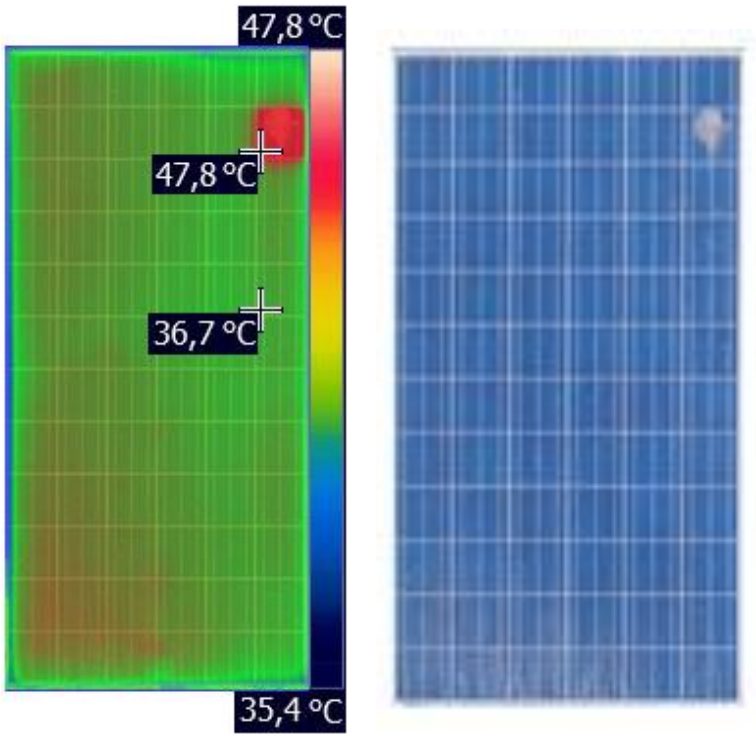

Figure 4-7: Thermal and optical images of a module soiled from bird dropping.

Figure 4-8 shows the I-V curve of the defective string (A600-Inv16-ST04) compared with a reference string (A600-Inv16-ST03). The shading of one cell in a mc-Si module string results in a step in the I-V curve caused by current conduction of a bypass diode in parallel to the affected substring. The negative impact on performance of the string due to this partially soiled cell was minimised by the 'protection' measure of the bypass diode which was forced into forward bias by the mismatch effect, as illustrated in section 2.5.1.

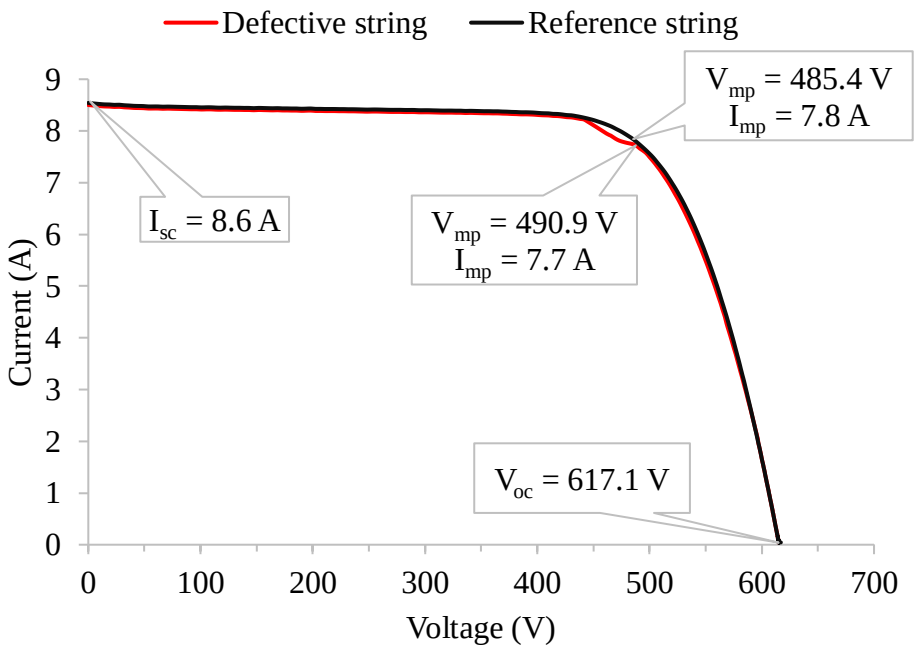

Figure 4-8: I-V curves of the defective and reference strings unmatched due to bird dropping.

The result is a power loss of approximately 6 W and reduction in the string performance (0.16%) and FF. The parameters indicating the defective and reference strings' efficiency are listed in Table 4-5. Considering that each 72-cell module produced approximately 270 W and that each cell only produced on average 3.7 W, the 6 W power loss from the partial shading of one cell can be considered disproportionate. This result highlights the fact that whole module substrings are affected by one mismatched cell and that without bypass diode protection, the power loss and hot spot damage may be more severe.

Table 4-5: Performance parameters of an underperforming string (defective), due to bird dropping, and a reference string.

String	I_{sc} (A)	V_{oc} (V)	I_{mp} (A)	V_{mp} (V)	FF	P_{max} (W)
A600-Inv16-ST04 Defective	8.6±1.9%	617.1±0.9%	7.7±2.8%	490.9±0.9%	0.712	3780±3.2%
A600-Inv16-ST03 Reference	8.6±1.9%	617.1±0.9%	7.8±2.8%	485.4±0.9%	0.713	3786±3.2%
ΔP (%)	0.0±1.9	0.0±0.9	1.3±2.8	1.1±0.9	0.001	0.2±3.2

The module string power loss is statistically insignificant especially when considering the calculated percentage uncertainty of ±3.2% given in Table 4-5. However, it proves the effectiveness of the bypass diode. The activated bypass diode minimises the detrimental effect of hot spotting on the entire string and reduces module string power loss. The solar cell under partial shading heats up, since it is producing less current than the rest of the cells in the substring and is forced into reverse bias, resulting in consumption of the substring's generated electrical energy as heat. In addition, some of the solar radiation received by the soiled cell is not converted to electrical power so, since energy must be conserved, it is only wasted as heat. This will cause the cell temperature be extraordinarily high [58], and damage the cell if the condition stays for long. Secondary effects such as delamination, module glass cracks and burns can occur and the damage will remain even after the module has been cleaned.

A non-homogeneous temperature distribution was identified in one module A300-Inv20-ST04-M13 on thermography images and is shown in Figure 4-9. One cell is abnormally hot and has a temperature difference of 8.4^{o}C with the reference temperature of 40.3^{o}C. The module's optical image in Figure 4-9 indicates that there is build-up of soil along the bottom module frame, which resulted in uneven shading along all the cells on the bottom row. The partially shaded cells are numbered 12, 13, 26, 27, 60 and 61, with cell 61 mostly affected as it is much hotter (58.7^{o}C) than the other cells and has more sediments on it. Five cells 12, 13, 26, 27 and 60 seem to be partially hot and the substring on the right side also seem to be warm.

The output electrical characteristics of the module string (A300-Inv20-ST04) is shown by the I-V curve in Figure 4-10, which deviates from the reference I-V curve (A300-Inv20-ST03) with two clear bumps at about 500 V and 540 V. The bumps are due to the activation of bypass diodes due to uneven shading in substrings. The individual I-V curve of the affected module was not measured but based on the position and shape of the bumps in the I-V curve, valuable inferences can be made. Table 4-6 shows that the string with the soiled module is underperforming and this is revealed by a small drop in FF and a reduction of 7 W in the optimum generated power, thus a 0.18% decrease in performance.

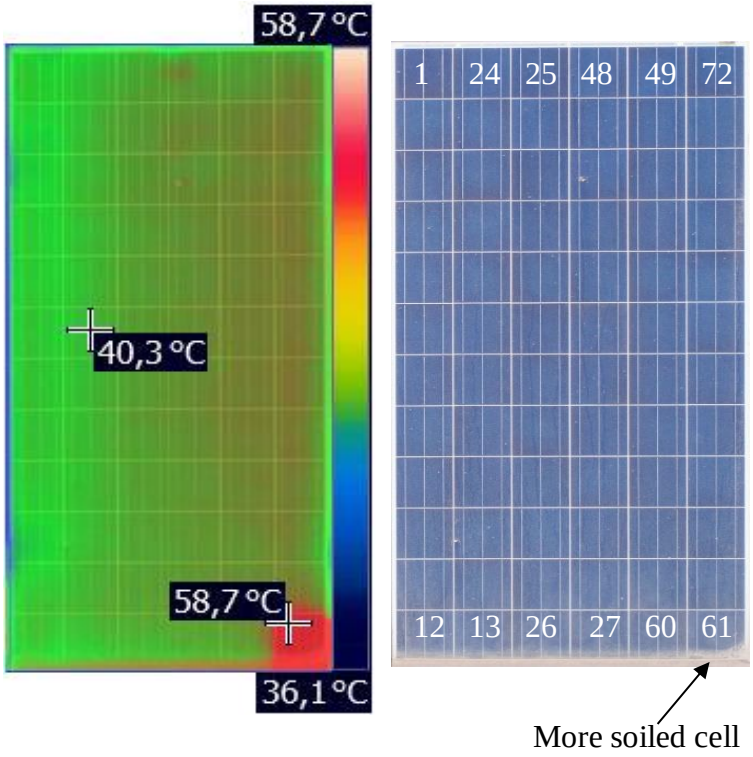

Figure 4-9: Thermal and optical images of the partially soiled module in string, A300-Inv20-ST04.

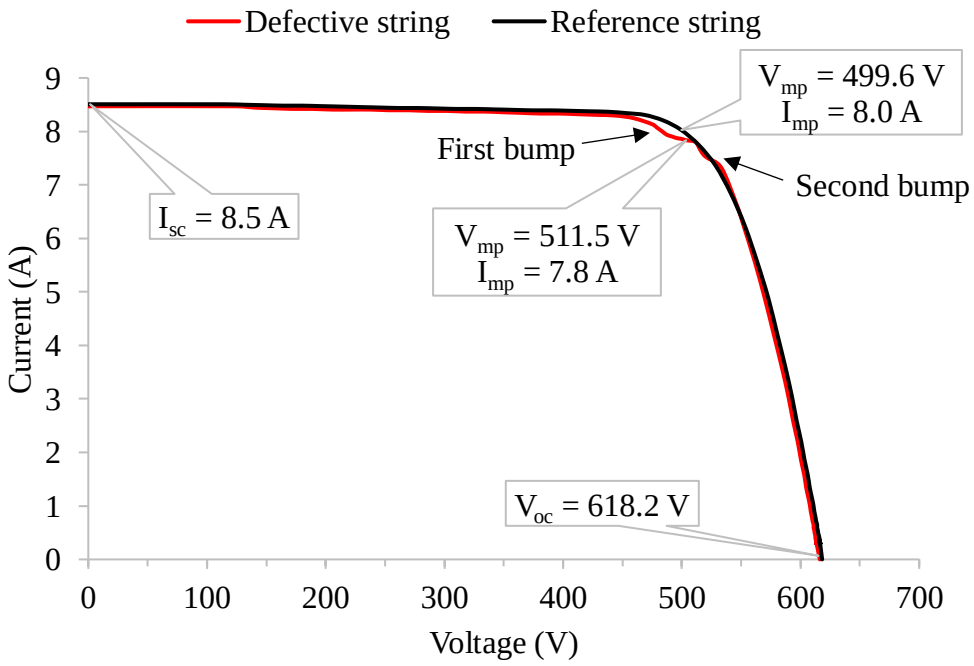

Figure 4-10: I-V curves of the defective and reference strings not matching due to partial soiling.

Table 4-6: Performance parameters of a defective string, A300-Inv20-ST04, and reference string, A300-Inv20-ST03.

String	I_{sc} (A)	V_{oc} (V)	I_{mp} (A)	V_{mp} (V)	FF	P_{max} (W)
A300-Inv20-ST04 Defective	8.5±1.9%	618.2±0.9%	7.8±2.8%	511.5±0.9%	0.759	3990±3.2%
A300-Inv20-ST03 Reference	8.5±1.9%	618.2±0.9%	8.0±2.8%	499.6±0.9%	0.761	3997±3.2%
ΔP (%)	0.0±1.9	0.0±0.9	2.5±2.8	2.4±0.9	0.002	0.18±3.2

Current mismatch due to uneven shading and the effect of bypass diodes on power loss is discussed in section 2.5.1. The drop in voltages at the bumps points to the possibility that two substrings are affected at first bump (approximately 30 V) and one substring is affected at second bump (approximately 15 V). The drop in current at each bump reveals that the affected substrings had different levels of shading, one lightly shaded (first bump) and one more heavily shaded (second bump). The two lightly shaded substrings (first bump) and the single more heavily shaded substring (bump two) can be observed in the thermal image Figure 4-9. The soiled module is generating less current than the expected (8.5 A) because of shading on the bottom cells 12, 13, 26, 27, 60 and 61. Partial shading seems to be uniform across the bottom five cells 12, 13, 26, 27 and 60 of two substrings. The substring with cell 61 (second bump) is generating less than the other two substrings (first bump) because of more soil on the cell. This shading scenario was simulated on poly-crystalline modules at ORF and using a PVSim program and the shapes of the I-V curves observed are similar to the I-V curve of the defective string in Figure 4-10. More information relating to this irregularity is discussed in sections 4.6 and 4.7.

Although the impact of dust and bird droppings on PV module efficiency can be minimal, as indicated in Table 4-5 and Table 4-6, it can lead to overheating and damage of the conducting bypass diode due to continual conduction of huge amount of current generated by the module string that is if the modules are not routinely cleaned. The dissipated thermal energy, from the abnormally heated bypass diode, can be revealed by a hot junction box on thermography inspection.

4.3.2 Impact of shade on performance of CIGS modules

Two modules with thermal inhomogeneity were observed in string, A200-Inv11-ST07. Thermal images of the only defective modules, M01 and M09, in the string are shown in Figure 4-11 (a) and (c) respectively. The thermal image of module M01 shows middle cells at elevated temperature of 44.8°C and are 5.3°C higher than the normally operating cells in the module. It can be seen from the optical image, in Figure 4-11 (b), that the overheated cells correspond to the partially shaded cells due to non-uniform vertical dirt streak on the front surface of the module, M01. The thermal image also shows that the neighbouring cells to the shaded cells are warm.

Thermal image of module M09, shown in Figure 4-11 (c), indicates two hot spots. One is due to a hot junction box and is only 3.7°C above the reference temperature of 39.8°C and the other hot spot is at 43.0°C, thus 3.2°C higher than the temperature of the normal operating cells. No optical impediment or any visual abnormality was observed on the front and back surfaces of this module. An optical image of the module is shown in Figure 4-11 (d).

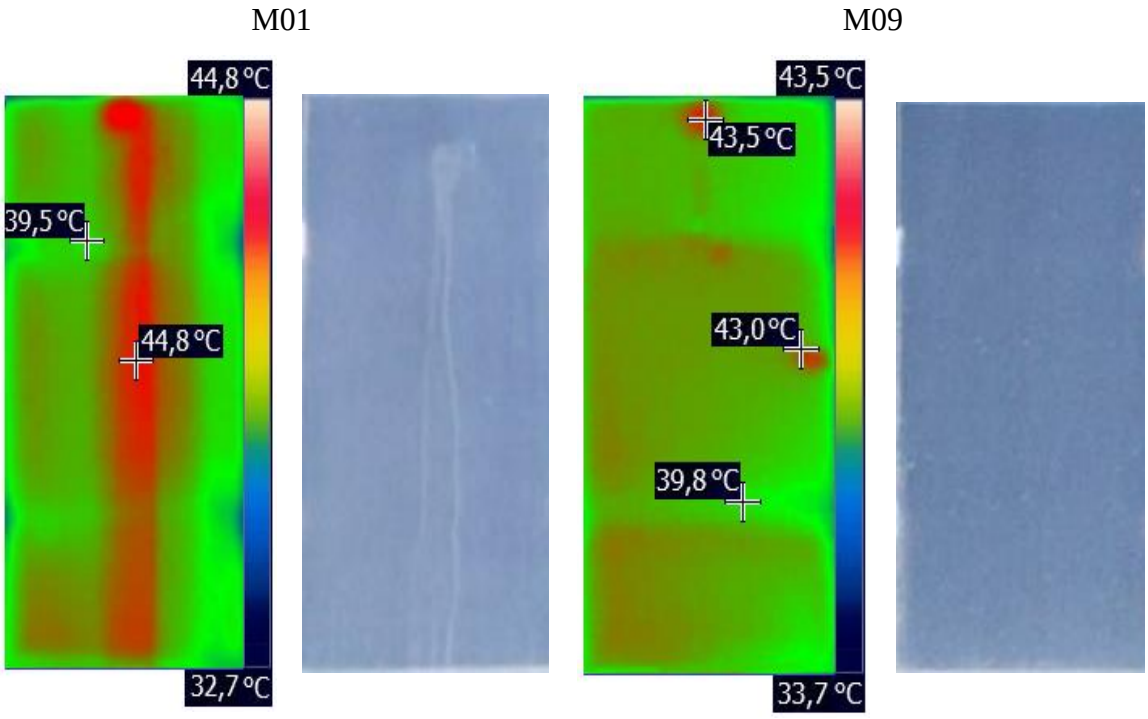

Figure 4-11: Thermal and optical images of modules with thermal irregularities in string A200-Inv11-ST07.

The performance of the affected string is shown by the defective string's I-V curve in Figure 4-12 as compared to the non-defective reference string, A200-Inv11-ST09. Two features in the string's I-V curve stand out; a bump near I_{sc} on the defective string's I-V curve and a reduction in Voc. This resulted in a drop in the defective string's FF and output power reduction of 25 W from the expected, 1535 W and is calculated in Table 4-7.

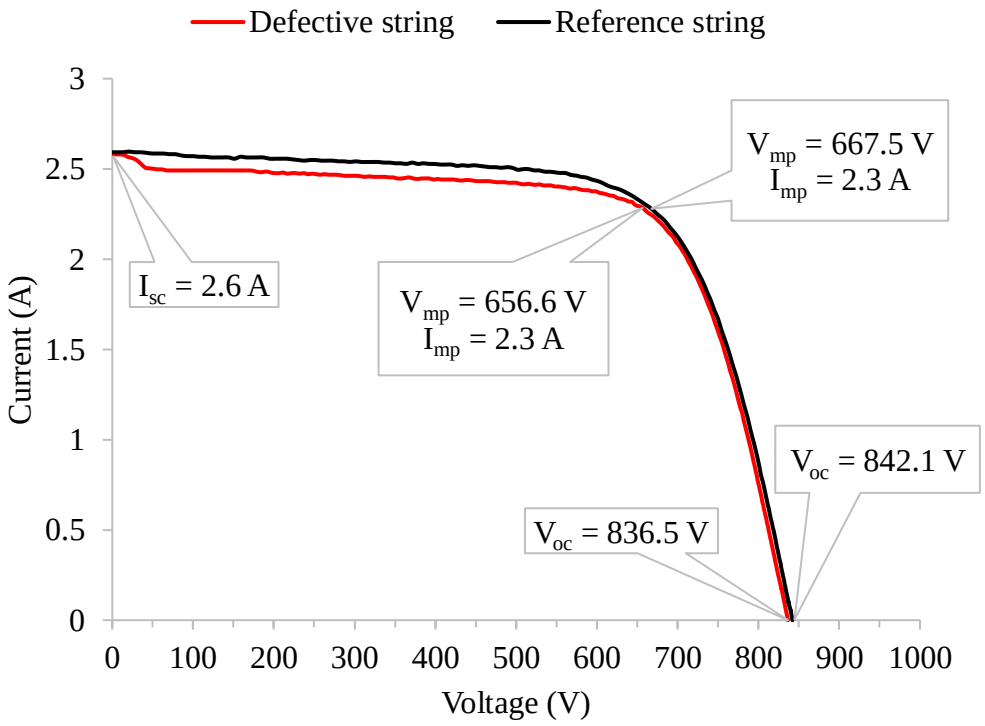

Figure 4-12: I-V curves of defective and reference strings in area A200. The defective string has two modules with thermal inhomogeneity.

Table 4-7: Performance parameters of the defective and reference stings.

String	I_{sc} (A)	V_{oc} (V)	I_{mp} (A)	V_{mp} (V)	FF	P_{max} (W)
A200-Inv11-ST07 Defective	2.6±1.2%	836.5±0.9%	2.3±1.4%	656.6±1.1%	0.69	1510±3.7%
A200-Inv11-ST09 Reference	2.6±1.2%	842.1±0.9%	2.3±1.4%	667.5±1.1%	0.70	1535±3.7%
ΔP (%)	0.0±1.2	0.7±0.9	0.0±1.4	1.6±1.1	0.01	1.6±3.7

In the absence of bypass diodes, the current mismatch caused by the uneven soiling in module M01 resulted in one or two cells to be reverse biased. The small bump close to I_{sc} points to the severity of the reverse bias, close to 800 V. At these voltages, cells would experience a rapid reverse bias breakdown current as indicated by the current bump close to I_{sc}. This effect caused a significant impact on the string performance and may have resulted in shunt paths and permanent damage of the affected module. This detrimental effect on partially shaded thin-film PV modules is also discussed in [17][59], and is owing to the reverse biasing of non-uniformly shaded solar cells and the absence of bypass diodes in the modules of CIGS technology. The reverse biasing and use of bypass diodes to avoid such damage is illustrated in section 2.5.1. The hot spotting effect is degenerative as it affects other cells surrounding the overheated cells. This transfer of heat to the other cells in the vicinity, reduce the performance of the good operating cells and can further affect generated output power of the string.

It is speculated that the failure in module M09 is due to the "worm" delamination defect [25], in its infant stage. Its effect on the string's generated electrical energy is marginal since the temperature difference, of 3.2°C, between the hot spot and the module's background reference temperature is small. Figure 4-13 shows the worm defect which is prevalent in several thin-film modules in the plant but was not observed in the defective string, A200-Inv11-ST07.

Figure 4-13: Typical "worm" defect found in CIGS modules.

4.4 Impact of a burnt cell on performance of mc-Si string

Hot spots were identified in string A100-Inv06-ST01 on one defective module, M01. The thermal image, of the defective module, in Figure 4-14 (a), shows two hot spots, one due to a warm junction box and another one caused by a damaged cell. The temperature scale indicates that the hotspot is at an abnormal temperature of 49.6°C thus a temperature difference of 5.5°C above the reference temperature of 43.8°C. The junction box is only 2.6°C above the reference temperature of normal operating cells. There is no optical impediment on the front surface of the module, see Figure 4-14 (b), however the hot spotting produced enough heat to cause visible damage, burn marks, at the backside of the module. This feature as seen from the backside is shown in Figure 4-14 (c) and corresponds to the hot spot on the affected cell, number 42.

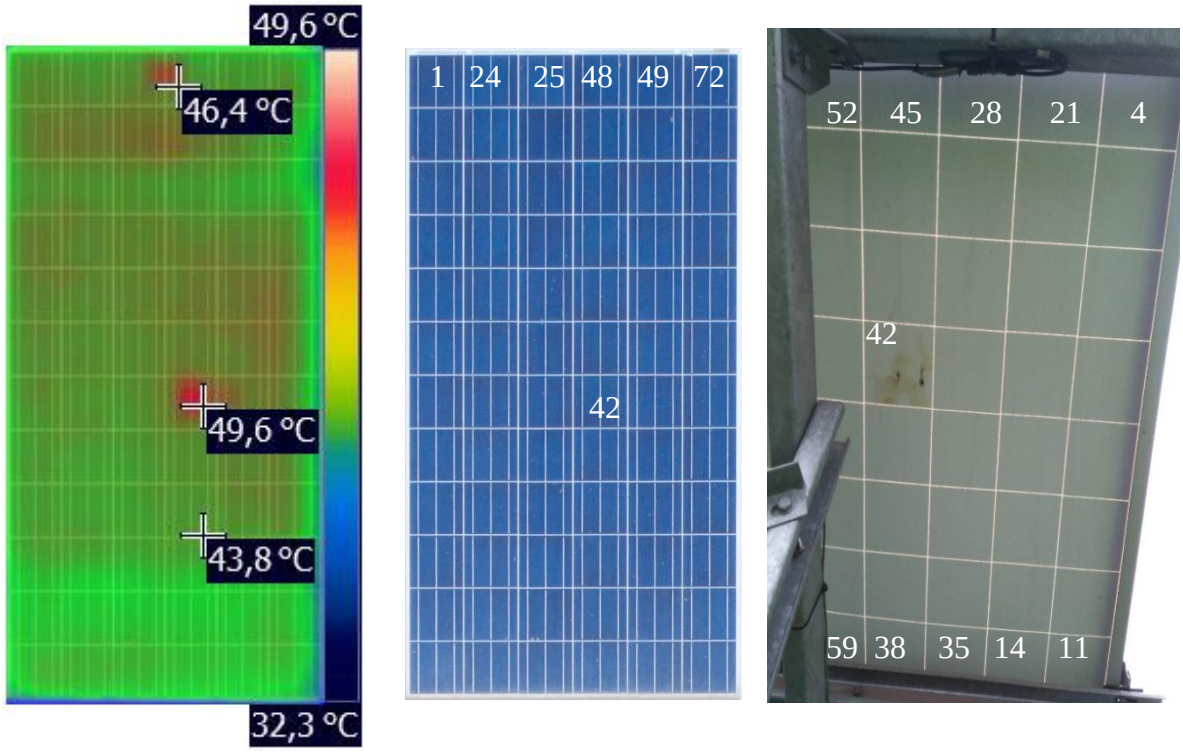

a **b** **c**

Figure 4-14: Thermal and optical images of a module with a burnt cell in mc-Si string, A100-Inv06-ST01.

The burn marks were probably caused by localised heating due to resistive flow of current on faulty soldered joints. The thermal fatigue may have increased the resistance until the cell was hot enough to burn and discolour the back encapsulation. This high series resistance is revealed by the slope of the defective string's I-V curve near V_{oc}, in Figure 4-15. In comparison to the

reference string, A100-Inv06-ST03, the failure of the cell caused the defective string to underperform by 2.1% equivalent to 84 W power loss, as calculated in Table 4-8. The small reduction in performance of the defective string, due to the burnt cell agrees with the findings published in the report; Review of Failures of Photovoltaic Modules [17]. The V_{oc} is insignificantly reduced since the damage has only destroyed small parts of the cell.

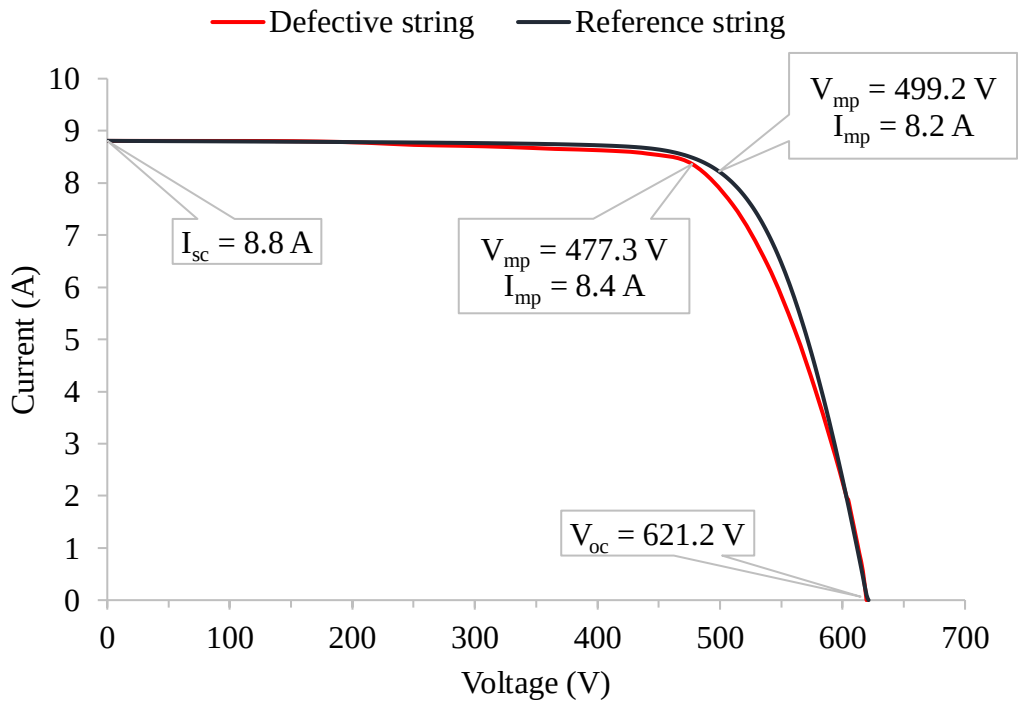

Figure 4-15: Defective I-V curve of a string with a burnt cell and a reference string I-V curve.

Table 4-8: The parameters showing performance of the defective and reference strings.

String	I_{sc} (A)	V_{oc} (V)	I_{mp} (A)	V_{mp} (V)	FF	P_{max} (W)
A100-Inv06-ST01 Defective	8.8±1.9%	621.2±0.9%	8.4±2.8%	477.3±1.0%	0.73	4009±3.4%
A100-Inv06-ST03 Reference	8.8±1.9%	621.2±0.9%	8.2±2.8%	499.2±1.0%	0.75	4093±3.4%
ΔP (%)	0.0±1.9	0.0±0.9	2.4±2.8	4.4±1.0	0.02	2.1±3.4

The I-V curve of the defective string shows no bump, so no bypass diode is conducting. Therefore, no current mismatch between substrings occurs confirming the observation that only a small part of the affected cell is damaged. The higher resistance of the busbars of the defective cell contribute to the increase in the series resistance slope of the string's I-V curve. From safety point of view, an electric arc may result which can cause fire, especially if the module string has many series connected modules, a scenario which creates very high voltage. Accordingly such a failure on a cell level which cascade the impact to the overall module string power can lead to serious repercussions due to the fire risk or possible electrical shocks [60][17].

4.5 Thermal signatures on non-visual abnormalities

The thermal image in Figure 4-16 shows a "defective" cell at a temperature slightly higher (ΔT = 2.1°C) than the reference temperature, 32.8°C, of normal operating cells. No optical impediment was seen on the surfaces of the PV module, and it is the only module (M11) with thermal irregularity that was observed in the module string, A100-Inv04-ST03. The optical image is shown in Figure 4-16. The performance of the string was not affected by the warm cell. This is reflected by the I-V curve of the "defective" string, in Figure 4-17 which matches to the I-V curve of the reference string, A100-Inv04-ST04.

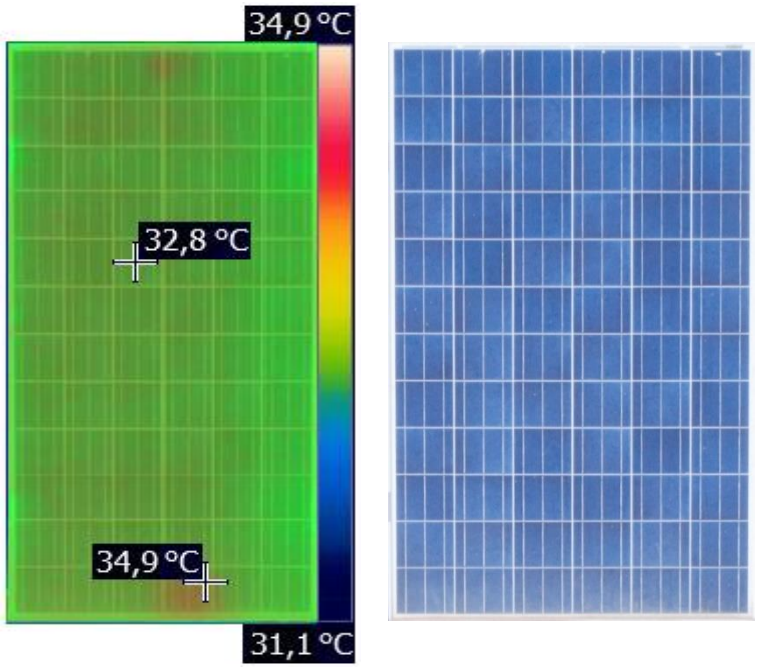

Figure 4-16: Thermal and optical images of a module with a warm cell.

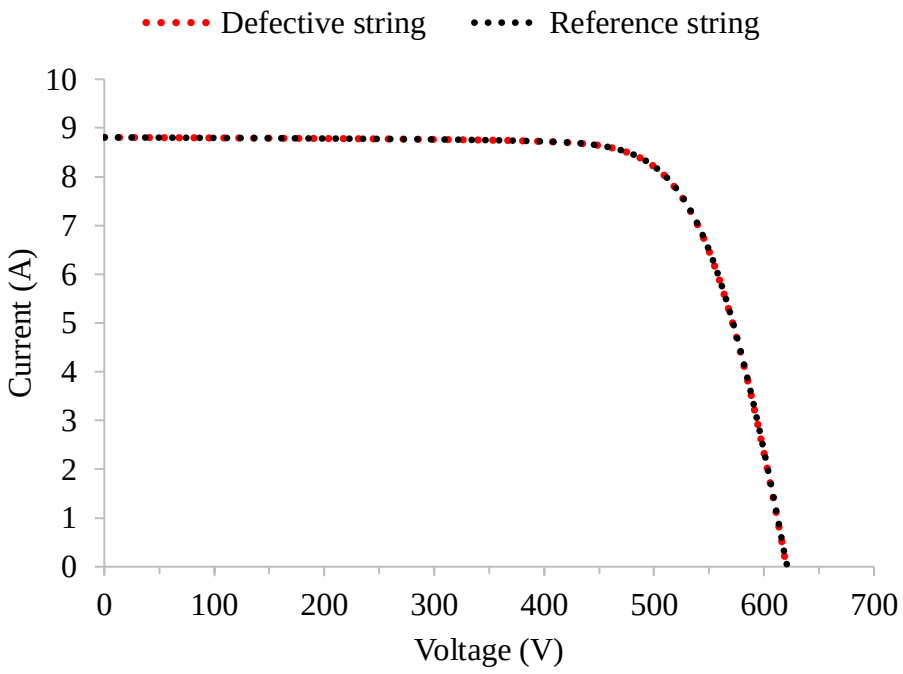

Figure 4-17: Matching I-V curves of a defective and reference strings. The defective string contains a module with a warm cell.

The marginal temperature difference, 2.1°C, indicates that the abnormality of the cell has no measurable impact on the performance of the string since defects which mostly reduce the efficiency of PV modules have to be at an abnormally high temperature and should have a standardised minimum temperature difference of 5°C from the reference temperature of normal operating cells in the same module. The thermal anomaly was probably due to non-visible cell defect, such as micro-cracks, creating small current mismatch in the module substring current and in turn warming up the cell. It is usually difficult or impossible to detect such types of failures under low solar irradiance conditions with low/no current mismatch to cause notable thermal signatures. Micro-cracks can develop into larger and deeper cracks over time due to thermal and mechanical stresses which can cause complete isolation and inactive of some cell parts leading to a significant power loss [17]. A clear picture of what is causing the slight increase in temperature of the 'defective' cell can be observed by using other inspection techniques such as Electroluminescence (EL) and Ultra violet (UV) fluorescence imaging. These non-destructive testing methods can detect micro-cracks, broken fingers and resistive parts, in a solar cell, which are not visible by naked eyes [17]. The dynamics of thermal signatures also depend on the operating point of a solar cell on the I-V curve, as highlighted in chapter 2. Since the operating point of the affected cell may change, the thermal signature may also change throughout the day as the environmental conditions change.

4.6 Performance of a mc-Si string after soiling simulation at ORF

The soiling scenarios in section 4.3.1 were simulated on a string of mc-Si modules at the Outdoor Research Facility (ORF) and the thermal images and power measurements were recorded in order to provide a verification of the observations made at ERIC.

Figure 4-18 and Figure 4-19 show thermal and optical images of a module with a shaded cell. Flour was used to resemble soiling, which caused various mismatch scenarios with resulting hot-spotting on the thermal images.

The optical impediment caused a bump (activated bypass diode) on the I-V curve shown in Figure 4-20. The shapes of the I-V curves in Figure 4-20 and Figure 4-8 are similar and reflecting the effect of shading one cell on a module string. When more flour was added to the same area the cell was under heavy shading thus receiving less light. This localised hot spotting on a cell string is detrimental as it increased the cell temperature shown in Figure 4-19 and reduce string power output. It forced the affected substring to contribute less current because of the increased current mismatch and is reflected by the defective module string's I-V curve of heavy shading in Figure 4-20. The change in the substring's short circuit current, ΔI, due to the change in shading is indicated in Figure 4-20. I_{sc} and V_{oc} of the shaded and unshaded reference strings is equal since only small area is shaded.

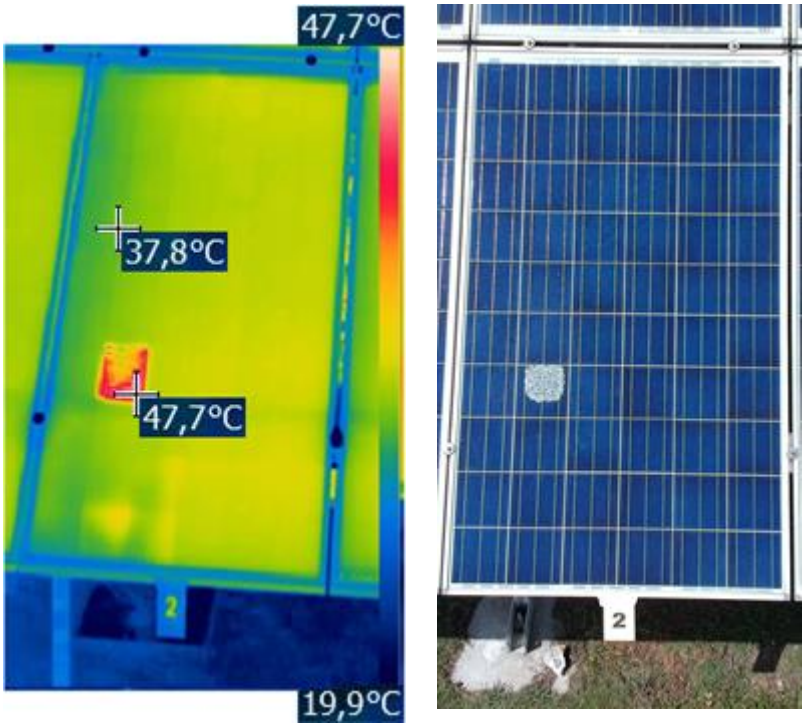

light shading

Figure 4-18: Thermal and optical images of a module with a cell under light shading.

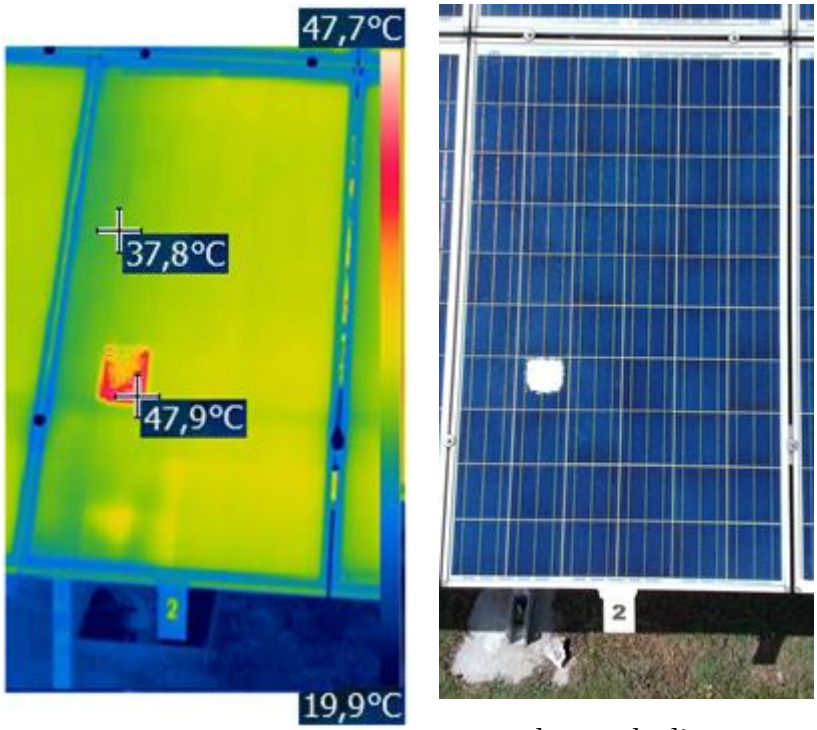

heavy shading

Figure 4-19: Thermal and optical images of a module with a cell under heavy shading.

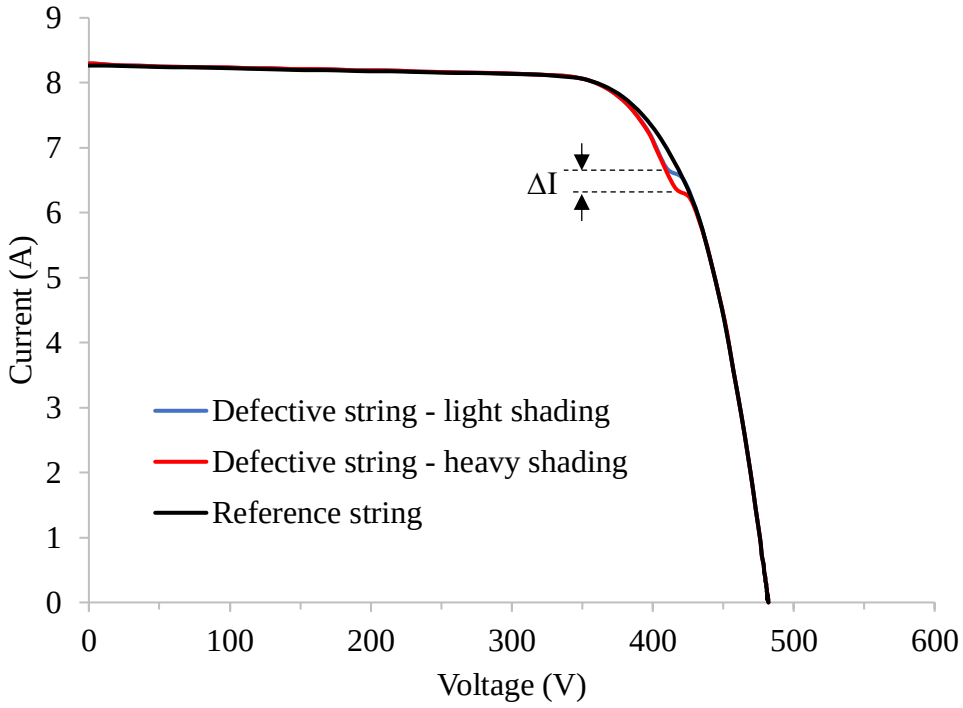

Figure 4-20: I-V curves of defective and reference strings.

Figure 4-21 shows thermal and optical images captured after partial shading on cells at the bottom row of module numbered 3. The images clearly indicate that the hot cell is due to uneven shading in a substring. The effect, on performance, is revealed by the I-V curve of the defective string in Figure 4-22 and its shape is similar to the defective string's I-V curve in Figure 4-10. The non-uniform shading, as discussed in section 4.3.1 caused current mismatch which led to two bumps. The voltages, V_1 and V_2, approximate the substring voltages of the shaded module. V_1 equals to voltage of the most affected substring, with a hot cell, and V_2 gives the voltage of the other two substrings in the soiled module. It can be seen, in Figure 4-22, that,

$$V_2 \sim 2(V_1) \qquad 4.1$$

and the module's voltage V_m can be estimated using equation 4.2.

$$V_m = V_1 + V_2 \qquad 4.2$$

The I-V curve of the shaded module also indicates that as the number of the activated bypass diodes increases the bump shifts to the left. This is reflected by the first bump which is more to the left and showing two bypass diodes that are conducting.

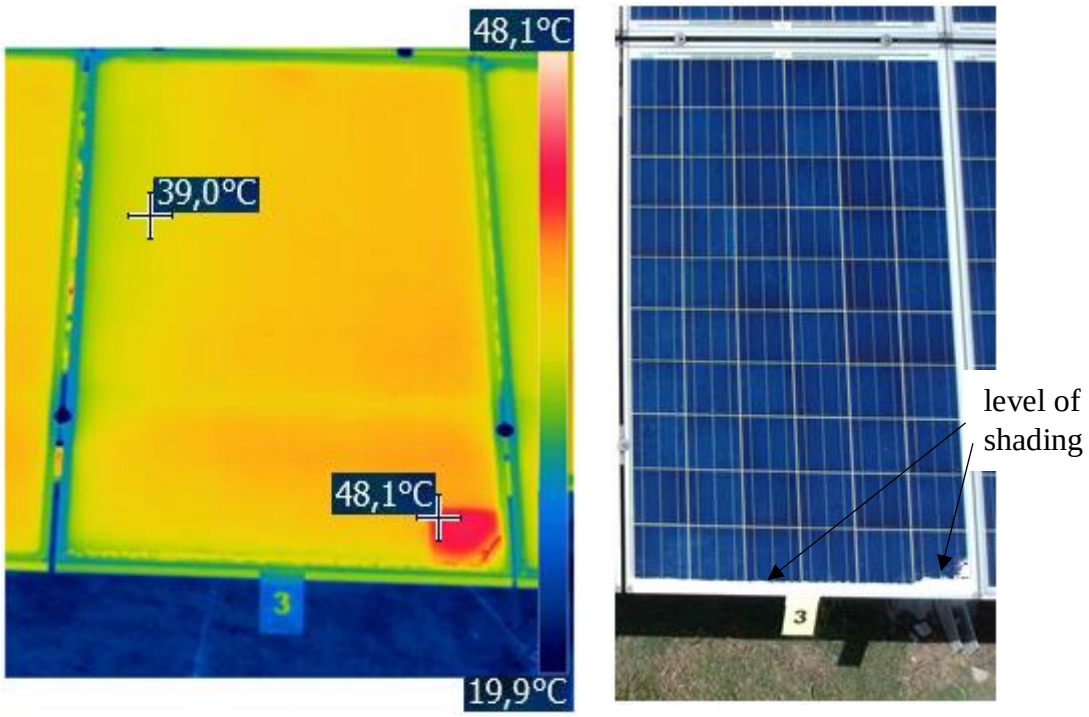

Figure 4-21: Thermal and optical images of a module with bottom row of cells partially shaded.

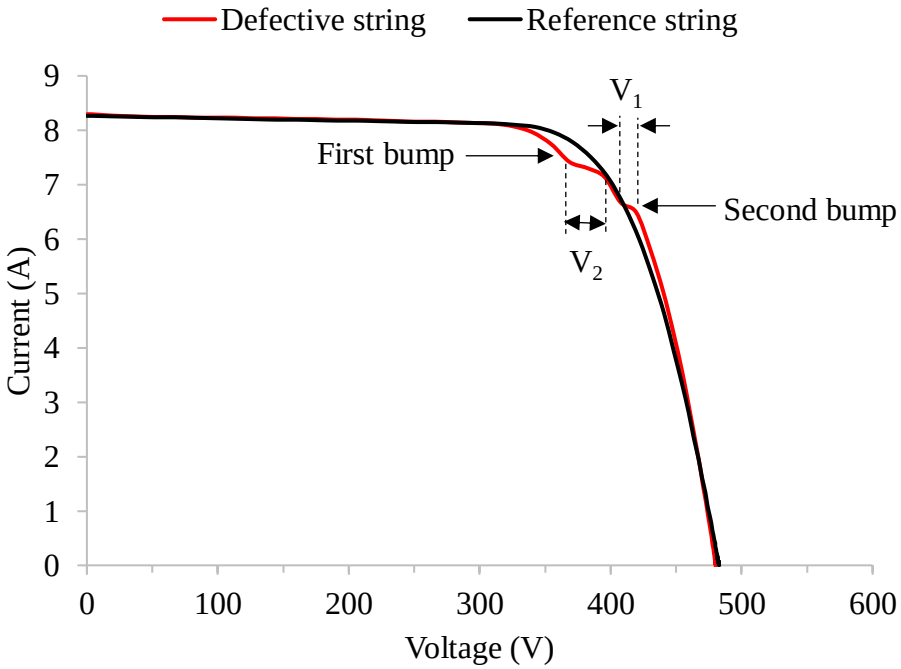

Figure 4-22: I-V characteristics of a defective and reference strings. The defective string contains a module with bottom row of cells partially shaded.

There are two variables and four possibilities when cells are under soiling. The two variables are 1) heavy (S) or light soiling (s) and 2) number of affected cells/substrings [many (N) and few (n)] which lead to having four possible combinations, SN, Sn, sN and sn. Each of these combinations will have a different effect on the I-V curve. Light shading gives shallow bumps (kinks) in the I-V curve while heavy soiling result in deep bumps and cause a large change in current. If more cells are affected the bump in the I-V curve will show a big drop in voltage and the bump appears more towards the lower voltage, however, if a few cells/substrings are affected, the bump will be closer to V_{oc} along the I-V curve.

4.7 Simulation of soiling scenario using PVSim program

The shading scenario on string A300-Inv20-ST04 was modelled in PVSim [30] and the I-V characteristics obtained are shown in Figure 4-23. A string of 14 modules was assumed to contain one underperforming module M01. The substrings of M01 were assumed to be generating less current than the string current. Two substrings of the module, M01, were assumed each to produce 7.5 A and the third substring produce 7.0 A. The string current was assumed to be 8.2 A and this scenario generated I-V parameters shown by the I-V curve of Simulation 1 in Figure 4-23. It can be seen that the shape of the I-V curve of simulation 1 is similar to the I-V curve of the defective string A300-Inv20-ST04, in Figure 4-10. Simulation 2 shows an I-V curve when current mismatch increases, with the two substrings assumed to be producing 6.0 A and the third substring producing 4.5 A. If the current mismatch increases probably due to more shaded cell parts, the bypass diodes of the affected module conduct at lower current. This is shown by the bumps of the I-V curve of simulation 2 and results in decrease in area under the I-V curve implying that the power generated also drops with more shading. An increase in current mismatch also causes the affected cells to be at abnormally high temperature than when current mismatch is low and affects the operating point, P_{max} point, of the string. The effect on the string's operating point due to change in mismatch is indicated by P_{max} points (P_{max1} and P_{max2}) of the simulated I-V curves in Figure 4-23. The P_{max} point of the string shifts to the left (P_{max2}) towards I_{sc} when mismatch is high and moves to the right (P_{max1}) towards V_{oc} when current mismatch is low. This also applies to substrings and cells operating in series. Uneven cell illumination and non-uniform cell degradation cause series connected substring mismatch which results in change in shape of I-V curves of module strings, as explained in reference [44]. This work describes how reverse breakdown occurs in solar cells and that when a cell operates in reverse bias it causes a reduction in voltage and power generated by a substring and module string.

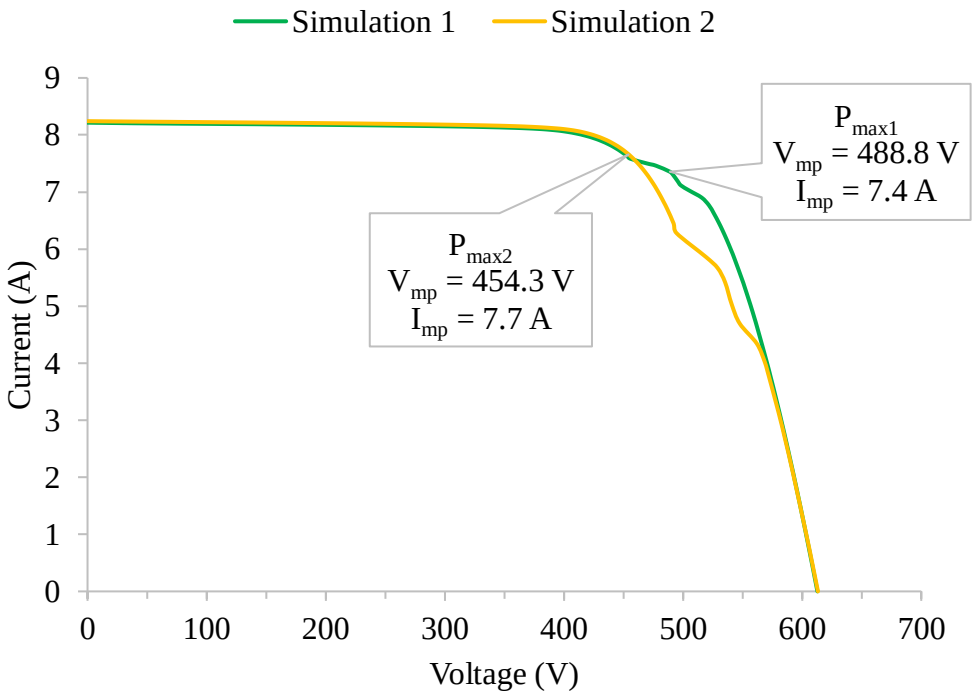

Figure 4-23: Simulated I-V curves of a string A300-Inv20-ST04, at different current mismatch.

4.8 Summary

Different thermal anomalies, due to several irregularities in PV module operation were analysed and their impact on module string output power was discussed. Significant reduction in string power was noticed on modules with thermal signatures of cracked cells. Partially soiled mc-Si cell causes a notable reduction in the string's generated electrical energy as a burnt cell, however a burnt cell poses a high risk of fire and electrical shock. The non-existence of bypass diodes in CIGS modules can result in shunt paths, severe string power loss and permanent degradation of PV action in the shaded solar cells. Simulation of the soiling scenario on mc-Si module strings show I-V characteristics similar to those the affected strings. EL and UV fluorescence can be of help in identifying non-visual causes of certain thermal signatures, although such anomalies showed no signs of affecting the string power, in this study. The anomalies discussed in this chapter show similar effects of thermal abnormality on a module as those highlighted in Table 2.3 and agrees to the outcome discussed in the International Energy Agency Report on Review of Failures in PV modules [17].

Chapter 5

Conclusions

The study investigated the correlation of Thermal Infrared (TIR) Imaging and Current-Voltage (I-V) measurements of PV module strings on PV plants to understand the impact of thermal signatures on the performance of the strings. An Unmanned Aerial Vehicle (UAV) with a mounted TIR camera was flown and rapidly captured thermal images on operating PV modules at a PV plant without affecting the normal operation of the plant. Anomalies in PV modules may cause current mismatch in solar cells leading to hot areas (thermal signatures) in mc-Si and CIGS modules. Visual inspection was carried out on modules with anomalies and it was observed that the two main reasons for current mismatch to occur are; a) uneven illumination on series connected cells and b) cracks causing isolation of current in parts of cells. Uneven illumination was caused by shattered module glass, bird droppings and general soiling. Cell cracks may have been caused by mechanical or thermal stress on the PV module. I-V measurements of the modules and strings were taken, corrected to STC, and analysed. TIR images and I-V measurements were not taken simultaneously, which may have led to imperfect correlation between observations from I-V parameters and TIR images in some cases. The conditions that may cause measurements to change, such as cloud cover, irradiance and wind were avoided or kept constant as best as possible.

Substantial power loss was realised on module strings containing modules with cracked cells, e.g. mc-Si string A500-Inv13-ST04. The power loss in the string A500-Inv13-ST04 was minimised by activation of bypass diodes in the defective module, M02. The bumps in the I-V curve of the defective module were reflected in the string's I-V curve and the output power was 7.6% lower than the reference string.

CIGS module strings A200-Inv11-ST08 and A700-Inv17-ST09 each contained a cracked module. The detrimental effect of cracks on the thin film monolithic integrated cells was shown by the change in shunt and series slopes as seen in the I-V curves of the strings containing cracked thin-film modules and caused the strings to underperform by 3.5% and 8.4% respectively. No bump was seen in the I-V curves of the strings since no bypass diode is incorporated in the CIGS modules. The absence of bypass diodes may have resulted in irreversible damage of module M01 in string A200-Inv11-ST07. The current mismatch was

caused by uneven shading due to dirt on the module and the I-V curve of the string shows a bump close to I_{sc} which was as a result of severe reverse voltage breakdown of the shaded cells.

Multi-crystalline strings A600-Inv16-ST04 and A300-Inv20-ST04 each contained a module under uneven shading due to bird dropping and soiling respectively. Notable power loss of less than 1.0% was realised on these strings since the shading covered a small area and bypass diodes in the modules minimised the impact of shading on the string's generated power. This shows the importance of bypass diodes in series connected PV modules.

Partial shading on solar cells or any anomaly on module operation which causes current mismatch creates a thermal signature and forces the operating point, P_{max}, on the I-V curve of the module string to change. The P_{max} point shifts towards V_{oc} (higher voltage, lower current) in small current mismatch scenarios while when current mismatch is high, the P_{max} point moves towards I_{sc} (lower voltage, high current) thus affecting the normal operation of the module or string and subsequently reducing the generated power. The shape of the mc-Si module or string I-V curve can be deduced when the soiling pattern on the module is known since there are two variables and four possibilities which affect the I-V curve. Light shading causes small change in current and result in shallow bumps whereas heavy soiling result in large change in current and cause deep bumps. If more cells are shaded a big drop in voltage will be noticed in the I-V curve while if few cells are under shade the bump will appear closer to V_{oc}.

A weak electrical connection resulting in a burnt cell on module M01 in string A100-Inv06-ST01 caused an observable drop in the generated power of the whole string (2.1%) and increased the series resistance of the string. The module may continue to deteriorate over time and further reduce the string power. Therefore, regular maintenance of the PV system is necessary which involves cleaning of soiled modules and checking for anomalies such as cracked or burnt solar cells in modules as they pose high safety and fire risks.

There were anomalies causing temperature irregularities in a module that could not be visually observed and TIR could only identify the anomalies as hot areas. Such cell defects call for further investigation using other testing techniques that can identify cracks in cells, such as EL and UV fluorescence. Additional inspection techniques will help to support the observed correlation of aerial thermal imaging with I-V parameters of PV modules. The study highlighted the fast and efficient use of TIR imaging in modules to locate portions of cells or complete cells that do not contribute power or may even consume power in operating PV module strings. Such understanding is important as it can contribute towards fast and effective

PV maintenance systems where the UAV thermography inspection technique can be applied for the in-situ evaluation of PV modules performance, thus quantifying power loss instead of just locating defects. It can also be of interest for PV plant operators, maintenance engineers, the research and development sector and future investors in the PV industry.

References

[1] K. Mertens, *Photovoltaics: Fundamentals, Technology and Practice*, 1st ed. Chichester, West Sussex, UK: John Wiley & Sons Ltd, 2014.

[2] REN21 Secretariat, "Renewables 2017 Global Status Report," 2017. [Online]. Available: http://www.ren21.net/wp_content/uploads/2017/06/178399_GSR_2017_Full_Report_0621_Opt.pdf. [Accessed: 18-May-2018].

[3] C. Breyer *et al.*, "On the role of solar photovoltaics in global energy transition scenarios," *Prog. Photovoltaics Res. Appl. John Wiley Sons, Ltd*, 2017.

[4] M. Wara, D. Cullenward, and R. Teitelbaum, "Peak Electricity and the Clean Power Plan," *Electr. J.*, vol. 28, no. 4, pp. 18–27, 2015.

[5] IEA PVPS, "5th edition report of the Snapshot of global photovoltaic markets," 2017.

[6] IEA PVPS, "22nd edition of the international survey report on Trends in Photovoltaic Applications," 2017.

[7] S. Bawakyillenuo, "Deconstructing the dichotomies of solar photovoltaic (PV) dissemination trajectories in Ghana, Kenya and Zimbabwe from the 1960s to 2007," *Energy Policy*, vol. 49, pp. 410–421, 2012.

[8] A. Eberhard and R. Naude, "The South African Renewable Energy Independent Power Producer Procurement Programme: A Review and Lessons Learned," *J. Energy South. Africa*, vol. 27, no. 4, p. 1, 2016.

[9] IEA, "Photovoltaic Power System Program (PVPS) Annual Report 2017," 2018.

[10] Sustainable Energy Africa, "Sustainable energy solutions for South African local government: a practical guide," *Cape Town: Sustainable Energy Africa*, 2017. [Online]. Available: https://www.sustainable.org.za/userfiles/process(2).pdf. [Accessed: 06-May-2018].

[11] "Solargis.com." [Online]. Available: http://solargis.com/assets/graphic/free-map/DNI/Solargis-World-DNI-solar-resource-map-en.png. (2016). [Accessed: 15-Jun-2018].

[12] R. Gumbo, L. T. Katsvairo, and K. Asai, "State of Photovoltaic home systems in Zimbabwe," *3rd Word Conf. Photovolt. Energy Convers. Proc.*, pp. 2640–2643, 2003.

[13] "ESI AFRICA." [Online]. Available: https://www.esi-africa.com/zimbabwes-solar-energy-projects/. [Accessed: 18-Jul-2018].

[14] C. T. Mzezewa and C. S. Murove, “Renewable Energy Market Study Report - Zimbabwe,”2017.[Online].Available:https://www.rvo.nl/sites/default/files/2017/11/renewable-energy-market-study-zimbabwe-2017.pdf. [Accessed: 20-Jul-2018].

[15] E. L. Meyer and E. E. van Dyk, “Assessing the Reliability and Degradation of Photovoltaic Module Performance Parameters,” *IEEE*, vol. 53, no. 1, pp. 83–92, 2004.

[16] C. Ferrara and D. Philipp, “Why do PV modules fail?,” *Elsevier - Energy Procedia*, vol. 15, pp. 379–387, 2012.

[17] M. Köntges *et al.*, “Review of Failures of Photovoltaic Modules,” IEA-PVPS, 2014.

[18] N. L. Purohit and Anshika, “Data Acquisition of Solar Power Plant Using Scada System,” *Int. J. Eng. Trends Technol.*, pp. 189–194, 2015.

[19] C. Buerhop, R. Weißmann, H. Scheuerpflug, R. Auer, and C. J. Brabec, “Quality Control of PV-Modules in the Field Using a Remote -Controlled Drone with an Infrared Camera,” *27th Eur. Photovolt. Sol. Energy Conf. Exhib. Proc.*, pp. 3370–3373, 2012.

[20] M. Aghaei, P. B. Quater, F. Grimaccia, S. L. Leva, and M. Mussetta, “Unmanned Aerial Vehicles in Photovoltaic Systems Monitoring Applications,” *29th Eur. Photovolt. Sol. Energy Conf. Exhib. Proc.*, pp. 2734–2739, 2014.

[21] G. Boyle, *Renewable Energy: Power for a Sustainable Future*, 3rd ed. Oxford: Oxford University Press, 2012.

[22] S. L. Sheng, *Semiconductor Physical Electronics*, 2nd ed. New York: Springer, 2006.

[23] R. A. Messenger and J. Ventre, *Photovoltaic Systems Engineering*, 2nd ed. Boca Raton London New York Washington, D.C: CRC Press LCC, 2005.

[24] A. J. Sangster, “Renewable Energy Technologies: Cost analysis series,” *Int. Renew. Energy Agency*, vol. 194, no. 4, pp. 145–172, 2014.

[25] C. Tzikas, G. Gomez, M. van den Donker, K. Bakker, A. H. M. Smets, and W. Folkerts, “DO THIN FILM PV MODULES OFFER AN ADVANTAGE UNDER PARTIAL SHADING CONDITIONS?,” *33rd Eur. Photovolt. Sol. Energy Conf. Exhib. Proc.*, pp. 1593–1596, 2017.

[26] S. Bowden and C. Honsberg, “PVCDROM | PVEducation.” http://pveducation.org/pvcdrom, (Accessed 15 July 2018).

[27] U. Jahn *et al.*, “Review on Infrared and Electroluminescence Imaging for PV Field Applications,” IEA-PVPS, 2018.

[28] T. J. Silverman, L. Mansfield, I. Repins, and S. Kurtz, “Damage in monolithic thin-film photovoltaic modules due to partial shade,” *44th IEEE Photovolt. Spec. Conf. Proc.*, pp. 1333–1338, 2018.

[29] S. Silvestre, A. Boronat, and A. Chouder, “Study of bypass diodes configuration on PV modules,” *Appl. Energy*, vol. 86, no. 9, pp. 1632–1640, 2009.

[30] D. L. King, J. K. Dudley, and W. E. Boyson, “PVSIM©: A Simulation Program for Photovoltaic Cells, Modules, and Arrays,” *25th IEEE Photovolt. Spec. Conf. Proc.*, pp. 1295–1297, 1996.

[31] A. Smets, K. Jäger, O. Isabella, R. Swaaij van, and M. Zeman, *Solar Energy - The Physics and Engineering of Photovoltaic Conversion Technologies and Systems*, 1st ed. CAMBRIDGE: UIT, 2016.

[32] E. Lorenzo and P. Davies, *Solar Electricity: Engineering of Photovoltaic Systems*, 1st ed. Sevilla, Spain: PROGENSA, 1994.

[33] Solmetric Corporation, “Guide To Interpreting I-V Curve Measurements of PV Arrays,” 2011. [Online]. Available: http://resources.solmetric.com/get/Guide to Interpreting I-V Curves.pdf. [Accessed: 06-Jul-2018].

[34] M.S. Tyagi, *Introduction to Semiconductor Material and Devices*, 1st ed. New York: John Wiley & Sons, 1991.

[35] J. L. Crozier, “Characterization of cell mismatch in photovoltaic modules using electroluminescence and associated electro-optic techniques,” MSc thesis, Nelson Mandela Metropolitan University, 2012.

[36] E. E. van Dyk, B. J. Scott, E. L. Meyer, and A. W. R. Leitch, “Temperature dependance of performance of crystalline silicon photovoltaic moduless,” *S. Afr. J. Sci.*, pp. 198–200, 2000.

[37] Joint Committee For Guides In Metrology (JCGM), “Evaluation of measurement data — Guide to the expression of uncertainty in measurement,” *Int. Organ. Stand. Geneva ISBN*, 2008.

[38] A. Luque and S. Hegedus, *Handbook of Photovoltaic Science and Engineering*. John Wiley & Sons Ltd, Chichester, West Sussex, England, 2003.

[39] E. E. van Dyk and E. L. Meyer, “Analysis of the effect of parasitic resistances on the performance of photovoltaic modules,” *Renew. Energy*, vol. 29, no. 3, pp. 333–344, 2004.

[40] J. L. Crozier, E. E. van Dyk, and F. J. Vorster, “Evaluating the Relationship Between Electroluminescence (EL) Imaging and the Power Output of Photovoltaic Modules,” *South. African Sol. Energy Conf. Proc.*, pp. 24–28, 2015.

[41] F. Mani, S. Pulipaka, and R. Kumar, “Characterization of power losses of a soiled PV panel in Shekhawati region of India,” *Sol. Energy*, vol. 131, pp. 96–106, 2016.

[42] J. L. Crozier, E. E. Van Dyk, and F. J. Vorster, “Identification and characterisation of performance limiting defects and cell mismatch in photovoltaic modules,” *Energy South. Africa*, vol. 26, no. 3, pp. 19–26, 2015.

[43] N. H. Zaini *et al.*, “Lightning surge analysis on a large scale grid-connected solar photovoltaic system,” *Energies*, vol. 10, no. 12, 2017.

[44] F. J. Vorster and E. E. Van Dyk, “Current-voltage characteristics of high-concentration, photovoltaic arrays,” *Prog. Photovoltaics Res. Appl.*, vol. 13, no. 1, pp. 55–66, 2005.

[45] M. C. Alonso-García and J. M. Rui, “Analysing and modelling the reverse characteristic of photovoltaic cells,” *Sol. Energy Mater. Sol. Cells*, pp. 1105–1120, 2006.

[46] X. P. V. Maldague, *Theory and practice of infrared technology for nondestructive testing*, 1st ed. New York: Wiley-Interscience, 2001.

[47] C. Buerhop, T. Pickel, M. Dalsass, H. Scheuerpflug, C. Camus, and C. J. Brabec, “AIR-PV-check: A quality inspection of PV-power plants without operation interruption,” *44th IEEE Photovolt. Spec. Conf. Proc.*, pp. 1–5, 2016.

[48] F. A. Hunter, M. W. Davis, B. P. Dougherty, D. L. King, W. E. Boyson, and J. A. Kratochvil, “Comparison of Photovoltaic Module Performance Measurements,” *J. Sol. Energy Eng.*, vol. 128, no. 2, pp. 152–159, 2006.

[49] U. Hoyer, A. Burkert, R. Auer, and C. Buerhop-Lutz, “Analysis of PV Modules by Electroluminescence and IR Thermography,” *24th Eur. Photovolt. Sol. Energy Conf. Proc.*, 2009.

[50] C. Buerhop-Lutz and H. Scheuerpflug, “Inspecting PV plants using aereal, drone-mounted infrared thermography system,” *South. African Sol. Energy Conf. Proc.*, pp. 422–429, 2015.

[51] “Eskom company information.” [Online]. Available: http://www.eskom.co.za/OurCompany/CompanyInformation/Pages/Company_Information.aspx. [Accessed: 11-Aug-2018].

[52] T. J. Serameng, K. T. Roro, E. E. van Dyk, J. L. Crozier, and F. J. Vorster, “Comparison of performance and degradation of different PV plant configurations in Johannesburg, South Africa,” *33rd Eur. Photovolt. Sol. Energy Conf. Exhib. Proc.*, pp. 2229–2234, 2015.

[53] “FLIR Infrared camera datasheet.” [Online]. Available: https://www.flir.com/globalassets/imported-assets/document/16-0423-oem-datasheet-update-tau-2.pdf. [Accessed: 17-Aug-2018].

[54] C. Buerhop, H. Scheuerpflug, and R. Weißmann, “The Role of Infrared Emissivity of Glass on IR-imaging of PV-Plants,” *26th Eur. Photovolt. Sol. Energy Conf. Exhib. Proc.*, pp. 3413–3416, 2011.

[55] FLIR Systems, “Thermal Imaging Guidebook for building and renewable energy applications,” 2011. [Online]. Available: http://www.flirmedia.com/MMC/THG/Brochures/T820325/T820325_EN.pdf. [Accessed: 07-Sep-2018].

[56] Solmetric Corporation, “Solmetric PV Analyzer I-V Curve Tracer with SolSensor ™ User ’ s Guide,” 2014. [Online]. Available: http://www.solmetric.net/get/PVA-SolSensor-Users-Guide-Feb19-2014.pdf. [Accessed: 02-Sep-2018].

[57] Solmetric Corporation, “Solmetric PV Analyzer I-V Curve Tracer with SolSensor ™ User ’ s Guide,” 2018. [Online]. Available: http://www.solmetric.net/get/Solmetric PV Analyzer Users Guide_1500_en.pdf. [Accessed: 02-Sep-2019].

[58] M. R. Maghami, H. Hizam, C. Gomes, M. A. Radzi, M. I. Rezadad, and S. Hajighorbani, “Power loss due to soiling on solar panel: A review,” *Renew. Sustain. Energy Rev.*, vol. 59, pp. 1307–1316, 2016.

[59] T. J. Silverman and I. Respins, “Shadows from people and tools can cause permanent damage in monolithic thin-film Photovoltaics modules,” *33rd Eur. Photovolt. Sol. Energy Conf. Exhib. Proc.*, pp. 1422–1426, 2017.

[60] J. H. Wohlgemuth and S. R. Kurtz, “How can we make PV modules safer?,” *Conf. Rec. IEEE Photovolt. Spec. Conf. Proc.*, pp. 3162–3165, 2012.

Appendix A

Research outputs associated with this work

A.1 National Conference Attended

- 5th Southern African Solar Energy Conference, 25-27 June 2018, Durban.